4-2016

Transfers to a gravitational saddle point: An extended mission design option for LISA Pathfinder

Andrew D. Cox
Purdue University

Graduate School Form
30 Updated 12/26/2015

PURDUE UNIVERSITY
GRADUATE SCHOOL
Thesis/Dissertation Acceptance

This is to certify that the thesis/dissertation prepared

By Andrew D Cox

Entitled
Transfers to a Gravitational Saddle Point: An Extended Mission Design Option for LISA Pathfinder

For the degree of Master of Science in Aeronautics and Astronautics

Is approved by the final examining committee:

Kathleen C. Howell
Chair

Carolin E. Frueh

William A. Crossley

To the best of my knowledge and as understood by the student in the Thesis/Dissertation Agreement, Publication Delay, and Certification Disclaimer (Graduate School Form 32), this thesis/dissertation adheres to the provisions of Purdue University's "Policy of Integrity in Research" and the use of copyright material.

Approved by Major Professor(s): Kathleen C. Howell

Approved by: Weinong Wayne Chen 04/17/2016
Head of the Departmental Graduate Program Date

TRANSFERS TO A GRAVITATIONAL SADDLE POINT: AN EXTENDED MISSION DESIGN OPTION FOR LISA PATHFINDER

A Thesis

Submitted to the Faculty

of

Purdue University

by

Andrew D. Cox

In Partial Fulfillment of the

Requirements for the Degree

of

Master of Science in Aeronautics and Astronautics

May 2016

Purdue University

West Lafayette, Indiana

"We have lingered long enough on the shores of the cosmic ocean. We are ready at last to set sail for the stars"

- Carl Sagan, *Cosmos*

ACKNOWLEDGMENTS

First and foremost, I must thank my family: Mom, Dad, Brian, Jason, and Tim. Your unceasing love and support mean the world to me. Mom and Dad, thank you for encouraging me to work hard and for supporting me throughout college and graduate school. I could not have made it this far without you.

I am extraordinarily grateful to my advisor, Professor Kathleen C. Howell. Your enthusiasm for your work and teaching inspired me to pursue post-graduate education and continues to inspire me. Thank you for giving me the opportunity to join your research group. It goes without saying that this research would not have been possible without your insights, guidance, and support. I am excited to continue learning from you.

I am also incredibly thankful for teachers and advisors that have passed on their contagious excitement for learning and taught me valuable lessons. Delcie Pace, Bajorn Gaylord, Kim Stover, and Rick Weinheimer, I cannot begin to express how grateful I am for the education you provided me. If I have any writing skills at all, it is due to your teaching. Jamie Champlin, Mike Spock, Nathan Schieffer, Professor Akil Narayan, and Professor Sameer Naik, thank you for showing me that math and science can be beautiful, creative, and exciting. Additionally, I would not be where I am today without the influence of my friends and classmates. Katie, Parth, Krista, Tom, Ronak, and Sean, thank you for your encouragement and support, especially on those days when all I wanted to do was quit. You have truly pushed me to be the best I can be.

I would also like to thank my committee members, Professors William A. Crossley and Carolin Frueh. Thank you for taking the time to review my thesis and provide feedback. For providing funding for my studies, I would like to thank the School of Aeronautics and Astronautics, as well as the College of Engineering. Finally, thank

you to my coworkers, collaborators, and colleagues for their invaluable advice and inspiration: Amanda, Masaki, Loic, Natasha, Ash, Davide, Lucia, Bonnie, Robert, Wayne, Cody, Rohan, Chris, Alex, Ted, Emily, Joseph, and Dave. I look forward to continuing to work with all of you.

TABLE OF CONTENTS

Page

LIST OF TABLES

LIST OF FIGURES

ABSTRACT

Cox, Andrew D. MSAA, Purdue University, May 2016. Transfers to a Gravitational Saddle Point: An Extended Mission Design Option for LISA Pathfinder. Major Professor: Kathleen C. Howell.

Any possible LISA Pathfinder extended mission will immediately follow the primary mission after completion of scientific observations and technical demonstrations in a Sun-Earth L_1 libration point orbit. One extended mission concept with scientific appeal is a spacecraft path that includes multiple encounters with a gravitational equilibrium point. This point, also termed a *saddle point*, exists where the total gravitational acceleration sums to zero and is distinct from the five Lagrange points in the three-body problem. This investigation seeks a strategy to design such a path subject to a variety of constraints. Periodic, quasi-periodic, and manifold structures are explored to supply useful transit behavior as well as arcs that repeatedly encounter the saddle point. A selection of these structures from the Earth-Moon and Sun-Earth circular restricted three-body problems are linked together via Poincaré mapping techniques and corrected in a higher-fidelity Sun-Earth-Moon bicircular restricted four-body problem (BC4BP) and in an ephemeris environment. Additionally, natural motion in the BC4BP is leveraged to achieve the required encounters, and is similarly corrected to meet mission constraints. Results from both methods are detailed and compared to the mission requirements.

1. INTRODUCTION

Repeated encounters of specific locations in space drive several types of applications. In one such scenario, repeated passage of a dynamically defined relative position offers the opportunity to corroborate science data gathered during preliminary flybys. This investigation seeks a strategy to design such a path subject to a variety of constraints by exploring an extended mission concept for the Laser Interferometer Space Antenna (LISA) Pathfinder spacecraft.

The primary mission for the LISA Pathfinder spacecraft occurs in the vicinity of the Sun-Earth L_1 libration point. Following the primary mission, the spacecraft can depart this region for an extended mission by leveraging its remaining propellant resources. One extended mission concept with particular scientific appeal is a spacecraft path that includes multiple passes near a specific gravitational equilibrium point. The focus of this effort is a strategy to design such an end-to-end transfer. Dynamical structures that emerge in the Circular Restricted 3-Body Problem (CR3BP), including quasi-periodic tori and invariant manifolds, are leveraged as part of the trajectory design scheme.

1.1 Problem Definition

The LISA Pathfinder (LPF) mission aims to demonstrate technologies required for space-based gravitational wave detection and will pave the way for the joint ESA/NASA LISA mission [1, 2]. The science experiments aboard the LPF spacecraft require stringent constraints on thermal and gravitational stability, thus, a "quiet" location in space is identified for the mission. A Sun-Earth L_1 Lissajous orbit with in-ecliptic amplitude of 800,000 km and out-of-ecliptic amplitude of 500,000 km is selected for the six month science phase; the spacecraft remains far from any mas-

sive bodies, maintains constant solar illumination as well as a quasi-constant distance from the Earth for communications purposes [1, 2, 3].

Following the 180-day primary mission, LPF may depart the Sun-Earth libration point region to enable an extended mission phase. The extended mission concept of interest is a spacecraft path that includes multiple passes near a gravitational equilibrium point, termed a *saddle point*. At such a point, gravitational accelerations from nearby massive bodies sum to a net-zero acceleration and, with repeated passes by the saddle point, it may be possible to measure the effects of MOdified Newtonian Dynamics (MOND) [4]. MOND was originally proposed by Milgrom as a solution to the "missing mass problem" in the universe, that is, the discrepancy between the observed motion of galaxies and the predictions of their motion computed via classical Newtonian dynamics based on the observed mass of the galaxies[5]. This "missing mass," is commonly attributed to the existence of *dark matter*, though attempts to observe dark matter particles have not yet proven successful [6]. MOND proposes an adjustment to classical Newton dynamics in systems such as galaxies where acceleration levels are very small, i.e., on the order of 10^{-10} m/s^2. Under such modified dynamics, dark matter need not exist to ensure coherence between observed motion and mass. Due to the high sensitivity of its graviational instruments, LPF is well-suited to seek evidence of MOND at a local gravitational equilibrium point.

Any extended mission concept for LPF cannot interfere with the primary mission and, thus, is subject to a variety of constraints. First, the cold gas micropropulsion system available on-board LPF produces thrust levels that are low and, consequently, will require time to perform maneuvers. Fabacher et al. estimate that a 1 m/s maneuver will require approximately 10 days to complete [3]. To reduce complexity in this investigation, this constraint is ignored and all maneuvers are assumed to be impulsive and instantaneous. Second, the amount of propellant remaining after the completion of the primary mission is capable of imparting a ΔV between 4 and 5 m/s to the spacecraft. Another challenge is the necessity to minimize operational costs associated with flying the extended mission, thus, the total post-mission time-of-flight

should not exceed two years. Additionally, the spacecraft must encounter the saddle point at least twice to obtain and verify the desired MOND measurements. Each pass should occur within 100 km of the exact saddle point location and at Earth-centered inertial velocities between 1 - 2 km/s to ensure the desired signal remains within the frequency bands available to the scientific instruments [7].

This analysis into a potential approach to deliver a transfer path for the LPF extended mission phase explores several design architectures that leverage natural motion in the CR3BP as well as the bi-circular restricted four-body problem (BC4BP). This natural flow enables construction of a low-cost trajectory that meets all constraints on the LPF extended mission concept. More generally, an architecture for the design of low-cost transfers is sought. In particular, paths that include multiple passes near a desired dynamical target, such as the saddle point, libration points, or other similar locations.

1.2 Previous Contributions

A few previous studies have been completed to investigate the possibility of the proposed extended mission concept. In 2009, Trenkel and Kemble examined the feasibility of direct and indirect paths from the LPF primary mission orbit to the saddle point [8]. The results verify that, in theory, the cold gas thrusters aboard LPF are capable of redirecting the spacecraft to achieve a saddle point encounter and that the conditions at the encounter facilitate MOND measurements by the on-board science instruments. In a subsequent development, a numerical method is offered to estimate the anomalous gradients that LPF encounters near the saddle point and demonstrates that the LPF instrumentation is capable of not only detecting, but also capturing, the detailed measurements of the predicted MOND gradients [9]. A more recent analysis by Fabacher et al. employs numerical techniques such as grid searches and optimization algorithms to identify feasible solutions that possess two saddle point encounters and, when propagated in reverse time, reach a loosely-bounded orbit near

the Sun-Earth L_1 point [3]. Fabacher et al. demonstrate a transfer from the L_1 vicinity that achieves two saddle point encounters within several hundred kilometers without exceeding the allotted 4-5 m/s maneuvering capability. In the sample path, the originating orbit possesses approximate dimensions of 800,000 km in-ecliptic amplitude and 150,000 km out-of-ecliptic amplitude. The current investigation aims to recreate the transfer demonstrated by Fabacher et al via natural structures in the CR3BP.

1.3 Document Overview

Multiple strategies to construct end-to-end trajectories that originate from the LPF primary mission orbit are developed. The unstable invariant manifolds associated with periodic and quasi-periodic motion in the vicinity of the Sun-Earth L_1 libration point are exploited to supply low-cost departures from the LPF primary mission orbit toward the saddle point. Natural motion in the CR3BP and BC4BP are employed as mechanisms to achieve multiple saddle point encounters and a multiple shooting corrections process is applied to enforce all relevant constraints. Sample transfer options are transitioned to higher-fidelity ephemeris models to demonstrate their persistence and validity.

The organization of this investigation proceeds as follows:

- Chapter 2: The equations of motion are derived for the CR3BP. A single integral of the motion, as well as a set of five equilibrium solutions, is identified and offers insight into the problem. Zero velocity surfaces and symmetry properties are also developed to supply further awareness of the regions governing the dynamical flow. A higher-fidelity BC4BP model is also developed and transformations between the reference frames are derived to facilitate straightforward transitions between models.

- Chapter 3: In this chapter, analytical and numerical techniques are developed to facilitate analysis in the CR3BP and BC4BP. Linearized dynamics relative to the fixed points in the system supply useful predictions of the nonlinear dynam-

ics. The State Transition Matrix (STM) is described and employed to describe the stability of solutions to the EOMs. Additionally, the STM is leveraged to identify stable, unstable, and center manifolds associated with the equilibrium solutions and periodic orbits; these manifolds supply a variety of additional design options. A differential corrections algorithm is derived to facilitate transitions between linear approximations and the full nonlinear dynamics and to adjust trajectories to meet specific constraints. This algorithm is applied to construct resonant orbits as well as other periodic solutions. Two continuation schemes, natural parameter continuation and pseudo-arclength continuation, are developed to expand single solutions into families of similar trajectories. Finally, the stable, unstable, and center manifolds associated with periodic orbits are employed to produce transit manifold arcs as well as quasi-periodic motion.

- Chapter 4: A model of the LPF primary mission orbit is developed and the saddle point behavior is investigated in detail. Low-cost transit arcs originating at the approximate primary mission orbit and flowing toward the saddle point are computed in the Sun-Earth CR3BP. Additionally, natural motion in the Earth-Moon CR3BP and Sun-Earth-Moon BC4BP is surveyed to identify trajectories that achieve multiple saddle point encounters. Higher-dimensional Poincaré mapping techniques are leveraged to select low-cost transitions between Sun-Earth and Earth-Moon motion, and tools are developed to combine the primary mission orbit, transit arcs, and saddle point encounter paths into an end-to-end trajectory in the Sun-Earth-Moon BC4BP.

- Chapter 5: Sample transfer designs that leverage Sun-Earth unstable manifold arcs and Earth-Moon resonant orbits are constructed, corrected, and compared with the mission constraints. Similarly, transfer designs that employ natural motion within the Sun-Earth-Moon BC4BP are computed and corrected to meet mission requirements. These transfers are also transitioned to higher-fidelity ephemeris models to validate the design.

- Chapter 6: A summary of the results is presented and recommendations for future work are suggested.

2. SYSTEM MODELS

Though analytical expressions exist to predict spacecraft motion under the influence of a single massive body, the addition of even one gravitational body renders such two-body approximations inaccurate. However, the more complex multi-body dynamics do not possess analytical solutions and are, therefore, investigated via numerical integration of the governing differential equations of motion. As a first step, the circular restricted three-body problem is formulated to describe the motion of a spacecraft under the influence of two point mass gravitational forces. A higher fidelity, bicircular, restricted four-body model is also developed and employed in this investigation to predict spacecraft motion with an additional perturbing mass.

2.1 Circular Restricted Three-Body Problem

Although the three-body problem possesses no analytical solution, many insights are available from the simplified circular restricted three-body problem (CR3BP). To enable numerical integration, the equations governing motion in the CR3BP are derived. These differential equations possess one energy-like integral of motion, termed the *Jacobi constant*, which can be leveraged as a comparator between solutions. The governing equations also admit five equilibrium solutions, which provide a basic understanding of motion in the system. Zero velocity surfaces and problem symmetry supply further information about solutions in the CR3BP.

2.1.1 Equations of Motion

The circular restricted three-body problem (CR3BP) describes the motion of three barycentric bodies P_1, P_2, and P_3 with masses m_1, m_2 and m_3, respectively. It is

assumed that P_3 possesses negligible mass compared to the other two bodies (i.e., $m_3 << m_1, m_2$) and, thus, does not affect their motion. The paths of the two larger bodies, termed *primaries*, are therefore governed by two-body dynamics and are represented by conic sections. For simplicity, it is assumed that the two primaries move in circular orbits (rather than more general elliptical orbits) about their mutual barycenter, B, as depicted in Figure 2.1. An inertial frame is defined such that the unit vectors $\hat{\mathbb{X}}$ and $\hat{\mathbb{Y}}$ span the primaries' orbital plane and $\hat{\mathbb{Z}}$ coincides with their angular momentum vector. The circular motion of the primaries is described by simple trigonometric relationships as viewed in this frame:

$$\vec{R}_1 = R_1 \left[-\cos(Nt)\hat{\mathbb{X}} - \sin(Nt)\hat{\mathbb{Y}}, \right] \tag{2.1}$$

$$\vec{R}_2 = R_2 \left[\cos(Nt)\hat{\mathbb{X}} + \sin(Nt)\hat{\mathbb{Y}}, \right] \tag{2.2}$$

where $N = \dot{\theta}$ is the mean motion along the primaries' orbit. The position of P_3, which is free to move in all three spatial dimensions, is denoted $\vec{R}_3$ and is relative to the inertially-fixed base point B. Newton's second law describes the motion of P_3 as viewed by an inertial observer due to the forces exerted on P_3 by P_1 and P_2. The equations that govern this motion are derived from the gradient of the gravitational potential function $U = -G\left(\frac{m_1}{R_{1,3}} + \frac{m_2}{R_{2,3}}\right)$. Accordingly, the acceleration of P_3 is evaluated as

$$\frac{\mathrm{d}^2\vec{R}_3}{\mathrm{d}t^2} = \vec{\nabla}U = -G\frac{m_1}{R_{1,3}^3}\vec{R}_{1,3} - G\frac{m_2}{R_{2,3}^3}\vec{R}_{2,3}. \tag{2.3}$$

This vector equation is nonautonomous as both $\vec{R}_{1,3}$ and $\vec{R}_{2,3}$ explicitly depend on the time-varying positions of P_1 and P_2 as represented in equations (2.1) and (2.2). Formulating the equations of motion in a frame that fixes the primaries' positions offers the advantage of an autonomous system in which energy is conserved. To this end, consider a rotating frame $(\hat{x}, \hat{y}, \hat{z})$ defined with $\hat{x}$ directed from P_1 to P_2 and $\hat{z}$ along the angular velocity of the primary orbit; $\hat{y}$ completes the orthonormal set. In this rotating frame, both primaries are stationary, removing any requirement for explicit functions of time in the equations of motion.

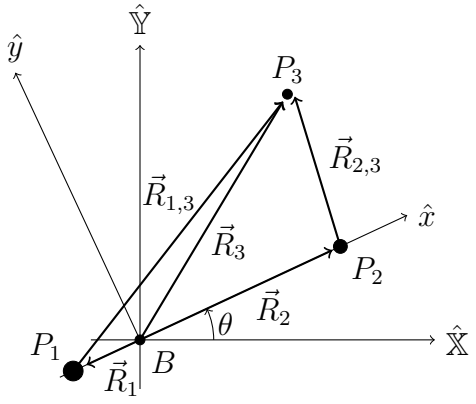

Figure 2.1.: Reference Frame Definition in the CR3BP

To further simplify notation and reduce round-off error during numerical integration, all variables are nondimensionalized by characteristic quantities. The characteristic length is the constant distance between the two primaries $l_* = R_1 + R_2$, the characteristic mass defines the total system mass $m_* = m_1 + m_2$, and a characteristic time is deduced by the reciprocal of the mean motion of the primaries $t_* = 1/N = \sqrt{l_*^3/(Gm_*)}$. Let lowercase letters represent nondimensional quantities as follows:

$$\vec{R}_i = l_*\vec{r}_i, \qquad m_2 = m_*\mu, \qquad t = t_*\tau.$$

An expression for m_1 is obtained in terms of the system mass ratio μ:

$$m_1 = (1-\mu)m_*. \tag{2.4}$$

As a result of applying these characteristic quantities, the nondimensional mean motion of the primaries n and the semi-major axis a are equal to unity, therefore, the

period of primary motion is $\tilde{T} = 2\pi/n = 2\pi$. Substituting nondimensional quantities into equation (2.3) results in the following relationship:

$$\begin{aligned}
\frac{\mathrm{d}^2\vec{r}_3}{\mathrm{d}\tau^2}\left(\frac{l_*}{t_*^2}\right) &= -G\left[\frac{m_*(1-\mu)l_*\vec{r}_{1,3}}{r_{1,3}^3 l_*^3} + \frac{m_*\mu l_*\vec{r}_{2,3}}{r_{2,3}^3 l_*^3}\right] \\
\ddot{\vec{r}}_3 &= -G\frac{m_*}{l_*^3}\left(\sqrt{\frac{l_*^3}{Gm_*}}\right)^2\left[\frac{(1-\mu)}{r_{1,3}^3}\vec{r}_{1,3} + \frac{\mu}{r_{2,3}^3}\vec{r}_{2,3}\right] \\
\ddot{\vec{r}}_3 &= \frac{(1-\mu)}{r_{1,3}^3}\vec{r}_{1,3} + \frac{\mu}{r_{2,3}^3}\vec{r}_{2,3}, \qquad (2.5)
\end{aligned}$$

where $\vec{r}_3$ is expressed in rotating coordinates as $\vec{r}_3 = x\hat{x} + y\hat{y} + z\hat{z}$ and the dots over a vector represent derivatives with respect to nondimensional time τ. The vectors $\vec{r}_{1,3}$ and $\vec{r}_{2,3}$ locate P_3 relative to P_1 and P_2, respectively, and are evaluated as $\vec{r}_{1,3} = \vec{r}_3 - \vec{r}_1$ and $\vec{r}_{2,3} = \vec{r}_3 - \vec{r}_2$. The distance from P_1 to the center of mass along the $\hat{x}$-axis, r_1, is expressed via the definition of center of mass:

$$R_1 = \frac{0m_1 + l_*m_2}{m_1 + m_2} \quad \rightarrow \quad r_1 l_* = \frac{l_* m_* \mu}{m_*} \quad \therefore \quad r_1 = \mu. \qquad (2.6)$$

As the nondimensional distance between the primaries is unity, the nondimensional distance r_2 is evaluated as $r_2 = 1 - \mu$. Substituting these relationships for r_1 and r_2 into the expressions for $\vec{r}_{1,3}$ and $\vec{r}_{2,3}$ yields

$$\vec{r}_{1,3} = x\hat{x} + y\hat{y} + z\hat{z} - \mu\hat{x} \qquad = (x-\mu)\hat{x} + y\hat{y} + z\hat{z}, \qquad (2.7)$$

$$\vec{r}_{2,3} = x\hat{x} + y\hat{y} + z\hat{z} - (1-\mu)\hat{x} = (x-1+\mu)\hat{x} + y\hat{y} + z\hat{z}. \qquad (2.8)$$

The relationship in equation (2.5) applies only for derivatives of $\vec{r}_3$ relative to an inertial observer and with respect to an inertial base point. In general, as is the case with the CR3BP equations of motion (EOMs), it is not convenient to compute derivatives in an inertial frame and a rotating frame supplies a convenient alternative. The Basic Kinematic Equation (BKE) relates derivatives relative to two different frames, i.e., a rotating frame $\hat{f}$ and an inertial frame $\hat{i}$. If the angular velocity of frame $\hat{f}$ relative to frame $\hat{i}$ is given by ${}^i\vec{\omega}^f$, then

$$\frac{{}^i\mathrm{d}\vec{r}_3}{\mathrm{d}\tau} = \frac{{}^f\mathrm{d}\vec{r}_3}{\mathrm{d}\tau} + {}^i\vec{\omega}^f \times \vec{r}_3. \qquad (2.9)$$

Let the unit vectors $\hat{x}$, $\hat{y}$, and $\hat{z}$ define frame $\hat{f}$. The kinematical inertial derivative of $\vec{r}_3$ is then defined as

$$\dot{\vec{r}}_3 = \dot{x}\hat{x} + \dot{y}\hat{y} + \dot{z}\hat{z} + [n\hat{z}] \times [x\hat{x} + y\hat{y} + z\hat{z}]$$
$$\dot{\vec{r}}_3 = (\dot{x} - ny)\hat{x} + (\dot{y} + nx)\hat{y} + \dot{z}\hat{z}. \tag{2.10}$$

Similarly, the second derivative yields

$$\ddot{\vec{r}}_3 = (\ddot{x} - 2n\dot{y} - n^2x)\hat{x} + (\ddot{y} + 2n\dot{x} - n^2y)\hat{y} + \ddot{z}\hat{z}. \tag{2.11}$$

Substituting this expansion, expressions for r_1 and r_2, and the nondimensional value $n = 1$ into equation (2.5) yields three scalar equations describing the motion of P_3 as expressed in terms of rotating coordinates:

$$\ddot{x} - 2\dot{y} - x = -(1-\mu)\frac{x+\mu}{r_{1,3}^3} - \mu\frac{x-1+\mu}{r_{2,3}^3}, \tag{2.12}$$

$$\ddot{y} + 2\dot{x} - y = -(1-\mu)\frac{y}{r_{1,3}^3} - \mu\frac{y}{r_{2,3}^3}, \tag{2.13}$$

$$\ddot{z} = -(1-\mu)\frac{z}{r_{1,3}^3} - \mu\frac{z}{r_{2,3}^3}. \tag{2.14}$$

where $r_{1,3} = \sqrt{(x-\mu)^2 + y^2 + z^2}$ and $r_{2,3} = \sqrt{(x-1+\mu)^2 + y^2 + z^2}$. Recall the inertial potential function, $U = \frac{1-\mu}{r_{1,3}} + \frac{\mu}{r_{2,3}}$, now expressed in terms of nondimensional quantities. A similar *pseudo-potential* Ω is defined as

$$\Omega = U + \frac{1}{2}(x^2 + y^2) = \frac{1-\mu}{r_{1,3}} + \frac{\mu}{r_{2,3}} + \frac{1}{2}(x^2 + y^2). \tag{2.15}$$

This function is associated with the differential equations in equations (2.12) - (2.14). Note that Ω is autonomous and is a function only of position. The equations of motion are then compactly rewritten in terms of the pseudo-potential:

$$\ddot{x} - 2\dot{y} = \Omega_x, \tag{2.16}$$

$$\ddot{y} + 2\dot{x} = \Omega_y, \tag{2.17}$$

$$\ddot{z} = \Omega_z, \tag{2.18}$$

were $\Omega_p = \dfrac{\partial\Omega}{\partial p}$. Note that the x and y accelerations are decoupled from the z acceleration, indicating that the two may evolve separately. Motion that originates entirely in the xy-plane does not develop any motion in the out-of-plane direction.

2.1.2 Jacobi Constant

An integral of the motion offers useful information about solutions in the CR3BP. Because the equations of motion are derived from an autonomous potential function, the system is conservative. The equations of motion therefore possess an energy-like integral of the motion; this constant is derived consistent with the process by Roy [10]. The dot product between the velocity and acceleration vectors $\dot{\vec{r}}_3$ and $\ddot{\vec{r}}_3$ yields the following scalar value:

$$\dot{\vec{r}}_3 \cdot \ddot{\vec{r}}_3 = \dot{x}\ddot{x} + \dot{y}\ddot{y} + \dot{z}\ddot{z} = \Omega_x\dot{x} + \Omega_y\dot{y} + \Omega_z\dot{z}. \tag{2.19}$$

The right side of equation (2.19) represents the total derivative of the pseudo-potential:

$$\frac{\mathrm{d}\Omega}{\mathrm{d}\tau} = \frac{\partial\Omega}{\partial x}\frac{\mathrm{d}x}{\mathrm{d}\tau} + \frac{\partial\Omega}{\partial y}\frac{\mathrm{d}y}{\mathrm{d}\tau} + \frac{\partial\Omega}{\partial z}\frac{\mathrm{d}z}{\mathrm{d}\tau} + \frac{\partial\Omega}{\partial\tau}, \tag{2.20}$$

where the partial $\frac{\partial\Omega}{\partial\tau}$ evaluates to zero because the pseudo-potential is autonomous. Accordingly, the scalar integration of equation (2.19) yields an expression for an energy-like constant:

$$\int \dot{\vec{r}}_3 \cdot \ddot{\vec{r}}_3 \,\mathrm{d}\tau = \frac{1}{2}(\dot{x}^2 + \dot{y}^2 + \dot{z}^2) = \Omega - C \quad \rightarrow \quad C = 2\Omega - v^2. \tag{2.21}$$

The constant C, also denoted the *Jacobi constant*, represents an energy-like quantity such that an increase in the value of Jacobi constant represents a decrease in energy relative to the rotating frame [11].

Consistent with the energy-like property, the Jacobi constant is a useful indicator of the minimum effort required to shift from one arc to another in the CR3BP. Consider a scenario in which a spacecraft is required to adjust its path from one energy C_1 to a path with energy C_2. At an orbit intersection in position space, there is generally a velocity discontinuity, or $\Delta\vec{v}$, one that is overcome via an instantaneous maneuver. In a typical case where this maneuver is accomplished via propulsive means, it is desirable to minimize the magnitude of this discontinuity to conserve propellant. The minimum possible Δv between arcs is available from the energy difference between the arcs.

Let the originating trajectory have velocity $\vec{v}_1$ and let the destination arc have velocity $\vec{v}_2$. A vector triangle, as in Figure 2.2, illustrates the relationship between the two velocities and the angle θ between them. The dotted semi-circle represents the magnitude of $\vec{v}_2$, thus, the maneuver required to deliver $\vec{v}_2$ extends from the tip of $\vec{v}_1$ to a point on the circle. It follows that the magnitude of $\Delta\vec{v}$ is minimized when $\vec{v}_1$ and $\vec{v}_2$ are parallel and $\theta = 0$.

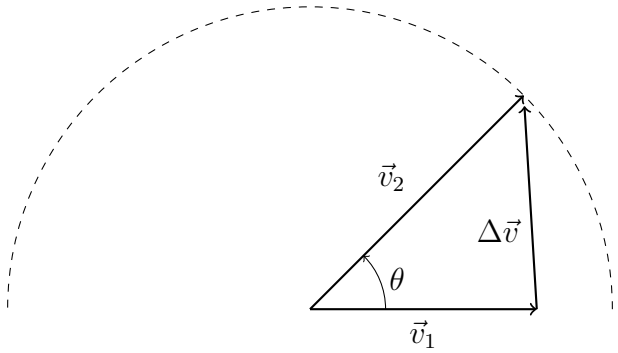

Figure 2.2.: A vector triangle represents the relationships between two velocity vectors and the maneuver vector $\Delta\vec{v}$ required to transition from $\vec{v}_1$ to $\vec{v}_2$. The dotted semicircle represents the magnitude of v_2.

The minimum maneuver magnitude is also obtained mathematically. The magnitude of the maneuver is available from the cosine law:

$$\|\Delta\vec{v}\| = \Delta v = \sqrt{v_1^2 + v_2^2 - 2v_1 v_2 \cos\theta}\,. \tag{2.22}$$

This expression is minimized when $\cos\theta = 1$, i.e., when $\theta = 0$, and the expression for velocity magnitude reduces to

$$\min \Delta v = \sqrt{v_1^2 + v_2^2 - 2v_1 v_2}\,. \tag{2.23}$$

Therefore, the minimum Δv may be computed from the magnitudes of the two velocities. These magnitudes are available from the Jacobi constant difference ΔC. At the intersection of two arcs in position space, the difference in Jacobi is evaluated as

$$\Delta C = C_1 - C_2 = v_2^2 - v_1^2. \tag{2.24}$$

If one of the velocities is known a priori, the other may be expressed as a function of ΔC, e.g.:

$$v_2 = \sqrt{\Delta C + v_1^2}\,. \tag{2.25}$$

Substitution of this quantity into the minimum Δv expression yields

$$\min \Delta v = \sqrt{2v_1^2 + \Delta C - 2v_1\sqrt{\Delta C + v_1^2}}\,. \tag{2.26}$$

Thus, the minimum possible maneuver magnitude between two arcs with different Jacobi constant values are computed given the velocity magnitude on one arc and the difference in the value of Jacobi constant between the two arcs. Though it is not true, in general, that minimizing the energy difference between two arcs minimizes the Δv required to transition from one to the other, the minimum possible Δv to complete the transfer *is* minimized as ΔC approaches zero. Subsequently, transfers between arcs that exist at similar Jacobi constant values potentially require smaller maneuver magnitudes than transfers between arcs with significantly different values of Jacobi constant.

2.1.3 Equilibrium Solutions

Significant insight into the motion in the CR3BP is acquired by analyzing the equilibrium solutions. As equilibrium solutions to the equations of motion, all time derivatives are equal to zero, i.e., $\ddot{z} = \ddot{y} = \ddot{z} = \dot{x} = \dot{y} = \dot{z} = 0$. Substituting these values into the EOMs yields the following factored equations:

$$\Omega_x = -x\left[\frac{(1-\mu)}{r_{1,3}^3} + \frac{\mu}{r_{2,3}^3} - 1\right] + \mu\left[\frac{-(1-\mu)}{r_{1,3}^3} - \frac{\mu}{r_{2,3}^3}\right] + \frac{\mu}{r_{2,3}^3} = 0, \tag{2.27}$$

$$\Omega_y = -y\left[\frac{(1-\mu)}{r_{1,3}^3} + \frac{\mu}{r_{2,3}^3} - 1\right] = 0, \tag{2.28}$$

$$\Omega_z = -z\left[\frac{(1-\mu)}{r_{1,3}^3} + \frac{\mu}{r_{2,3}^3}\right] = 0. \tag{2.29}$$

Equation (2.29) is only satisfied when $z = 0$ as the terms in the square brackets consist only of positive values. Accordingly, all equilibrium solutions exist in the plane of the

primaries' motion. Consider solutions along the line joining the primaries, i.e., $y = 0$. In this case, the equations for an equilibrium solution reduce to

$$x - (1-\mu)\frac{x+\mu}{A(x+\mu)^3} - \mu\frac{x-1+\mu}{B(x-1+\mu)^3} = 0, \tag{2.30}$$

where $A = \text{sgn}(x+\mu)$ and $B = \text{sgn}(x-1+\mu)$. To solve this equation, three separate cases must be examined: (i) both A and B are negative and $-\infty < x \leq -\mu$, (ii) A is positive, B is negative, and $-\mu < x \leq 1-\mu$, and (iii) A and B are both positive and $1-\mu < x < \infty$. Given an initial guess within each range of x, three equilibrium points are computed by numerically solving equation (2.30) for x. Since all three solutions lie on the x-axis, as in Figure 2.3, they are labeled the *collinear* points and are numbered L_1, L_2, and L_3 [12].

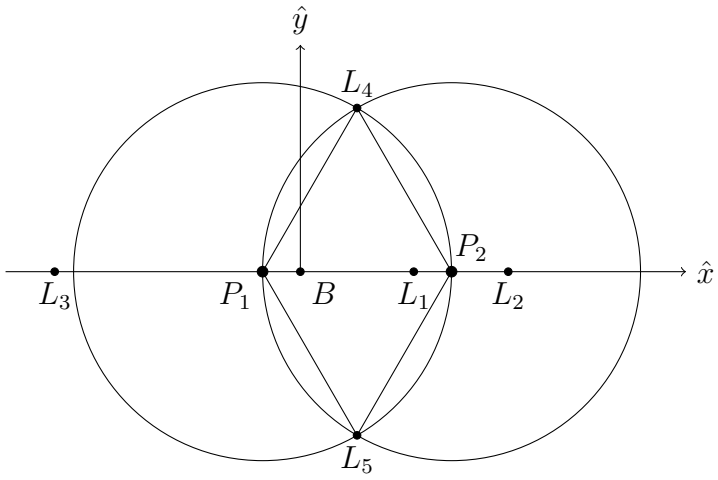

Figure 2.3.: The relative locations of the collinear equilibrium points L_1, L_2, and L_3, as well as the triangular equilibrium points L_3 and L_5.

To locate any remaining equilibrium points, allow $y \neq 0$. In this case, the terms in the square brackets in equation (2.28) must evaluate to zero. This requirement simplifies equation (2.27) and yields the following relationship:

$$x[0] + \mu[-1] + \frac{\mu}{r_{2,3}^3} = 0 \quad \rightarrow \quad r_{2,3}^3 = 1 \quad \therefore \quad r_{2,3} = 1. \tag{2.31}$$

The substitution of $r_{2,3} = 1$ back into equation (2.28) results in $r_{1,3} = 1$. Each expression describes a unit circle centered at P_1 and P_2, respectively. The intersections

of these circles satisfy both equations and locate the remaining equilibrium solutions. Because the nondimensional distance between the primaries is unity, as well as the radii of the circles, the final equilibrium points coincide with the vertices of equilateral triangles and are appropriately termed the *triangular points* and are numbered by convention L_4 and L_5, as depicted in Figure 2.3.

2.1.4 Zero Velocity Surfaces

Although the motion of P_3 cannot be described analytically, bounds on its motion are available from an analysis of its Jacobi constant. The expression for Jacobi constant, i.e., equation (2.21), is rewritten as $v^2 = 2\Omega - C$ to supply information about the magnitude of the velocity of P_3. Clearly, if $C > 2\Omega$, the velocity magnitude is imaginary. As the physical speed v cannot be imaginary, P_3 cannot pass through regions where $C > 2\Omega$. These regions are bounded by surfaces where velocity magnitude is zero, i.e., where $C = 2\Omega$. This three-dimensional (3D) surface is defined by an infinite number of points. For illustrative purposes, consider a cross section of this surface in the xy-plane as depicted in Figure 2.4. The Jacobi constant values associated with the equilibrium points possess corresponding surfaces that serve as boundaries between different surface geometries. These energies are denoted $C_{L_1}, \ldots, C_{L_5}$ and represent the energy at the equilibrium point location and correspond to zero velocity. At low energy levels, i.e., $C > C_{L_1}$, motion near each primary is confined and cannot escape to other regions of space. The planar cross section of the zero velocity surface at such an energy level is depicted in Figure 2.4(a) in the Earth-Moon system. The grey regions represent portions of space where a trajectory with the specified Jacobi value, defined in terms of its 6D position and velocity state, cannot exist; these regions are commonly termed *forbidden regions*. The two primaries are represented by small grey circles and the five equilibrium points are located by black asterisks. As the Jacobi value decreases and energy increases, the forbidden regions in the xy-plane shrink. Once an energy is reached such that $C < C_{L_1}$, a passage, or *gateway*, opens

between the P_1 and P_2 regions and passage between the two primaries is possible (Figure 2.4(b)). Once $C < C_{L_2}$, an additional gateway opens that permits motion to depart the P_1-P_2 system entirely (Figure 2.4(c)). As energy continues to increase, the L_3 gateway opens and the planar forbidden regions recede toward the triangular points (Figure 2.4(d)). At Jacobi constant values less than $C_{L_{4,5}}$, the forbidden regions disappear from the plane, thus planar motion is entirely unbounded. However, out-of-plane zero velocity surfaces persist, though they too recede further from the plane as energy increases.

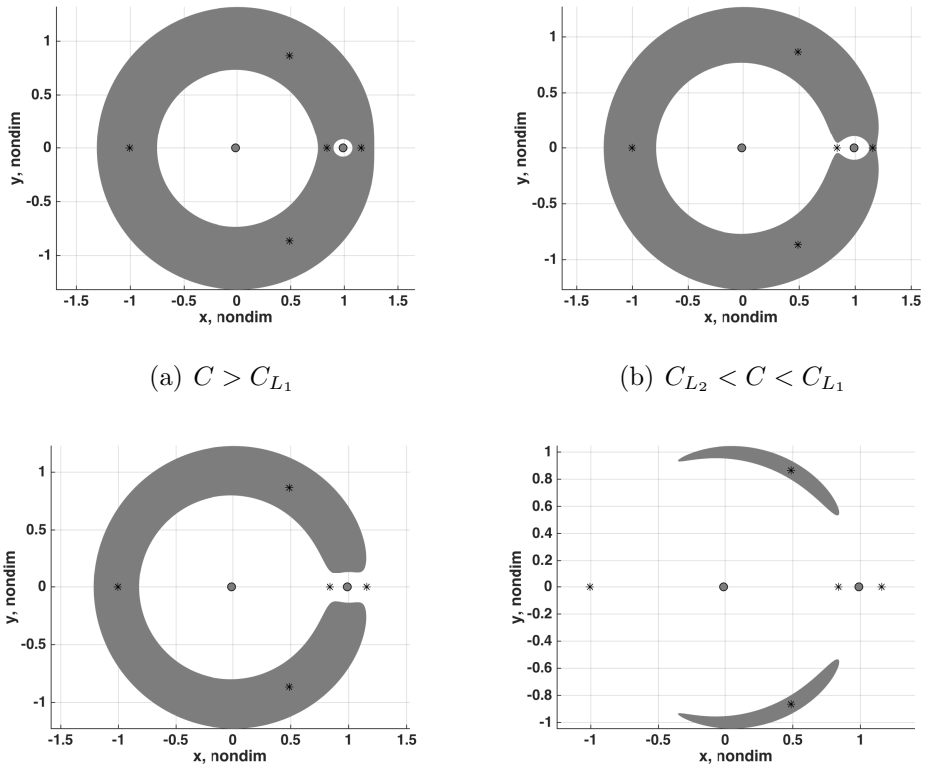

(a) $C > C_{L_1}$

(b) $C_{L_2} < C < C_{L_1}$

(c) $C_{L_3} < C < C_{L_2}$

(d) $C_{L_{4,5}} < C < C_{L_3}$

Figure 2.4.: Zero velocity surfaces (shaded areas) in the Earth-Moon system at a variety of energy levels

The zero velocity surfaces offer useful information about bounds on the motion of P_3. Lower energy levels constrain P_3 to remain near P_1 or P_2. If a transfer between

the two primaries is required, an energy-raising maneuver is implemented to open the L_1 gateway. Similarly, securing a capture around P_1 or P_2 is accomplished by implementing an energy-lowering maneuver to close one or both of the L_1 and L_2 gateways. Paths to L_3, L_4, and L_5 must also possess sufficient energy to shift the forbidden regions as necessary.

2.1.5 Symmetry and Mirroring

Locating solutions of interest, for example, periodic motion, is facilitated by exploiting symmetry across the xz-plane. Consider a set of coordinates (x', y', z') defined such that $x'(t') = x(\tau)$, $y'(t') = -y(\tau)$, and $z'(t') = z(\tau)$, where $t' = -\tau$. This transformed set of coordinates mirrors the conventional set (x, y, z) across the xz-plane in reverse time. Time derivatives are transformed such that $\frac{\mathrm{d}}{\mathrm{d}t'} = -\frac{\mathrm{d}}{\mathrm{d}\tau}$ and $\frac{\mathrm{d}^2}{\mathrm{d}t'^2} = \frac{\mathrm{d}^2}{\mathrm{d}\tau^2}$. Substituting the transformed coordinates into the equations of motion (2.16) - (2.18) yields a set of transformed EOMs:

$$\frac{\mathrm{d}^2x'}{\mathrm{d}t'^2} + 2\,\frac{\mathrm{d}y'}{\mathrm{d}t'} = \frac{\partial\Omega}{\partial x'}\,, \tag{2.32}$$

$$\frac{\mathrm{d}^2y'}{\mathrm{d}t'^2} - 2\,\frac{\mathrm{d}x'}{\mathrm{d}t'} = \frac{\partial\Omega}{\partial y'}\,, \tag{2.33}$$

$$\frac{\mathrm{d}^2z'}{\mathrm{d}t'^2} = \frac{\partial\Omega}{\partial z'}\,. \tag{2.34}$$

This set of equations is identical in structure to equations (2.16) - (2.18); thus, given any solution in the CR3BP, a solution mirrored across the xz-plane also exists. One consequence of this problem symmetry is the mirror theorem.

Theorem 2.1.1 (Mirror Theorem) *If n point masses are acted upon by their mutual gravitational forces only, and at a certain epoch each radius vector from the center of mass of the system is perpendicular to every velocity vector, then the orbit of each mass after that epoch is a mirror image of its orbit prior to that epoch.[13]*

Given the theorem, it follows that any trajectory with two distinct mirror events is periodic in the CR3BP. By extension, any trajectory that possesses two distinct crossings perpendicular to the xz-plane (i.e., $y = \dot{x} = \dot{z} = 0$) is a periodic solution.

2.2 Bicircular Restricted Four-Body Problem

Numerous mission scenarios include spacecraft paths that pass through multiple dynamical environments, some involving a significant influence from three different gravitational fields. To support such multi-system design strategies, a four-body model is derived to include perturbing accelerations from three primary masses on the motion of an infinitesimally small fourth body. A series of reference frames are defined to describe the motion of the primary bodies and a set of governing equations are derived. Due to the increasing complexity of the problem, the governing equations do not admit an integral, though a pseudo-potential function remains available.

2.2.1 Equations of Motion

The bicircular restricted four-body problem (BC4BP) delivers a framework for the analysis of the motion of a body P_4, with mass m_4, under the gravitational influence of three barycentric bodies $P_1, \ldots P_3$ with masses $m_1, \ldots m_3$, respectively. Consistent with the CR3BP, the mass of the body of interest, P_4, is assumed to be negligible compared to the masses of the three primary bodies and, thus, does not affect their motions. By convention, the primaries are ordered such that $m_1 > m_2 > m_3 >> m_4$. Two barycenters are defined in this system and depicted in Figure 2.5(a): B_1 locates the center of mass of the entire system, and B_2 locates the center of mass of the P_2-P_3 system. It is assumed that P_1 and B_2 move about B_1 in circular orbits while P_2 and P_3 encircle B_2. The P_2-P_3 orbital plane is inclined relative to the P_1-B_2 orbital plane by a constant angle γ, as illustrated in Figure 2.5(b), and does not precess over time. This framework is consistent with Sun-planet-moon dynamical environments such as the Sun-Earth-Moon system. Vectors $\vec{R}_{j,4}$ locate P_4 relative to the jth primary and vectors $\vec{R}_j$ locate the jth primary relative to the origin at B_2. Additionally, the vector $\vec{P}$ locates P_4 relative to the system barycenter B_1, an inertially fixed base point.

A series of four reference frames is employed to describe the motion of the BC4BP. An inertial frame $\hat{i}$ consists of the unit vectors ($\hat{\mathbb{X}}$, $\hat{\mathbb{Y}}$, $\hat{\mathbb{Z}}$). The $\hat{s}$ frame rotates with

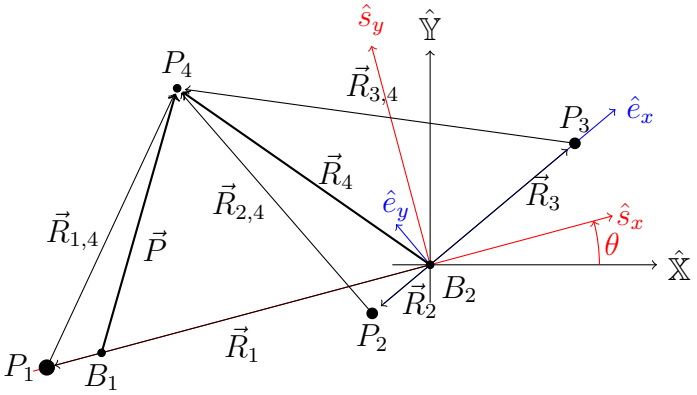

(a) Planar Projection

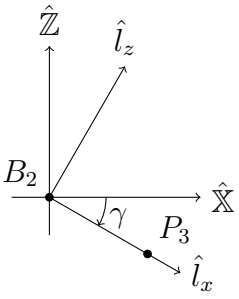

(b) Inertial Frame $\leftrightarrow$ Secondary Orbital Frame

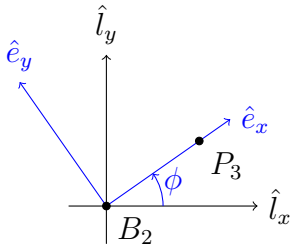

(c) Secondary Orbital Frame $\leftrightarrow$ Secondary Rotating Frame

Figure 2.5.: Frame Definitions

with P_1 about B_2 and is defined such that $\hat{s}_z = \hat{\mathbb{Z}}$. Note that P_1 and B_2 actually orbit B_1, but the rotation rate $\dot{\theta}$ is independent of the choice of origin. The orbital plane defined by the motion of P_2 and P_3 about B_2 coincides with the $(\hat{l}_x, \hat{l}_y)$ plane where $\hat{l}_z$ is directed parallel to the P_2-P_3 orbital angular momentum vector and $\hat{l}_y = \hat{\mathbb{Y}}$. Finally, the $\hat{e}$ frame rotates with P_2 and P_3 about B_2 and is defined such that $\hat{e}_z = \hat{l}_z$. The rotation of the P_1-B_2 system is measured by θ with constant angular rate ${}^i\omega^s$ in the $\hat{s}_z$ direction, and the rotation of the P_2-P_3 system is measured by the angle ϕ with the corresponding constant angular rate ${}^l\omega^e$ in the $\hat{e}_z$ direction. The geometry of the system is linked to epoch time T such that, at some initial epoch T_0:

$$\theta_0 = {}^i\omega^s T_0 \qquad \text{and} \qquad \phi_0 = {}^l\omega^e T_0.$$

A general expression for each angle is then given by

$$\theta = {}^{i}\omega^{s}(T_0 + T), \tag{2.35}$$

$$\gamma = \gamma_0 \quad \forall\ T_0,\, T, \tag{2.36}$$

$$\phi = {}^{l}\omega^{e}(T_0 + T). \tag{2.37}$$

Thus, the system geometry is completely described by an epoch T relative to time T_0.

The derivation of the governing differential equations of motion may be accomplished with various approaches. To minimize the complexity of the formulation, let the $\hat{s}$ frame serve as the working coordinate system with an origin at B_2. Characteristic quantities are selected to nondimensionalize key parameters, such as:

$$l_* = kR_1, \qquad r_* = R_2 + R_3, \qquad m_* = k(m_1 + m_2 + m_3), \qquad t_* = \sqrt{\frac{l_*^3}{Gm_*}}.$$

Note that both the characteristic length l_* and mass m_* are scaled by a positive constant k. This factor facilitates further variable scaling to maintain a relatively uniform order of magnitude between quantities and is particularly useful in Sun-planet-moon architectures where R_1 is much larger than both R_2 and R_3. Nondimensional quantities are represented by lower-case letters, i.e.,

$$\vec{R}_i = \vec{r}_i l_* \qquad \vec{P} = \vec{\rho} l_* \qquad m_2 + m_3 = \mu m_* \qquad m_3 = \nu m_* \qquad t = \tau t_*.$$

The masses of P_1 and P_2 are then reduced as follows:

$$\begin{aligned} \frac{m_1}{m_*} &= \frac{m_1 + m_2 + m_3}{m_*} - \frac{m_2 + m_3}{m_*} = \frac{1}{k} - \mu \quad \rightarrow \quad m_1 = (1/k - \mu)m_*, \\ \frac{m_2}{m_*} &= \frac{m_2 + m_3}{m_*} - \frac{m_3}{m_*} = \mu - \nu \qquad\qquad\quad \rightarrow \quad m_2 = (\mu - \nu)m_*. \end{aligned}$$

A gravitational potential function for the BC4BP system is defined as

$$U = -G\left(\frac{m_1}{R_{1,4}} + \frac{m_2}{R_{2,4}} + \frac{m_3}{R_{3,4}}\right). \tag{2.38}$$

Consequently, the acceleration, as viewed by an observer fixed in the rotating $\hat{s}$ frame, of P_4 is expressed as

$$\frac{\mathrm{d}^2\vec{P}}{\mathrm{d}t^2} = \vec{\nabla}U = -G\frac{m_1}{R_{1,4}}\vec{R}_{1,4} - G\frac{m_2}{R_{2,4}}\vec{R}_{2,4} - G\frac{m_3}{R_{3,4}}\vec{R}_{3,4}. \tag{2.39}$$

Leveraging the characteristic quantities yields a nondimensional second order vector differential equation similar to the one derived to govern motion in the CR3BP:

$$\ddot{\vec{\rho}} = -\frac{(1/k-\mu)}{r_{1,4}^3}\vec{r}_{1,4} - \frac{(\mu-\nu)}{r_{2,4}^3}\vec{r}_{2,4} - \frac{\nu}{r_{3,4}^3}\vec{r}_{3,4}. \tag{2.40}$$

Recall that dots over a quantity denote derivatives with respect to nondimensional time and, for Newton's law to apply, these derivatives are viewed by an inertial observer relative to an inertially fixed point. The system barycenter B_1 may serve as an inertial base point, hence, the vector $\vec{\rho}$ is used to locate the body of interest rather than $\vec{r}_4$. The location of P_4 is expanded as

$$\vec{\rho} = \vec{d} + \vec{r}_4 = (x+d)\hat{s}_x + y\hat{s}_y + z\hat{s}_z, \tag{2.41}$$

where $\vec{d} = d\hat{s}_x$ is a vector from B_1 to B_2.; in this formulation, the magnitude d is a constant. To construct a derivative relative to an inertial observer, apply the basic kinematic equation (BKE):

$$\dot{\vec{\rho}} = \frac{{}^i\mathrm{d}\vec{\rho}}{\mathrm{d}\tau} = \frac{{}^s\mathrm{d}\vec{\rho}}{\mathrm{d}\tau} + {}^i\vec{\omega}^s \times \vec{\rho}, \tag{2.42}$$

where the angular rate ${}^i\omega^s$ is equivalent to the mean motion of the P_1-B_2 system:

$${}^i\omega^s = N_1 = \sqrt{\frac{G(m_1+m_2+m_3)}{(D_1+D_2)^3}} = \sqrt{\frac{G\frac{1}{k}m_*}{\frac{1}{k^3}l_*^3}} = k\sqrt{\frac{Gm_*}{l_*^3}}. \tag{2.43}$$

Multiplying by the characteristic time yields a nondimensional quantity, i.e., $n_1 = N_1 t_* = k$. The inertial derivative of $\vec{\rho}$ is thus evaluated as

$$\begin{aligned}\dot{\vec{\rho}} &= \dot{x}\hat{s}_x + \dot{y}\hat{s}_y + \dot{z}\hat{s}_z + k\hat{s}_z \times \vec{\rho} \\ \dot{\vec{\rho}} &= (\dot{x} - ky)\hat{s}_x + (\dot{y} + k[x+d])\hat{s}_y + \dot{z}\hat{s}_z.\end{aligned} \tag{2.44}$$

Again, applying the BKE yields the inertial acceleration in rotating coordinates:

$$\ddot{\vec{\rho}} = \left[\ddot{x} - 2k\dot{y} - k^2(x+d)\right]\hat{s}_x + \left[\ddot{y} + 2k\dot{x} - k^2 y\right]\hat{s}_y + \ddot{z}\hat{s}_z. \tag{2.45}$$

The distance d is easily expressed in terms of nondimensional quantities by recognizing that d locates the system center of mass relative to B_2:

$$D = \frac{0(m_2+m_3) + R_1 m_1}{m_1+m_2+m_3} = \frac{\frac{1}{k}l_*(\frac{1}{k}-\mu)m_*}{\frac{1}{k}m_*} = l_*(\frac{1}{k}-\mu). \tag{2.46}$$

Nondimensionalizing this quantity yields $d = 1/k - \mu$. As the distance between P_1 and B_2 is $r_1 = 1/k$, it follows that the distance between B_1 and P_1 is simply μ. A similar analysis is completed on the P_2-P_3 system, and the positions of all three primaries are expressed in terms of nondimensional quantities:

$$\vec{r_1} = -\frac{1}{k}\hat{s}_x, \tag{2.47}$$

$$\vec{r_2} = -\frac{\nu}{\mu}\frac{r_*}{l_*}\hat{e}_x, \tag{2.48}$$

$$\vec{r_3} = \left(1 - \frac{\nu}{\mu}\right)\frac{r_*}{l_*}\hat{e}_x. \tag{2.49}$$

To include these expressions in later derivations, the $\hat{e}_x$ unit vector must be expressed in terms of the working frame $\hat{s}$. The $\hat{e}$ unit vectors may be expressed in terms of the $\hat{s}$ frame by transforming $\hat{e}$ to $\hat{s}$. The resulting expression for the $\hat{e}_x$ direction is

$$\hat{e}_x = \left(C_\theta C_\phi C_\gamma + S_\theta S_\phi\right)\hat{s}_x + \sin(\phi - \theta)\hat{s}_y - C_\phi S_\gamma \hat{s}_z, \tag{2.50}$$

where C_A represents $\cos(A)$ and S_B represents $\sin(B)$. Note that, if the P_2-P_3 orbital plane is not inclined relative to the working frame, the angle γ is equal to zero and equation (2.50) simplifies to

$$\hat{e}_x = \cos(\phi - \theta)\hat{s}_x + \sin(\phi - \theta)\hat{s}_y. \tag{2.51}$$

Substituting the full relationship (when $\gamma \neq 0$) into the positions of the primaries yields:

$$\vec{r_1} = -\frac{1}{k}\hat{s}_x, \tag{2.52}$$

$$\vec{r_2} = -\frac{\nu}{\mu}\frac{r_*}{l_*}\left(C_\theta C_\phi C_\gamma + S_\theta S_\phi\right)\hat{s}_x - \frac{\nu}{\mu}\frac{r_*}{l_*}\sin(\phi - \theta)\hat{s}_y + \frac{\nu}{\mu}\frac{r_*}{l_*}C_\phi S_\gamma \hat{s}_z, \tag{2.53}$$

$$\vec{r_3} = \left(1 - \frac{\nu}{\mu}\right)\left(C_\theta C_\phi C_\gamma + S_\theta S_\phi\right)\hat{s}_x + \left(1 - \frac{\nu}{\mu}\right)\sin(\phi - \theta)\hat{s}_y - \left(1 - \frac{\nu}{\mu}\right)C_\phi S_\gamma \hat{s}_z. \tag{2.54}$$

To shorten the notation, let the positions of the primaries be represented by

$$\vec{r_1} = x_1\hat{s}_x + y_1\hat{s}_y + z_1\hat{s}_z, \tag{2.55}$$

$$\vec{r_2} = x_2\hat{s}_x + y_2\hat{s}_y + z_2\hat{s}_z, \tag{2.56}$$

$$\vec{r_3} = x_3\hat{s}_x + y_3\hat{s}_y + z_3\hat{s}_z. \tag{2.57}$$

The equations of motion expressed in equation (2.40) are, therefore, expanded as

$$\ddot{x} = 2k\dot{y} + k^2(x + \frac{1}{k} - \mu) - \frac{(\frac{1}{k} - \mu)(x - x_1)}{r_{1,4}^3} - \frac{(\mu - \nu)(x - x_2)}{r_{2,4}^3} - \frac{\nu(x - x_3)}{r_{3,4}^3}, \tag{2.58}$$

$$\ddot{y} = -2k\dot{x} + k^2 y - \frac{(\frac{1}{k} - \mu)y}{r_{1,4}^3} - \frac{(\mu - \nu)(y - y_2)}{r_{2,4}^3} - \frac{\nu(y - y_3)}{r_{3,4}^3}, \tag{2.59}$$

$$\ddot{z} = -\frac{(\frac{1}{k} - \mu)z}{r_{1,4}^3} - \frac{(\mu - \nu)(z - z_2)}{r_{2,4}^3} - \frac{\nu(z - z_3)}{r_{3,4}^3}. \tag{2.60}$$

Recall the potential function $U = -G\left(\frac{m_1}{R_{1,4}} + \frac{m_2}{R_{2,4}} + \frac{m_3}{R_{3,4}}\right)$ from an inertial formulation. A similar *pseudo-potential* Υ emerges for the rotating frame formulation:

$$\Upsilon = k^2(1/k - \mu)x + \frac{1}{2}k^2(x^2 + y^2) + \frac{1/k - \mu}{r_{1,4}} + \frac{\mu - \nu}{r_{2,4}} + \frac{\nu}{r_{3,4}}. \tag{2.61}$$

The equations of motion may then be compactly written:

$$\ddot{x} - 2k\dot{y} = \frac{\partial \Upsilon}{\partial x}\,, \tag{2.62}$$

$$\ddot{y} + 2k\dot{x} = \frac{\partial \Upsilon}{\partial y}\,, \tag{2.63}$$

$$\ddot{z} = \frac{\partial \Upsilon}{\partial z}\,. \tag{2.64}$$

Numerical integration of these equations supplies the motion of the particle P_4 under the influence of the three larger primary masses.

2.2.2 Search for an Integral of Motion

The BC4BP pseudo-potential function, in contrast to the CR3BP pseudo-potential, is time dependent due to the motions of P_2 and P_3. Although P_1 remains fixed, P_2 and P_3 both possess nonzero velocities relative to the rotating frame; these velocity

vectors are expressed as scalar multiples of the angular velocity of the $\hat{e}$ frame relative to the $\hat{s}$ frame. This angular velocity, ${}^{s}\vec{\omega}^{e}$, is derived via the time derivative of equation (2.50):

$$
\begin{aligned}
{}^{s}\vec{\omega}^{e} = &\left[\dot{\theta}(S_{\phi}C_{\theta} - C_{\phi}S_{\theta}C_{\gamma}) + \dot{\phi}(C_{\phi}S_{\theta} - S_{\phi}C_{\theta}C_{\gamma})\right]\hat{s}_{x} + \\
&(\dot{\phi} - \dot{\theta})\cos(\phi - \theta)\hat{s}_{y} + \dot{\phi}S_{\phi}S_{\gamma}\hat{s}_{z},
\end{aligned} \tag{2.65}
$$

where $\dot{\theta} = n_1 = k$ and $\dot{\phi}$ is the nondimensional mean motion of the P_2-P_3 system:

$$
\dot{\phi} = n_2 = {}^{l}\omega^{e} = \sqrt{\mu\frac{l_{*}^{3}}{r_{*}^{3}}}. \tag{2.66}
$$

The velocities of the three primaries are, therefore, generally represented by

$$
\dot{\vec{r}}_1 = \vec{v}_1 = \vec{0}, \tag{2.67}
$$

$$
\dot{\vec{r}}_2 = \vec{v}_2 = \frac{-\nu}{\mu}\frac{r_{*}}{l_{*}}{}^{s}\vec{\omega}^{e}, \tag{2.68}
$$

$$
\dot{\vec{r}}_3 = \vec{v}_3 = \left(1 - \frac{\nu}{\mu}\right)\frac{r_{*}}{l_{*}}{}^{s}\vec{\omega}^{e}. \tag{2.69}
$$

Because the nonconstant vectors $\vec{r}_1$, $\vec{r}_2$, and $\vec{r}_3$ appear explicitly in the pseudo-potential function Υ, the total derivative possesses a nonzero time derivative $\frac{\partial\Upsilon}{\partial\tau}$. Therefore, the total derivative of Υ cannot be integrated to obtain a constant of the motion.

2.2.3 Equilibrium Solutions

Similar to the equilibrium solutions in the CR3BP, the BC4BP possesses a set of five equilibrium points. However, in contrast to the CR3BP, these solutions are not fixed points as viewed in the $\hat{s}$ frame. Viewed as locations with instantaneous velocity and acceleration of zero, these points oscillate, or *librate*, over time as the system geometry varies. Consistent with the CR3BP, equilibrium solutions are located by solving the following vector equation:

$$
\vec{\nabla}\Omega = \vec{0}. \tag{2.70}
$$

Due to the additional complexity of the BC4BP, however, analytical solutions to this equation are not readily apparent. However, the equilibrium points associated with the P_1-P_2 CR3BP supply good approximations for the BC4BP equilibrium solutions, and, given the CR3BP approximations as an initial guess, numerical methods easily converge upon the BC4BP equilibrium point locations. The BC4BP solutions oscillate with a period commensurate with the orbit of P_2 and P_3 in the rotating frame and possess out-of-plane components when $\gamma \neq 0$.

2.3 Coordinate Frame Transformations

It is often useful to transform various quantities from one frame to another, for example, when transitioning a quantity or state vector in the CR3BP solution to a higher fidelity model such as the BC4BP or an inertial ephemeris system. Consider two reference frames $\hat{o}$ and $\hat{f}$ as illustrated in Figure 2.6. Although the unit vectors ($\hat{o}_1$, $\hat{o}_2$) appear to be coplanar with ($\hat{f}_1$, $\hat{f}_2$), it is not necessary. The position of point B is located relative to point P with a vector expressed in terms of coordinates in the $\hat{o}$ working frame, that is, $\underset{o}{\vec{r}_{PB}}$, where the "$o$" beneath the vector represents the working frame. The velocity of point B is similarly denoted as ${}^{o}\dot{\underset{o}{\vec{r}}}_{PB}$, where the left superscript denotes the observer frame associated with the derivative. To transform the coordinates of any vector, the vectors must share a common base point such as point A in Figure 2.6. If no such point exists, an intermediate frame is required to transition from $\hat{o}$ to $\hat{f}$. A matrix $\underset{o,f}{\mathbf{R}}$ describes a set of rotations to shift between the $\hat{o}$ and $\hat{f}$ working frames. Finally, the angular velocity of frame $\hat{o}$ with respect to frame $\hat{f}$ is denoted by ${}^{f}\vec{\omega}^{o}$, and is conveniently expressed in terms of either working frame. To express the position of B in the $\hat{f}$ frame, the following steps are completed:

1. Shift base point: $\underset{o}{\vec{r}_{AB}} = \underset{o}{\vec{r}_{PB}} - \underset{o}{\vec{r}_{PA}}$.
2. Change working frame: $\underset{f}{\vec{r}_{AB}} = \underset{o}{\vec{r}_{AB}}\underset{o,f}{\mathbf{R}}$.
3. Shift base point: $\underset{f}{\vec{r}_{GB}} = \underset{f}{\vec{r}_{AB}} + \underset{f}{\vec{r}_{GA}}$.

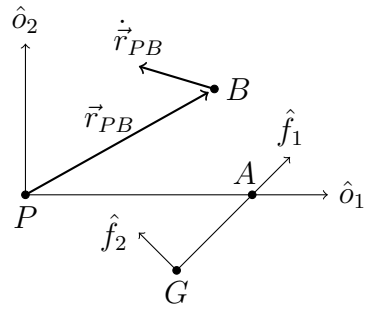

Figure 2.6.: Arbitrary Reference Frames

This process is expressed in one concise expression as

$$\underset{f}{\vec{r}_{GB}} = (\underset{o}{\vec{r}_{PB}} - \underset{o}{\vec{r}_{PA}})\underset{o,f}{\mathbf{R}} + \underset{f}{\vec{r}_{GA}}. \tag{2.71}$$

To express the components of the velocity of B in terms of the $\hat{f}$ frame, first recognize that, because points A and P are both fixed in the $\hat{o}$ frame, the velocities $\underset{o}{{}^{o}\dot{\vec{r}}_{PB}}$ and $\underset{o}{{}^{o}\dot{\vec{r}}_{AB}}$ are equivalent. Likewise, $\underset{f}{{}^{f}\dot{\vec{r}}_{GB}} = \underset{f}{{}^{f}\dot{\vec{r}}_{AB}}$. Thus, to transform the velocity of B between coordinate frames the following steps are completed:

1. Change observer: $\underset{o}{{}^{f}\dot{\vec{r}}_{AB}} = \underset{o}{{}^{o}\dot{\vec{r}}_{AB}} + \underset{o}{{}^{f}\vec{\omega}^{o}} \times \underset{o}{\vec{r}_{AB}}$.
2. Change working frame: $\underset{f}{{}^{f}\dot{\vec{r}}_{AB}} = \underset{o}{{}^{f}\dot{\vec{r}}_{AB}}\underset{o,f}{\mathbf{R}}$.

Again, this process is expressed as a single equation:

$$\underset{f}{{}^{f}\dot{\vec{r}}_{GB}} = \left(\underset{o}{{}^{o}\dot{\vec{r}}_{AB}} + \underset{o}{{}^{f}\vec{\omega}^{o}} \times \underset{o}{\vec{r}_{AB}}\right)\underset{o,f}{\mathbf{R}}. \tag{2.72}$$

Both operations are combined into a single matrix multiplication operation, as deduced by Haapala [14]:

$$\begin{Bmatrix} \vec{r}_{GB} - \vec{r}_{GA} \\ \dot{\vec{r}}_{GB} \end{Bmatrix}_{f} = \begin{bmatrix} \mathbf{R} & \mathbf{0_{3\times 3}} \\ \dot{\mathbf{R}} & \mathbf{R} \end{bmatrix} \begin{Bmatrix} \vec{r}_{PB} - \vec{r}_{PA} \\ \dot{\vec{r}}_{PB} \end{Bmatrix}_{o}, \tag{2.73}$$

where $\mathbf{R}$ is the rotation matrix $\underset{o,f}{\mathbf{R}}$ and $\dot{\mathbf{R}}$ is the time derivative of $\mathbf{R}$. Such transformations facilitate comparisons of solution geometries between rotating systems and are particularly useful when transitioning solutions between lower and higher fidelity models.

3. DYNAMICAL SYSTEMS THEORY

Dynamical Systems Theory (DST) offers many tools and techniques that facilitate the analysis of the nonlinear dynamics in the CR3BP and BC4BP. Taylor Series expansions supply linear approximations to the nonlinear dynamical behavior and offer stability information about nonlinear solutions, as well as predictions about motion near a baseline solution. Differential corrections methods facilitate the transition between linear and nonlinear dynamics and yield tools capable of identifying an evolving motion that meets a set of desired constraints. Shooting techniques derived from differential corrections methods are applied to compute periodic orbits and continuation schemes are employed to expand a single solution into a family of similar arcs. The stable, unstable, and center manifolds associated with periodic solutions are leveraged to identify a diverse range of motion in the CR3BP. Finally, the analysis of the six-dimensional spatial CR3BP is facilitated by Poincaré mapping techniques.

3.1 Approximating Nonlinear Dynamics via Linearization

Although the nonlinear equations that govern motion in the CR3BP and BC4BP possess no closed-form solutions, linearizations of the equations relative to a reference solution supply significant insight into the nonlinear motion. These linearizations form a set of variational equations of motion that *are* analytically solvable. To illustrate these techniques, linearizations relative to the CR3BP equilibrium points are investigated as sources of periodic and quasi-periodic motion. A more generalized linearization is represented by the State Transition Matrix and the stable, unstable, and center subspaces of this matrix are leveraged to identify additional useful structures.

3.1.1 Variational Equations of Motion

The CR3BP is governed by a set of nonlinear, coupled, second-order differential equations that possess no analytical solution but are approximated by *variational* equations. If higher-order terms are neglected, these equations are reduced to linear EOMs that are analytically solvable and offer insight into system stability and predict the nearby behavior. In general, the nonlinear system of equations is expressed by the vector differential equation,

$$\dot{\vec{q}} = \vec{f}(\vec{q},\ t), \tag{3.1}$$

where $\vec{q} = \{\vec{r}_{1,3}, \vec{v}\}^T$. Consider a specific reference solution $\vec{q}_*(t)$ with initial conditions $\vec{q}_*(t_0)$. A nearby solution has the form $\vec{q}(t) = \vec{q}_*(t) + \delta\vec{q}(t)$ where $\delta\vec{q}(t)$ is some small variation from the reference solution. Substituting the nearby solution into equation (3.1) yields

$$\dot{\vec{q}} = \dot{\vec{q}}_* + \delta\dot{\vec{q}} = \vec{f}(\vec{q}_* + \delta\vec{q},\ t). \tag{3.2}$$

A linear relationship between the reference and nearby solution is constructed by applying a Taylor Series expansion to $\vec{f}$ about the reference solution $\vec{q}_*$:

$$\dot{\vec{q}}_* + \delta\dot{\vec{q}} \approx \vec{f}(\vec{q}_*, t) + \left.\frac{\partial \vec{f}}{\partial \vec{q}}\right|_{\vec{q}_*} \delta\vec{q} + \text{H.O.T.s}\ldots \tag{3.3}$$

By ignoring all terms of order two or higher (i.e., H.O.T.s), the Taylor Series expansion is further reduced by recognizing that $\vec{q}_*$ is a solution to equation (3.1), i.e., $\dot{\vec{q}}_* = \vec{f}(\vec{q}_*, t)$:

$$\delta\dot{\vec{q}} \approx \left.\frac{\partial \vec{f}}{\partial \vec{q}}\right|_{\vec{q}_*} \delta\vec{q} = \mathbf{A}(t)\delta\vec{q}, \tag{3.4}$$

where $\delta\vec{q} = \{\xi\ \ \eta\ \ \zeta\ \ \dot{\xi}\ \ \dot{\eta}\ \ \dot{\zeta}\}^T$, expressed in the rotating coordinate frame, and $\mathbf{A}$ is a 6×6 matrix that contains the partial derivatives of $\vec{f}$ with respect to the state $\vec{q}$

evaluated on the reference, $\vec{q}_*$. This relationship is expressed more as a set of scalar equations, in matrix form,

$$\begin{Bmatrix} \dot{\xi} \\ \dot{\eta} \\ \dot{\zeta} \\ \ddot{\xi} \\ \ddot{\eta} \\ \ddot{\zeta} \end{Bmatrix} = \begin{bmatrix} 0 & 0 & 0 & 1 & 0 & 0 \\ 0 & 0 & 0 & 0 & 1 & 0 \\ 0 & 0 & 0 & 0 & 0 & 1 \\ \Omega_{xx} & \Omega_{xy} & \Omega_{xz} & 0 & 2 & 0 \\ \Omega_{yx} & \Omega_{yy} & \Omega_{yz} & -2 & 0 & 0 \\ \Omega_{zx} & \Omega_{zy} & \Omega_{zz} & 0 & 0 & 0 \end{bmatrix} \begin{Bmatrix} \xi \\ \eta \\ \zeta \\ \dot{\xi} \\ \dot{\eta} \\ \dot{\zeta} \end{Bmatrix}, \tag{3.5}$$

where $\Omega_{ab} = \frac{\partial^2 \Omega}{\partial a \partial b}$ are the second derivatives of the pseudo-potential function evaluated on the reference solution. Evaluating this matrix equation yields the scalar, variational equations of motion:

$$\ddot{\xi} - 2\dot{\eta} = \Omega_{xx}\xi + \Omega_{xy}\eta + \Omega_{xz}\zeta, \tag{3.6}$$

$$\ddot{\eta} + 2\dot{\xi} = \Omega_{yx}\xi + \Omega_{yy}\eta + \Omega_{yz}\zeta, \tag{3.7}$$

$$\ddot{\zeta} = \Omega_{zx}\xi + \Omega_{zy}\eta + \Omega_{zz}\zeta. \tag{3.8}$$

Similar equations are derived for the linear relative dynamics in the BC4BP.

3.1.2 Motion Near the Equilibrium Points

A greater understanding of the stability and local dynamics near the equilibrium solutions is achieved by linearizing the equations of motion about each equilibrium point, i.e., about $\vec{q}_* = \vec{q}_{L_i}$. As all of the equilibrium solutions exist in the xy-plane, any Ω terms with out-of-plane components reduce to zero and equations (3.6) - (3.8) are rewritten as

$$\ddot{\xi} - 2\dot{\eta} = \Omega_{xx}\xi + \Omega_{xy}\eta, \tag{3.9}$$

$$\ddot{\eta} + 2\dot{\xi} = \Omega_{yx}\xi + \Omega_{yy}\eta, \tag{3.10}$$

$$\ddot{\zeta} = \Omega_{zz}\zeta. \tag{3.11}$$

Note that equation (3.11), which governs the linear out-of-plane motion near the equilibrium points, is completely decoupled from the in-plane motion. Regardless of the CR3BP system, Ω_{zz} is positive at all five equilibrium points, thus this simple second-order differential equation admits an oscillatory solution with frequency $\omega_z = \sqrt{|\Omega_{zz}|}$. At the triangular points, Ω_{zz} is equal to one, indicating that any out-of-plane motion near L_4 and L_5 incurs a period of 2π, equivalent to the period of the two primaries.

The system describing the in-plane motion is reduced from a six- to a four-dimensional problem and the associated $\mathbf{A}$ matrix includes only the terms corresponding to equations (3.9) and (3.10). The stability of the in-plane motion is investigated by analyzing the roots of the characteristic polynomial, i.e., the eigenvalues, associated with the $\mathbf{A}$ matrix and evaluated at the reference solution. These eigenvalues are computed by evaluating the determinant of $(\lambda\mathbf{I} - \mathbf{A})$ and solving for the roots of the resulting equation:

$$\det \begin{bmatrix} \lambda & 0 & -1 & 0 \\ 0 & \lambda & 0 & -1 \\ -\Omega_{xx} & -\Omega_{xy} & \lambda & -2 \\ -\Omega_{xy} & -\Omega_{yy} & 2 & \lambda \end{bmatrix} = \lambda^4 + \lambda^2(4 - \Omega_{yy} - \Omega_{xx}) + \Omega_{xx}\Omega_{yy} - \Omega_{xy}^2 = 0. \quad (3.12)$$

The solution to this characteristic equation is simplified by first considering only the collinear equilibrium points which lie along the x-axis. In this case, the Ω_{xy} term reduces to zero and the characteristic equation simplifies to

$$\lambda^4 + \lambda^2(4 - \Omega_{yy} - \Omega_{xx}) + \Omega_{xx}\Omega_{yy}, \quad (3.13)$$

which is represented as a second order polynomial,

$$\Lambda^2 + 2\beta_1\Lambda - \beta_2^2 = 0, \quad (3.14)$$

where $\lambda = \pm\sqrt{\Lambda}$, $\beta_1 = 2 - \frac{1}{2}(\Omega_{xx} - \Omega_{yy})$, and $\beta_2^2 = -\Omega_{xx}\Omega_{yy}$. When evaluated at the three collinear points, Ω_{xx} is positive, and Ω_{yy} is negative, thus β_2 is positive. Applying the quadratic formula yields the roots of this equation:

$$\Lambda_1 = -\beta_1 + \sqrt{\beta_1^2 + \beta_2^2}, \tag{3.15}$$

$$\Lambda_2 = -\beta_1 - \sqrt{\beta_1^2 + \beta_2^2}. \tag{3.16}$$

Regardless of the sign of β_1, the square root term is real and larger than the magnitude of β_1 because $\beta_2^2 > 0$ for all collinear points. Hence, Λ_1 is positive and Λ_2 is negative. Accordingly, the eigenvalues of fourth-order characteristic equation (3.12) are given by

$$\lambda_{1,2} = \pm\sqrt{\Lambda_1} \quad \in \mathcal{R}, \tag{3.17}$$

$$\lambda_{3,4} = \pm\sqrt{\Lambda_2} \quad \in \mathcal{I}. \tag{3.18}$$

Note that, due to the signs of Λ_1 and Λ_2, λ_1 and λ_2 are real while λ_3 and λ_4 are imaginary. Solutions to equations (3.9) and (3.10) are expressed as linear combinations of the exponentials of the eigenvalues:

$$\vec{q} = \alpha_1\vec{v}_1 e^{\lambda_1 t} + \alpha_2\vec{v}_2 e^{\lambda_2 t} + \alpha_3\vec{v}_3 e^{\lambda_3 t} + \alpha_4\vec{v}_4 e^{\lambda_4 t}, \tag{3.19}$$

where $\vec{v}_i$ is the eigenvector associated with λ_i and α_i is a scaling constant. The first two terms, or *modes*, which are associated with real eigenvalues, converge or diverge exponentially over time based on the sign of λ_1 and λ_2. The final two modes, which are associated with imaginary eigenvalues, oscillate with a frequency consistent with the eigenvalue magnitude. Initial conditions may be selected to isolate the convergent/divergent mode or to isolate the oscillatory mode. The former yields trajectories that approach or depart the equilibrium solution over time, while the latter yields periodic motion in the vicinity of the equilibrium point. Though these simple modes exist only as a by-product of linearization, their effects are observed and leveraged in the full nonlinear system to generate analogous motion.

A similar analysis is completed for the linear dynamics near the triangular points. Though $y \neq 0$ at these solutions, the exact positions of L_4 and L_5 are expressed as a

function of the system mass ratio μ: $(x,\ y) = (0.5-\mu,\ \pm\sqrt{3}/2)$. Substituting these values into the second derivatives of the pseudo-potential function yields $\Omega_{xx} = 3/4$, $\Omega_{yy} = 9/4$, and $\Omega_{xy} = 3\sqrt{3}(1-2\mu)/4$. The fourth-order characteristic equation (3.12) then reduces to

$$\lambda^4 + \lambda^2 + \frac{27}{4}\left(\mu(1-\mu)\right) = 0. \tag{3.20}$$

Substituting $\Lambda = \lambda^2$ again returns expressions for the roots of this equation:

$$\Lambda_1 = \frac{-1}{2} + \frac{1}{2}\sqrt{1 - 27\mu(1-\mu)}, \tag{3.21}$$

$$\Lambda_2 = \frac{-1}{2} - \frac{1}{2}\sqrt{1 - 27\mu(1-\mu)}, \tag{3.22}$$

where $\lambda_{1,2} = \pm\sqrt{\Lambda_1}$ and $\lambda_{3,4} = \pm\sqrt{\Lambda_2}$. For most CR3BP systems of interest, such as the Sun-Earth and Earth-Moon CR3BP, the term $1-27\mu(1-\mu)$ lies between zero and one, which results in $\Lambda_2 < \Lambda_1 < 0$. The eigenvalues λ_i are therefore imaginary, and planar motion in the vicinity of L_4 and L_5 is comprised of linear combinations of oscillatory solutions with frequencies $|\lambda_{1,2}|$ and $|\lambda_{3,4}|$.

3.1.3 State Transition Matrix

Linearization techniques are extended to a more general set of reference solutions to gain additional insight. In the previous section, specific analytical solutions are derived to describe motion in the vicinity of the CR3BP equilibrium points. For example, for motion relative to the equilibrium points, $\mathbf{A}$ in equation (3.4) is a constant matrix. A more general solution to the differential equation in equation (3.4), one that accommodates potentially time-varying reference solutions, takes the form

$$\delta\vec{q}(t) = \mathbf{\Phi}(t, t_0)\delta\vec{q}(t_0), \tag{3.23}$$

where $\mathbf{\Phi}$ is termed the *state transition matrix* (STM), or *sensitivity matrix*, and is defined as

$$\mathbf{\Phi}(t, t_0) \equiv e^{\mathbf{A}(t-t_0)}. \tag{3.24}$$

This matrix represents a linear map between perturbations in an initial state $\vec{q}_0 = \vec{q}(t_0)$ and perturbations in some later state $\vec{q}_f = \vec{q}(t)$. Written more explicitly, this relationship is given by

$$\begin{Bmatrix} \delta x_f \\ \delta y_f \\ \delta z_f \\ \delta \dot{x}_f \\ \delta \dot{y}_f \\ \delta \dot{z}_f \end{Bmatrix} = \begin{bmatrix} \frac{\partial x}{\partial x_0} & \frac{\partial x}{\partial y_0} & \frac{\partial x}{\partial z_0} & \frac{\partial x}{\partial \dot{x}_0} & \frac{\partial x}{\partial \dot{y}_0} & \frac{\partial x}{\partial \dot{z}_0} \\ \frac{\partial y}{\partial x_0} & \frac{\partial y}{\partial y_0} & \frac{\partial y}{\partial z_0} & \frac{\partial y}{\partial \dot{x}_0} & \frac{\partial y}{\partial \dot{y}_0} & \frac{\partial y}{\partial \dot{z}_0} \\ \frac{\partial z}{\partial x_0} & \frac{\partial z}{\partial y_0} & \frac{\partial z}{\partial z_0} & \frac{\partial z}{\partial \dot{x}_0} & \frac{\partial z}{\partial \dot{y}_0} & \frac{\partial z}{\partial \dot{z}_0} \\ \frac{\partial \dot{x}}{\partial x_0} & \frac{\partial \dot{x}}{\partial y_0} & \frac{\partial \dot{x}}{\partial z_0} & \frac{\partial \dot{x}}{\partial \dot{x}_0} & \frac{\partial \dot{x}}{\partial \dot{y}_0} & \frac{\partial \dot{x}}{\partial \dot{z}_0} \\ \frac{\partial \dot{y}}{\partial x_0} & \frac{\partial \dot{y}}{\partial y_0} & \frac{\partial \dot{y}}{\partial z_0} & \frac{\partial \dot{y}}{\partial \dot{x}_0} & \frac{\partial \dot{y}}{\partial \dot{y}_0} & \frac{\partial \dot{y}}{\partial \dot{z}_0} \\ \frac{\partial \dot{z}}{\partial x_0} & \frac{\partial \dot{z}}{\partial y_0} & \frac{\partial \dot{z}}{\partial z_0} & \frac{\partial \dot{z}}{\partial \dot{x}_0} & \frac{\partial \dot{z}}{\partial \dot{y}_0} & \frac{\partial \dot{z}}{\partial \dot{z}_0} \end{bmatrix} \begin{Bmatrix} \delta x_0 \\ \delta y_0 \\ \delta z_0 \\ \delta \dot{x}_0 \\ \delta \dot{y}_0 \\ \delta \dot{z}_f \end{Bmatrix} = \begin{bmatrix} \mathbf{\Phi_{rr}} & \mathbf{\Phi_{rv}} \\ \mathbf{\Phi_{vr}} & \mathbf{\Phi_{vv}} \end{bmatrix} \delta \vec{q}_0, \tag{3.25}$$

where the STM $\mathbf{\Phi}$ is the 6×6 matrix of partial derivatives evaluated along the reference path. The STM possesses several useful properties,

$$\mathbf{\Phi}(t_2, t_0) = \mathbf{\Phi}(t_2, t_1)\mathbf{\Phi}(t_1, t_0), \tag{3.26}$$

$$\mathbf{\Phi}(t_0, t) = \mathbf{\Phi}^{-1}(t_1, t_0), \tag{3.27}$$

$$\det(\mathbf{\Phi}) = 1, \tag{3.28}$$

and may be separated into four quadrants, each of which relates perturbations in $\vec{q}_0$ to perturbations in $\vec{q}_f$. For example, assuming that the state vectors represent position and velocity, the top-left 3×3 quadrant $\mathbf{\Phi_{rr}}$ relates changes in the position state at $\tau = t_0$ to changes in the position state at $\tau = t$. Similarly, the top-right quadrant $\mathbf{\Phi_{rv}}$ relates changes in the velocity state at $\tau = t_0$ to changes in the position state at $\tau = t$.

The STM is computed in parallel with the state vector via numerical integration. A matrix differential equation is obtained by substituting the general solution back into equation (3.4):

$$\dot{\mathbf{\Phi}}(t, t_0) = \mathbf{A}(t)\mathbf{\Phi}(t, t_0). \tag{3.29}$$

This equation is numerically integrated along with the equations of motion to compute a time history for the STM. Because the neither the CR3BP nor the BC4BP possess an analytical solution, the predictive properties of the STM are crucial to investigating the dynamical behavior near a reference solution.

3.1.4 Stability and Invariant Manifolds

Descriptions of the stability of the reference solution and the flow in its vicinity are straightforwardly obtained from the eigenstructure of the linear dynamics relative to a fixed reference. Two types of fixed reference solutions are considered: the equilibrium solutions of the EOMs and periodic orbits. A condensed overview of the theory underlying this analysis is presented here; for a more complete discussion see [14].

Invariant Manifolds of an Equilibrium Point

The invariant manifolds in the vicinity of the equilibrium points are employed to describe the nearby motion. Recall the general linearization from equation (3.4), $\dot{\delta\vec{q}} = \mathbf{A}(t)\delta\vec{q}$, where $\delta\vec{q} = \vec{q} - \vec{q}_*$ and $\vec{q}_*$ is the reference solution of interest. If this reference is one of the equilibrium points, i.e., $\vec{q}_* = \vec{q}_{L_i}$, the $\mathbf{A}$ matrix is constant and, as noted previously, the general solution to equation (3.4) is written

$$\delta\vec{q}(t) = \mathbf{\Phi}(t, t_0)\delta\vec{q}(t_0) = e^{\mathbf{A}(t-t_0)}\delta\vec{q}(t_0). \tag{3.30}$$

The matrix $\mathbf{A}$ is decomposed into the form $\mathbf{A} = \mathbf{S\Gamma S}^{-1}$, where $\mathbf{S}$ is an $n \times n$ matrix with columns equal to the eigenvectors $\vec{\eta}_i$ of $\mathbf{A}$ and $\mathbf{\Gamma}$ is a diagonal $n \times n$ matrix comprised of the corresponding eigenvalues γ_i. The solution expressed in equation (3.30) is then rewritten:

$$\delta\vec{q}(t) = \mathbf{S}e^{\mathbf{\Gamma}(t-t_0)}\mathbf{S}^{-1}\delta\vec{q}(t_0). \tag{3.31}$$

When the matrix form is expanded, equation (3.31) yields the vector:

$$\delta\vec{q}(t) = \sum_{i=1}^{6} \alpha_i e^{\gamma_i(t-t_0)}\vec{\eta}_i, \tag{3.32}$$

where α_i is a scaling constant and is determined by the choice of initial condition $\delta\vec{q}(t_0)$. Note that this expansion is equivalent to, though more general than, the solution for motion near the collinear points derived previously and expressed in equation (3.19). Equation (3.32) represents the solution as a linear combination of the eigenvectors of $\mathbf{A}$. In other words, the solution $\vec{q}(t)$ is the superposition of n terms, or modes. The contribution from each mode flows in the direction of the eigenvector $\vec{\eta}_i$ and is characterized by the eigenvalue γ_i. Due to the Hamiltonian nature of the CR3BP as well as the BC4BP, the eigenvalues of $\mathbf{A}$ occur in pairs. That is, eigenvalues occur in real pairs, $\pm\gamma$, imaginary pairs, $\pm j\omega$, or complex quartets, $\pm\alpha \pm j\omega$ [15]. Terms with negative, real eigenvalues decay to zero. Similarly, terms with positive, real eigenvalues grow exponentially. Modes with imaginary eigenvalues supply oscillatory behavior about the reference solution, and modes with complex eigenvalues demonstrate a combination of decay or growth with oscillations depending on the sign of the real component. Decaying modes are termed *stable*, exponentially increasing modes are *unstable*, and oscillatory modes are *nonstable*, or *neutrally stable*. The number of stable, unstable, and oscillatory (or, *center*) modes are denoted by n_S, n_U, and n_C, respectively. As the eigenvectors $\vec{\eta}_i$ associated with eigenvalues γ_i are linearly independent, they span $\mathbb{R}^n$, thus $n_U + n_S + n_C = \text{rank}(\mathbf{A})$. The space $\mathbb{R}^n$ is broken into three subspaces, the stable subspace, $E^S = \text{span}\left\{\vec{\eta}_i^S\right\}_{i=1}^{n_S}$, unstable subspace, $E^U = \text{span}\left\{\vec{\eta}_i^U\right\}_{i=1}^{n_U}$, and center subspace, $E^C = \text{span}\left\{\vec{\eta}_i^C\right\}_{i=1}^{n_C}$. These linear subspaces are invariant under $e^{\gamma_i t}$, so any solution $a_i\vec{\eta}_i$ in a subspace E remains within the span $\{\vec{\eta}_i\}$ for all past and future times [16].

Given the equilibrium points as the reference, $\vec{q}_* = \vec{q}_{L_i}$, if the linear dynamics relative to $\vec{q}_{L_i}$ possess no center subspace, i.e., $n_C = 0$, the equilibrium point is termed *hyperbolic*. In this case, the Stable Manifold Theorem stipulates that local stable and unstable manifolds, $W^S_{loc}(\vec{q}_{L_i})$, $W^U_{loc}(\vec{q}_{L_i})$, exist. These local manifolds possess global analogs, $W^S(\vec{q}_{L_i})$, $W^U(\vec{q}_{L_i})$, that are computed by propagating forward in time along the local unstable manifold or backward in time along the local stable manifold.

Theorem 3.1.1 (Stable Manifold Theorem) *Suppose* $\dot{\vec{q}} = \vec{f}(\vec{q})$ *possesses a hyperbolic equilibrium point* $\vec{q}_{L_i}$*. Then, there exist local stable and unstable manifolds* $W^S_{loc}(\vec{q}_{L_i})$, $W^U_{loc}(\vec{q}_{L_i})$ *of same dimension* n_S, n_U *as the eigenspaces* E^S *and* E^U *of the linearized system* (3.4)*, and tangent to* E^S *and* E^U *at* $\vec{q}_{L_i}$ *[16].*

These stable and unstable global manifolds supply information about transit behavior to and from the equilibrium solutions and are useful in trajectory design applications. In the more general case when $n_C \neq 0$, a center manifold also exists, as described by the Center Manifold Theorem:

Theorem 3.1.2 (Center Manifold Theorem) *Let* $\vec{f}$ *be a* C^r *vector field on* $\mathbb{R}^n$ *vanishing at the origin so that* $\vec{\eta}(\vec{q}_{L_i}) = \vec{0}$ *and let* $\mathbf{A} = D\vec{f}(\vec{q}_{L_i})$*. Divide the spectrum of* $\mathbf{A}$ *into its stable, unstable, and center parts,* n_S, n_U, *and* n_C *respectively, with*

$$Re(\gamma) \begin{cases} < 0 & : \gamma \in n_S \\ = 0 & : \gamma \in n_C \\ > 0 & : \gamma \in n_U \end{cases} .$$

Let the generalized eigenspaces be E^S, E^C, *and* E^U, *respectively. Then, there exist* C^r *stable and unstable manifolds* W^S *and* W^U *tangent to* E^S *and* E^U *at* $\vec{q}_{L_i}$ *and a center manifold* W^C *tangent to* E^C *at* $\vec{q}_{L_i}$*. The manifolds* W^S, W^U, *and* W^C *are all invariant for the flow* $\vec{f}$*. The stable and unstable manifolds are unique, but* W^C *need not be. If* $\vec{f}$ *is* C^∞*, then there exists a* C^r *center manifold for any* $r < \infty$ *[16].*

Accordingly, the notion of invariance extends to global manifolds: Any motion that originates on a global manifold remains on that manifold for all past and future times. Recall the solution derived for linear motion near the collinear libration points as represented in equation (3.19); this solution combines four modes: a stable mode, an unstable mode, and two oscillatory modes. An appropriate choice of initial conditions within the stable, unstable, or center subspaces isolates the desired behavior. The motion within these subspaces is easily transitioned from the linear approximations to the full nonlinear dynamical evolution via differential corrections processes, thus,

desirable motion in the nonlinear system, such as periodic solutions in the vicinity of the libration points, is obtained from the linear approximation.

Invariant Manifolds of a Periodic Orbit

Invariant manifolds are computed for periodic solutions in an analogous fashion as the invariant manifolds of the equilibrium points. To investigate the stability of periodic orbits and their associated manifolds, consider a discretization that reduces the dimension of the solution such that it is represented by a fixed point. The STM associated with one revolution of an orbit with period T, $\mathbf{\Phi}(\tau + T, \tau)$, termed the *monodromy matrix*, supplies such a dimension reduction. The monodromy matrix maps perturbations in the initial state to perturbations after one period of duration, T. By definition, a state on a periodic orbit repeats after time T, i.e., $\vec{q}(\tau) = \vec{q}(\tau+T)$, thus, the periodic solution is a fixed point on the stroboscopic map represented by the monodromy matrix. Accordingly, the linear approximation near a periodic orbit is represented by the discrete form

$$\delta\vec{q}(k+1) = \mathbf{\Phi}(\tau + T, \tau)\delta\vec{q}(k), \tag{3.33}$$

where $k = nT$, $k + 1 = (n + 1)T$, and $n \in \mathbb{Z}$ ($\mathbb{Z}$ is the set of all real integers). Assuming $\mathbf{\Phi}(\tau+T, \tau)$ has n linearly independent eigenvectors, i.e., it is not defective, the general solution to the discrete differential equation is given by

$$\delta\vec{q}(nT) = \mathbf{\Phi}(\tau + nT, \tau)\delta\vec{q}(\tau), \tag{3.34}$$

where, due to the STM property in equation (3.26), $\mathbf{\Phi}(\tau+nT, \tau) = \mathbf{\Phi}(\tau+T, \tau)^n$. Let λ_i be the eigenvalues of $\mathbf{\Phi}(\tau+T, \tau)$ and $\vec{v}_i$ be the associated eigenvectors. The general solution describing subsequent map iterations is then expressed via the superposition of the modes of $\mathbf{\Phi}$:

$$\delta\vec{q}(k) = \sum_{i=1}^{n} c_i\lambda_i\vec{v}_i. \tag{3.35}$$

Recall that the general solution of the continuous time linearization about the equilibrium points is governed by $e^{\gamma_i t}$. In this continuous time system, modes are dis-

tinguished by the sign of the associated eigenvector, i.e., eigenvalues with a negative real part produce stable motion, eigenvalues with a positive real part yield unstable motion, and eigenvalues with a zero real part induce oscillatory motion. In contrast, the modes of the discrete system are governed by λ_i^k. Thus, eigenvalues with magnitude less than one induce decaying, stable motion, eigenvalues with magnitudes greater than one yield unstable growth, and eigenvalues with unit magnitude produce motion that neither grows nor decays relative to the fixed point. Because the periodic orbit is completely described by the fixed point on the stroboscopic map, the stability of the fixed point, as determined by the eigenvalues of the monodromy matrix, is synonymous to the stability of the periodic orbit [17].

The eigenstructure of the monodromy matrix is described by Lyapunov's theorem.

Theorem 3.1.3 (Lyapunov's Theorem) *If λ is an eigenvalue of the monodromy matrix $\mathbf{\Phi}(\tau + T, \tau)$, of a time-invariant system, then λ^{-1} is also an eigenvalue. The spectrum of the monodromy matrix of a real time-invariant system is symmetric with respect to both the unit circle and the real axis[18].*

Accordingly, eigenvalues on the real axis occur in reciprocal pairs, i.e., λ and $1/\lambda$, and complex eigenvalues occur in conjugate pairs, λ and $\bar{\lambda}$. As in the continuous time system, the eigenvectors $\vec{v}_i$ span the space $\mathbb{R}^n$, again comprised of three subspaces, E^S, E^U, and E^C. The dimension of each subspace is equivalent to the number of stable, unstable, and center eigenvalues, respectively. Subsequently, $n_S = \dim\left[E^S\right]$ is the number of eigenvalues with magnitude less than one, $n_U = \dim\left[E^U\right]$ is the number of eigenvalues with magnitude greater than one, and $n_C = \dim\left[E^C\right]$ is the number of eigenvalues with unit magnitude. Note that, because eigenvalues occur in reciprocal pairs, $n_S = n_U$ and n_C is always a multiple of two. The monodromy matrix associated with a periodic orbit admits at least one unit eigenvalue, and, consequently, for the Hamiltonian CR3BP, the monodromy matrix associated with a periodic orbit possesses a pair of unit eigenvalues[19]. Accordingly, $n_C \geq 2$ for any CR3BP periodic solution.

A set of theorems exist for the discrete system that are analogous to the Stable Manifold Theorem and Center Manifold Theorem associated with the continuous time system [20, 21]. These theorems describe stable, unstable, and center invariant manifolds with dimensions n_S, n_U, and n_C, respectively, associated with the periodic solution that behave in the same manner as the invariant manifolds for the equilibrium point. In other words, the stable manifold asymptotically approaches the periodic orbit in forward time, the unstable manifold asymptotically approaches the periodic orbit in reverse time, and the center manifold remains bounded relative to the periodic solution. A *stable* periodic orbit in the CR3BP, thus, is characterized by $n_C = 6$, and therefore does not possess a stable or unstable manifold. In general, however, periodic orbits are *unstable* with at least one set of stable/unstable eigenvalues in addition to the minimum two center eigenvalues. Periodic orbits with an additional set of center eigenvalues, i.e., with $n_C = 4$ may exist as part of two periodic orbit families or may possess a center manifold that contains quasi-periodic structures. Similar to the invariant manifolds associated with the equilibrium points, the periodic orbit invariant manifolds yield a variety of additional solutions in the CR3BP offer have many trajectory design applications.

3.2 Differential Corrections

Insights gained from the STM are leveraged in differential corrections methods to identify motion that meets specific design constraints. Although there are numerous approaches to solve this type of problem, this investigation employs a multi-dimensional Newton-Raphson algorithm because of its simplicity and adaptability to many different scenarios [22].

3.2.1 Multi-Dimensional Newton Method

The simplicity and adaptability of the multi-dimensional Newton method stems from the formulation of the problem. Consider two vectors: a design-variable vector $\vec{X}$ of length w, and a constraint vector $\vec{F}$ of length u:

$$\vec{X} = \begin{Bmatrix} X_1 \\ \vdots \\ X_w \end{Bmatrix}, \qquad \vec{F}(\vec{X}) = \begin{Bmatrix} F_1 \\ \vdots \\ F_u \end{Bmatrix}.$$

Each element in $\vec{X}$ represents a node state, epoch time, time-of-flight, or similar variable that is adjusted to obtain a desired solution. Each row of $\vec{F}$ represents a constraint on the design variables and is equal to zero when satisfied. In general, constraints are formulated as functions of the design variables, thus $\vec{F} = \vec{F}(\vec{X})$. The goal of the Newton scheme is a set of design variables $\vec{X}_f$ that satisfies all constraints, i.e., $\vec{F}(\vec{X}_f) = \vec{0}$ [23]. A linear approximation is employed to relate changes in $\vec{X}$ to changes in $\vec{F}$. This predictive capability allows the corrections algorithm to identify and implement a step towards $\vec{X}_f$. Given an initial set of design variables $\vec{X}_*$, $\vec{F}(\vec{X})$ is expanded about $\vec{X}_*$ in a Taylor Series expansion:

$$\vec{F}(\vec{X}_f) = \vec{F}(\vec{X}_*) + \mathbf{J}\big|_{\vec{X}_*}(\vec{X}_f - \vec{X}_*) + \text{H.O.T.s}, \tag{3.36}$$

where $\mathbf{J}$ is the $u \times w$ Jacobian matrix with elements $\mathbf{J}_{i,j} = \dfrac{\partial F_i}{\partial X_j}$ evaluated on the reference solution $\vec{X}_*$. Ignoring higher order terms and recognizing that $\vec{F}(\vec{X}_f)$ evaluates to zero, the expansion is reduced to

$$\vec{F}(\vec{X}_*) + \vec{J}\big|_{\vec{X}_*}(\vec{X}_f - \vec{X}_*) = \vec{0}. \tag{3.37}$$

In practice, due to discrepancies between the linear prediction and the nonlinear path, a single iteration is insufficient to locate $\vec{X}_f$ and additional iterations are completed. This process is repeated until the L^2 norm of the constraint vector is less than some tolerance ϵ, i.e., $\left\|\vec{F}(\vec{X}_f)\right\| < \epsilon$. Substituting the more general $\vec{X}_n$ and $\vec{X}_{n+1}$ for $\vec{X}_*$ and

$\vec{X}$, respectively, in equation (3.37) and rearranging to solve for the updated design variable vector yields

$$\vec{X}_{n+1} = \vec{X} - \mathbf{J}^{-1}\Big|_{\vec{X}_n} \vec{F}(\vec{X}_n). \tag{3.38}$$

However, unless $u = w$, $\mathbf{J}$ is not square and, thus, is not invertible. In this case, an alternative solution is employed to obtain an expression for $\vec{X}_{n+1}$ in terms of $\vec{X}_n$, $\mathbf{J}$, and $\vec{F}(\vec{X}_n)$. Consider the general case with $u < w$; the simplified Taylor Series expansion in equation (3.37) is expressed as

$$\mathbf{J}\vec{x} = \vec{b}, \tag{3.39}$$

where $\vec{x}$ and $\vec{b}$ represent the design variable vector and constraint vector differentials $\left(\vec{X}_{n+1} - \vec{X}_n\right)$ and $\left(\vec{0} - \vec{F}(\vec{X}_n)\right)$, respectively. It is assumed that $\mathbf{J}$ is full rank, i.e., $\text{rank}(\mathbf{J}) = u$. Hence, for each $\vec{b}$, there exists a set of solutions comprised of a linear combination of a particular solution $\vec{x}_p$ and the homogenous solution $\vec{x}_h$:

$$\left\{ \vec{x} \;\middle|\; \mathbf{J}\vec{x} = \vec{b} \right\} = \left\{ \vec{x}_p + \vec{x}_h \;\middle|\; \mathbf{J}\vec{x}_p = \vec{b},\, \vec{x}_h \in \mathcal{N}(\mathbf{J}) \right\}. \tag{3.40}$$

To compute one particular solution, $\vec{x}_1$, multiply both sides of equation (3.39) by the right inverse of $\mathbf{J}$ and solve for $\vec{x}_1$:

$$\vec{x}_1 = \mathbf{J}^T(\mathbf{J}\mathbf{J}^T)^{-1}\vec{b}. \tag{3.41}$$

Suppose another particular solution $\vec{x}_2$ exists that satisfies equation (3.39). It follows that $\mathbf{J}\vec{x}_2 - \mathbf{J}\vec{x}_1 = \mathbf{J}(\vec{x}_2 - \vec{x}_1) = \vec{0}$. Expand the inner product of $(\vec{x}_2 - \vec{x}_1)$ and $\vec{x}_1$ to gain insight into the relationship between the solutions:

$$\begin{aligned}
(\vec{x}_2 - \vec{x}_1)^T\vec{x}_1 &= (\vec{x}_2 - \vec{x}_1)^T\mathbf{J}^T(\mathbf{J}\mathbf{J}^T)^{-1}\vec{b} \\
&= (\mathbf{J}(\vec{x}_2 - \vec{x}_1))^T(\mathbf{J}\mathbf{J}^T)^{-1}\vec{b} \\
&= 0.
\end{aligned}$$

Note that $\vec{x}_1$ is replaced by the solution obtained in equation (3.41). Since the inner product between the difference vector $(\vec{x}_2 - \vec{x}_1)$ and the solution $\vec{x}_1$ is zero, the

two vectors are orthogonal. Applying the Pythagorean theorem to this right vector triangle offers insight into the relative lengths of the vectors:

$$\|\vec{x}_2 - \vec{x}_1\|^2 + \|\vec{x}_1\|^2 = \|\vec{x}_2\|^2 . \tag{3.42}$$

The left side of equation (3.42) is clearly greater than the magnitude of $\vec{x}_1$, so the magnitude of $\vec{x}_2$ is greater than the magnitude of $\vec{x}_1$. Because $\vec{x}_2$ is *any* other vector that satisfies equation (3.39), it follows that $\vec{x}_1$ is the solution with the smallest magnitude, i.e., the *minimum-norm* solution. Recall that $\vec{x}$ represents the vector differential $\vec{X}_{n+1} - \vec{X}_n$. Accordingly, the magnitude of $\vec{x}$ indicates the distance between two iterations of the design variable vector and the minimum-norm solution represents a solution that is nearest the previous solution in w-dimensional space. Applying the minimum-norm solution from equation (3.41) to equation (3.37) yields an update equation for non-square Jacobian matrices:

$$\vec{X}_{n+1} = \vec{X} - \mathbf{J}^T(\mathbf{J}\mathbf{J}^T)^{-1}\vec{F}(\vec{X}). \tag{3.43}$$

This solution is implemented in place of equation (3.38) in the general case when the Jacobian matrix is not square.

3.2.2 Single Shooting Method

To illustrate the multi-dimensional Newton algorithm, consider a simple example with the initial state vector for a spacecraft defined as $\vec{q}_0 = \{x_0,\, y_0,\, z_0,\, \dot{x}_0,\, \dot{y}_0,\, \dot{z}_0\}^T$. If no adjustments are incorporated, the spacecraft arrives at some final state $\vec{q}_f = \{x_f,\, y_f,\, z_f,\, \dot{x}_f,\, \dot{y}_f,\, \dot{z}_f\}^T$ at time $t = t_0 + \tau$. Suppose a different final position $\vec{r}_d = \{x_d,\, y_d,\, z_d\}^T$ is desired. To achieve this goal, the initial velocity and time-of-flight along the arc are adjusted to yield a different path. Thus, the design variable vector is comprised of the initial velocity and time-of-flight variables:

$$\vec{X} = \left\{ \dot{x}_0 \quad \dot{y}_0 \quad \dot{z}_0 \quad \tau \right\}^T . \tag{3.44}$$

Because the initial position $(x_0,\ y_0,\ z_0)$ is not present in the design variable vector, it remains fixed and is not adjusted by the corrections process. A single vector constraint

(or three scalar constraints) is placed on the final position of the spacecraft to ensure it arrives at the desired location:

$$\vec{F}(\vec{X}) = \begin{Bmatrix} x_f - x_d & y_f - y_d & z_f - z_d \end{Bmatrix}^T. \tag{3.45}$$

The Jacobian matrix relating the constraint equations and design variable vectors is represented by the following expression:

$$\mathbf{J} = \frac{\partial \vec{F}(\vec{X})}{\partial \vec{X}} = \begin{bmatrix} \frac{\partial(x_f - x_d)}{\partial \dot{x}_0} & \frac{\partial(x_f - x_d)}{\partial \dot{y}_0} & \frac{\partial(x_f - x_d)}{\partial \dot{z}_0} & \frac{\partial(x_f - x_d)}{\partial \tau} \\ \frac{\partial(y_f - y_d)}{\partial \dot{x}_0} & \frac{\partial(y_f - y_d)}{\partial \dot{y}_0} & \frac{\partial(y_f - y_d)}{\partial \dot{z}_0} & \frac{\partial(y_f - y_d)}{\partial \tau} \\ \frac{\partial(z_f - z_d)}{\partial \dot{x}_0} & \frac{\partial(z_f - z_d)}{\partial \dot{y}_0} & \frac{\partial(z_f - z_d)}{\partial \dot{z}_0} & \frac{\partial(z_f - z_d)}{\partial \tau} \end{bmatrix}. \tag{3.46}$$

Because the desired final position (x_d, y_d, z_d) is selected independently of the node $\vec{q}_0$ and is constant, each partial of a desired final position state with respect to any of the design variables is zero. Thus, the Jacobian simplifies to

$$\mathbf{J} = \begin{bmatrix} \frac{\partial x_f}{\partial \dot{x}_0} & \frac{\partial x_f}{\partial \dot{y}_0} & \frac{\partial x_f}{\partial \dot{z}_0} & \frac{\partial x_f}{\partial \tau} \\ \frac{\partial y_f}{\partial \dot{x}_0} & \frac{\partial y_f}{\partial \dot{y}_0} & \frac{\partial y_f}{\partial \dot{z}_0} & \frac{\partial y_f}{\partial \tau} \\ \frac{\partial z_f}{\partial \dot{x}_0} & \frac{\partial z_f}{\partial \dot{y}_0} & \frac{\partial z_f}{\partial \dot{z}_0} & \frac{\partial z_f}{\partial \tau} \end{bmatrix} = \begin{bmatrix} & & & \dot{x}_f \\ & \mathbf{\Phi}_{rv}(t_0 + \tau, t_0) & & \dot{y}_f \\ & & & \dot{z}_f \end{bmatrix}. \tag{3.47}$$

The left-most 3×3 block of $\mathbf{J}$ represents the partial derivatives of the integrated position state with respect to the original velocity state; these relationships are captured by the STM, thus, the 3×3 block is replaced with the appropriate STM elements for the propagated arc. The final column represents the time derivative of the integrated position states, which are equivalent to the integrated velocity states. As there exist more design variables than constraints, the Jacobian is not square and the minimum-norm solution is leveraged to obtain an updated design variable vector:

$$\begin{Bmatrix} \dot{x}_0 \\ \dot{y}_0 \\ \dot{z}_0 \\ \tau \end{Bmatrix}_{n+1} = \begin{Bmatrix} \dot{x}_0 \\ \dot{y}_0 \\ \dot{z}_0 \\ \tau \end{Bmatrix}_n - \mathbf{J}^T(\mathbf{J}\mathbf{J}^T)^{-1} \begin{Bmatrix} x_f - x_d \\ y_f - y_d \\ z_f - z_d \end{Bmatrix}_n. \tag{3.48}$$

By iteratively applying this update equation, a solution $\vec{X}$ is obtained that satisfies the constraint functions such that $\left\|\vec{F}(\vec{X})\right\| < \epsilon$.

3.2.3 Multiple Shooting Method

The multiple shooting strategy is a more general and a more powerful extension of the single shooting algorithm that adjusts multiple arc segments simultaneously [22, 24]. Consider, for example, the arc segments displayed in Figure 3.1. Each segment may represent part of a transfer arc, periodic orbit, or any other path in the CR3BP or the BC4BP model. An end-to-end design consists of n nodes with $n-1$ propagated arc segments between them. The ith segment originates at node state $\vec{q}_i$ and epoch time T_i. Each arc segment is propagated from the initial node state for some time-of-flight τ_i to a final state $\vec{q}_{i,f}$. The final nth node is not propagated and serves only as an end point that may be constrained to attain a desired final state.

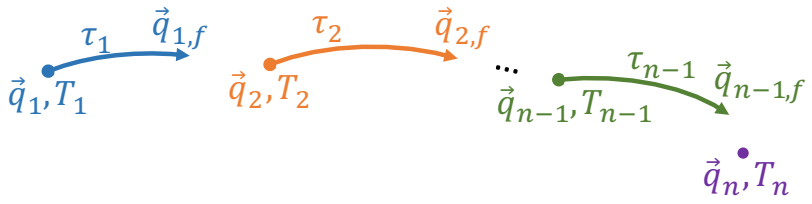

Figure 3.1.: Arc Segments Before Corrections

The state and constraint vectors may be constructed in a variety of ways. In this investigation, the design variable vector possesses a structure consistent with

$$\vec{X} = \left\{ \vec{q}_1 \quad \dots \quad \vec{q}_n \quad \tau_1 \quad \dots \quad \tau_{n-1} \quad T_1 \quad \dots \quad T_n \right\}^T, \tag{3.49}$$

where the node states are listed first, followed by times-of-flight and epoch times. Additional design variables are appended to the end of $\vec{X}$ as required. Note that epoch times T_i are only included for the nonautonomous BC4BP. An end-to-end trajectory is constructed from the nodes, times-of-flight, and epoch times as in Figure 3.1. These

quantities are subject to a number of constraints. For example, any spatial path must be continuous in both position and time. Let node state $\vec{q}_i$ contain position and velocity states such that $\vec{q}_i = \{\vec{r}_i \;\; \vec{v}_i\}^T$. Position continuity is enforced by requiring the ith node position to coincide with the final propagated state from the previous node, i.e., $\vec{r}_{i-1,f} - \vec{r}_i = \vec{0}$. Similarly, a time continuity constraint takes the form $T_{i+1} - (T_i + \tau_i) = 0$. In general, velocity continuity is also required between arc segments, but is not enforced wherever an impulsive maneuver is allowed. Velocity continuity constraints are formulated in the same fashion as position continuity constraints. In this investigation, the constraint vector is constructed in the form

$$\vec{F}(\vec{X}) = \left\{ \begin{array}{c} \vec{q}_{1,f} - \vec{q}_2 \\ \vdots \\ \vec{q}_{n-1,f} - \vec{q}_n \\ T_2 - (T_1 + \tau_1) \\ \vdots \\ T_n - (T_{n-1} + \tau_{n-1}) \end{array} \right\}, \tag{3.50}$$

where both position and velocity continuity are represented by the $\vec{q}_{i-1,f} - \vec{q}_i$ constraints. Again, note that time continuity is only required for the nonautonomous BC4BP. Many other constraint options exist and are formulated intuitively in the multiple shooting problem. As demonstrated in the single shooting example, any of the design variables may be constrained to be equal to a constant value. Accordingly, individual node positions, velocities, and epochs can be fixed as desired. More creative constraints may be applied to ensure a node is an apse relative to a specific primary, or to ensure a node remains at a fixed distance from a point. Additionally, the total maneuver budget, or total ΔV, along a transfer path can be constrained.

Inequality Constraints

All constraints have been formulated, thus far, as equality constraints. The Newton method is a root-finding process and, accordingly, identifies design vectors $\vec{X}$ that

drive the constraint function to zero, within some specified tolerance. However, it is often useful to constrain an inequality, such as a minimum altitude relative to a primary, or a maximum allowable ΔV [25]. Such inequality constraints are achieved by incorporating a slack variable. Consider, for example, a minimum altitude constraint:

$$G = r > r_{min}. \tag{3.51}$$

An arbitrary positive slack variable β^2 is added to the left side to yield an equality constraint:

$$G = r = r_{min} + \beta^2. \tag{3.52}$$

A quick rearrangement of terms yields a constraint formatted properly for the Newton method:

$$F = r - r_{min} - \beta^2 = 0. \tag{3.53}$$

The slack variable is appended to the design vector $\vec{X}$ and is adjusted with the other variables to satisfy the constraint function. It is good practice to define an initial value for β such that F is satisfied when G satisfied. In other words, if the initial design satisfies $r > r_{min}$, choose $\beta = \sqrt{r - r_{min}}$ to ensure that $F = 0$.

3.2.4 Jacobi Matrix Formulation

Although the relationships between constraints and design variables are available numerically (e.g., via finite differencing or complex-step derivatives), analytical relationships offer higher accuracy and require less computational time to evaluate. The single shooting example developed in Section 3.2.2 briefly discusses the relationships between a position state constraint and a node state; the relationship between this constraint and the arc time-of-flight is also considered. These relationships, mathematically represented as partial derivatives, are examined in more detail in this section as they apply to a multiple shooting process. In particular, the partial derivatives of state-continuity constraints are derived for both a CR3BP multiple shooting process as well as for a BC4BP shooting scheme. Many other constraints leverage the

propagated states $\vec{q}_{i,f}$ and employ derivatives similar to those derived for the state continuity constraint; these other constraints are not formulated here.

State Continuity

State continuity constraints are included in most corrections processes. Position continuity is required between all arc segments in a discretized trajectory, and velocity continuity is desirable as it is typically infeasible to implement impulsive maneuvers between every arc segment. Consider the full state continuity constraint $\vec{F} = \vec{q}_{i-1,f} - \vec{q}_i$. The relationships between this constraint and the full design vector $\vec{X}$ are captured by the vector partial derivative $\frac{\partial \vec{F}}{\partial \vec{X}}$, a $6 \times w$ matrix where w is the number of design variables in $\vec{X}$. To evaluate this derivative, apply the process described by Pavlak to express the constraint vector as a function of its explicit and implicit variables [25]:

$$\vec{F} = \vec{f}\left(\vec{q}_i, \;\; \vec{q}_{i-1,f}(\vec{q}_{i-1}, \; \tau_{i-1}, \; T_{i-1})\right). \tag{3.54}$$

First, consider the relationship between $\vec{F}$ and $\vec{q}_i$. Because $\vec{q}_i$ appears explicitly in the constraint equation, this derivative is straightforward:

$$\frac{\partial \vec{F}}{\partial \vec{q}_i} = -\mathbf{I}_{6\times 6}. \tag{3.55}$$

Next, consider the relationship between $\vec{F}$ and $\vec{q}_{i-1}$, which does not appear explicitly in $\vec{F}$. Instead, apply the partial derivative chain rule to extract the relationship:

$$\frac{\partial \vec{F}}{\partial \vec{q}_{i-1}} = \frac{\partial \vec{F}}{\partial \vec{q}_{i-1,f}} \frac{\mathrm{d}\vec{q}_{i-1,f}}{\mathrm{d}\vec{q}_{i-1}}. \tag{3.56}$$

The first term on the right side of the expression is simply the 6×6 identity matrix. The second term relates changes in the propagated state $\vec{q}_{i-1,f}$ to changes in its originating state $\vec{q}_{i-1}$. These relationships are captured by the STM integrated along with the EOMs. Substituting the STM into the partial derivative expansion yields

$$\frac{\partial \vec{F}}{\partial \vec{q}_{i-1}} = \mathbf{I}_{6\times 6}\mathbf{\Phi}(T_{i-1} + \tau_{i-1}, \; T_{i-1}) = \mathbf{\Phi}(T_{i-1} + \tau_{i-1}, \; T_{i-1}). \tag{3.57}$$

No relationships exist between $\vec{F}$ and node state $\vec{q}_j$ for $j \neq i,\ i-1$. Each node state is selected independently of the other nodes, thus $\vec{q}_{i-2}$, $\vec{q}_{i-3}$, etc., have no effect on $\vec{q}_{i-1}$ or $\vec{q}_i$. In fact, no functional relationship exists between $\vec{q}_{i-1}$ and $\vec{q}_i$; the desired continuity conditions between these states are captured by the constraint equation $\vec{F}$, not by any functional dependency on one another.

Next consider the relationship between $\vec{F}$ and time-of-flight τ_{i-1}. This relationship is also computed by expanding the partial derivative via the chain rule:

$$\frac{\partial \vec{F}}{\partial \tau_{i-1}} = \frac{\partial \vec{F}}{\partial \vec{q}_{i-1,f}} \frac{\mathrm{d}\vec{q}_{i-1,f}}{\mathrm{d}\tau_{i-1}} = \mathbf{I}_{6\times 6}\dot{\vec{q}}_{i-1,f} = \dot{\vec{q}}_{i-1,f}. \tag{3.58}$$

The first term again simplifies to the identity matrix. The second term represents the derivative of the state with respect to integration time, which simply evaluates to the state time-derivative, which consists of the velocity and acceleration at the final propagated state. Like node states, arc segment times-of-flight are chosen independently of one another, so $\frac{\partial \vec{F}}{\partial \tau_j} = \vec{0}$ for $j \neq i-1$. Accordingly, the state continuity constraint depends only the $i-1$th time of flight.

Finally, consider the relationship between $\vec{F}$ and epoch time T_{i-1}. In the autonomous CR3BP, no such relationship exists but, in the BC4BP, the epoch plays an important role in the dynamical evolution. The familiar derivative expansion yields

$$\frac{\partial \vec{F}}{\partial T_{i-1}} = \mathbf{I}_{6\times 6} \frac{\mathrm{d}\vec{q}_{i-1,f}}{\mathrm{d}T_{i-1}}\,. \tag{3.59}$$

The resulting expression relates the propagated state to its originating epoch; this relationship is not as straightforward as those considered thus far. Rather than attempting to identify an analytical expression for this relationship, consider its derivative:

$$\frac{\mathrm{d}}{\mathrm{d}t}\left(\frac{\partial \vec{q}}{\partial T}\right) = \frac{\partial}{\partial T}\left(\frac{\mathrm{d}\vec{q}}{\mathrm{d}t}\right), \tag{3.60}$$

where t represents time along the propagated arc segment and ranges from T to $T+\tau$, inclusive. When integrated with the equations of motion, this derivative yields a value for the quantity $\frac{\partial \vec{q}}{\partial T}$. Because t and T are independent (recall that T is an

independently chosen value for each node), the denominators of the derivatives are interchangeable. Expanding this relationship yields

$$\frac{\partial}{\partial T}\left(\frac{\mathrm{d}\vec{q}}{\mathrm{d}t}\right) = \frac{\partial}{\partial T}\left(\dot{\vec{q}}\right) = \frac{\partial}{\partial T}\left[\vec{f}\left(t,\, \vec{q},\, \left\{\vec{r}_k(T,t),\ k=1,2,3\right\}\right)\right], \tag{3.61}$$

where $\vec{f}$ represents the equations of motion, which are functions of integration time t, initial state $\vec{q}$, and the position of each primary $\vec{r}_k$. Note that the positions of the primaries are functions only of epoch time T and integration time t. The partial of $\vec{f}$ with respect to epoch time T is expanded via the chain rule:

$$\frac{\partial \vec{f}}{\partial T} = \frac{\partial \vec{f}}{\partial t}\frac{\mathrm{d}t}{\mathrm{d}T} + \frac{\partial \vec{f}}{\partial \vec{q}}\frac{\partial \vec{q}}{\partial T} + \sum_{k=1}^{3}\left[\frac{\partial \vec{f}}{\partial \vec{r}_k}\frac{\mathrm{d}\vec{r}_k}{\mathrm{d}T}\right]. \tag{3.62}$$

As already established, t and T are independent, thus $\frac{\mathrm{d}t}{\mathrm{d}T}$ is zero. The quantity $\frac{\partial \vec{f}}{\partial \vec{q}}$ is represented by the **A** matrix, as derived in equation (3.4). The derivative of primary position with respect to epoch time is simply the velocity of the primary, i.e.,

$$\frac{\mathrm{d}\vec{r}_k}{\mathrm{d}T} = \vec{v}_k. \tag{3.63}$$

Analytical expressions for these velocities appear in equations (2.67) - (2.69). The final term to evaluate is the relationship between the EOMs, $\vec{f}$, and the primary position, $\vec{r}_k$, captured in $\frac{\partial \vec{f}}{\partial \vec{r}_k}$. Recall that

$$\vec{f} = \dot{\vec{q}} = \left\{\dot{x} \quad \dot{y} \quad \dot{z} \quad \ddot{x} \quad \ddot{y} \quad \ddot{z}\right\}^T,$$

where the second derivatives are evaluated by equations (2.62) - (2.64). Thus, the 6×3 matrix $\frac{\partial \vec{f}}{\partial \vec{r}_k}$ that results is

$$\frac{\partial \dot{\vec{q}}}{\partial \vec{r}_k} = \begin{bmatrix} \dfrac{\partial \dot{x}}{\partial x_k} & \dfrac{\partial \dot{x}}{\partial y_k} & \dfrac{\partial \dot{x}}{\partial z_k} \\ \vdots & & \vdots \\ \dfrac{\partial \ddot{z}}{\partial x_k} & \cdots & \dfrac{\partial \ddot{z}}{\partial z_k} \end{bmatrix} = \begin{bmatrix} 0 & 0 & 0 \\ 0 & 0 & 0 \\ 0 & 0 & 0 \\ \dfrac{\partial \ddot{x}}{\partial x_k} & \dfrac{\partial \ddot{x}}{\partial y_k} & \dfrac{\partial \ddot{x}}{\partial z_k} \\ \dfrac{\partial \ddot{y}}{\partial x_k} & \dfrac{\partial \ddot{y}}{\partial y_k} & \dfrac{\partial \ddot{y}}{\partial z_k} \\ \dfrac{\partial \ddot{z}}{\partial x_k} & \dfrac{\partial \ddot{z}}{\partial y_k} & \dfrac{\partial \ddot{z}}{\partial z_k} \end{bmatrix}. \tag{3.64}$$

Note that because the velocity states ($\dot{x}$, $\dot{y}$, $\dot{z}$) are not functions of primary position, these components evaluate to zero, leaving only the bottom half of the matrix as nonzero. The remaining partial derivatives are summarized in Appendix B.3. By substituting these relationships into equation (3.62) and applying the relationship from equation (3.60), an analytical differential equation is available:

$$\frac{\mathrm{d}}{\mathrm{d}t}\left(\frac{\partial \vec{q}}{\partial T}\right) = \mathbf{A}(t)\,\frac{\partial \vec{q}}{\partial T} + \sum_{k=1}^{3}\left[\frac{\partial \vec{f}}{\partial \vec{r}_k}\,\frac{\mathrm{d}\vec{r}_k}{\mathrm{d}T}\right]. \tag{3.65}$$

This equation is integrated simultaneously with the EOMs and the STM differential equation to render a time-history for the quantity $\frac{\mathrm{d}\vec{q}}{\mathrm{d}T}$. The initial condition for $\frac{\partial \vec{q}}{\partial T}$ represents the change in a node state $\vec{q}$ due to a change in the node epoch T. Because these two quantities are independent of one another, the initial condition is $\vec{0}_{6\times 1}$. The original constraint equation (3.59) is computed via the final integrated value of $\frac{\partial \vec{q}}{\partial T}$ on the $(i-1)$th arc segment. As usual, $\frac{\partial \vec{F}}{\partial T_j} = \vec{0}$ for $j \neq i-1$.

The Jacobian matrix $\mathbf{J}$ is constructed by placing all partial derivative terms in their appropriate locations. As the matrix is defined as $\mathbf{J} = \dfrac{\partial \vec{F}(\vec{X})}{\partial \vec{X}}$, the ith row of $\mathbf{J}$ corresponds to the derivatives of the constraint F_i with respect to all state variables. Similarly, the jth column of $\mathbf{J}$ represents the derivative of all the constraints $\vec{F}$ with respect to the state X_j. Consider the Jacobian matrix associated with a set of n nodes, all of which are constrained to be continuous in position and velocity. The Jacobian is then represented as three submatrices:

$$\mathbf{J} = \begin{bmatrix} \mathbf{J_1} & \mathbf{J_2} & \mathbf{J_3} \end{bmatrix}, \tag{3.66}$$

where $\mathbf{J_1}$ represents the partial derivatives of the continuity constraints with respect to the node states, $\mathbf{J_2}$ represents the derivatives with respect to times-of-flight, and $\mathbf{J_3}$

represents the derivatives with respect to epoch times. Accordingly, each submatrix is expressed as:

$$\mathbf{J_1} = \begin{bmatrix} \mathbf{\Phi}_1 & -\mathbf{I}_{6\times6} & 0_{6\times6} & \dots & 0_{6\times6} \\ 0_{6\times6} & \mathbf{\Phi}_2 & -\mathbf{I}_{6\times6} & & \vdots \\ \vdots & & \ddots & \ddots & 0_{6\times6} \\ 0_{6\times6} & \dots & 0_{6\times6} & \mathbf{\Phi}_{n-1} & -\mathbf{I}_{6\times6} \end{bmatrix}, \qquad \mathbf{J_2} = \begin{bmatrix} \dot{\vec{q}}_{1,f} & 0_{1\times6} & \dots & 0_{1\times6} \\ 0_{6\times1} & \dot{\vec{q}}_{2,f} & & \vdots \\ \vdots & & \ddots & 0_{6\times1} \\ 0_{6\times1} & \dots & 0_{6\times1} & \dot{\vec{q}}_{n-1,f} \end{bmatrix},$$

$$\mathbf{J_3} = \begin{bmatrix} \dfrac{\partial \vec{q}_{1,f}}{\partial T_1} & 0_{6\times1} & \dots & \dots & 0_{6\times1} \\ 0_{6\times1} & \dfrac{\partial \vec{q}_{2,f}}{\partial T_2} & & & \vdots \\ \vdots & & \ddots & & \vdots \\ 0_{6\times1} & \dots & 0_{6\times1} & \dfrac{\partial \vec{q}_{n,f}}{\partial T_{n-1}} & 0_{6\times1} \end{bmatrix}.$$

Additional constraints correspond to additional rows in the Jacobian matrix.

Time Continuity

Although the autonomous CR3BP does not require time continuity constraints, multiple shooting problem formulations in the BC4BP must enforce time continuity. Time continuity constraints are represented by a simple difference:

$$F = T_i - (T_{i-1} + \tau_{i-1}) = 0. \tag{3.67}$$

The partial derivatives of this constraint are straightforward and equal to ±1. Recall that epoch times and times-of-flight are all independently selected design variables with no functional dependencies on any other design variables. A set of $n-1$ time continuity constraints are appended to the constraint vector, and an $n-1\times w$ matrix is appended to the Jacobian,

$$\mathbf{J} = \begin{bmatrix} \mathbf{J_1} & \mathbf{J_2} & \mathbf{J_3} \\ \mathbf{0} & -\mathbf{I}_{n-1\times n-1} & \mathbf{J_5} \end{bmatrix}, \tag{3.68}$$

where the negative identity matrix represents the partial derivatives of the time continuity constraints with respect to the times-of-flight. The submatrix $\mathbf{J_5}$ captures the partial derivatives with respect to the node epoch times and appears as a banded matrix:

$$\mathbf{J_5} = \begin{bmatrix} -1 & 1 & 0 & \dots & 0 \\ 0 & -1 & 1 & & \vdots \\ \vdots & & \ddots & \ddots & 0 \\ 0 & \dots & 0 & -1 & 1 \end{bmatrix}.$$

The relationships represented by these matrices supply the corrections scheme with the information necessary to adjust the epochs and times-of-flight of a solution to satisfy the requirements imposed by the constraint vector.

3.3 Applications for a Multiple Shooting Strategy

The general approach of these shooting schemes offer many applications due to the intuitive form of the solution formulation. When combined with knowledge of system dynamics, the shooting method becomes a powerful tool to isolate desired behavior such as periodic and quasi-periodic motion. To demonstrate this capability, this shooting strategy is employed to compute several types of periodic orbits in the CR3BP, including planar resonant orbits and libration point orbits.

3.3.1 Planar Resonant Orbits

Resonant orbits are periodic solutions with orbital periods in rational ratios as compared to the period of the system in which they reside. For example, a 5:2 resonant orbit in the Earth-Moon system completes five revolutions around the Earth in the same interval that the Moon requires to complete two revolutions. These pure, rational period ratios exist only in the two-body problem, however. Subsequently, when the gravitational perturbation of the secondary (e.g., the Moon in the Earth-Moon system) is included, resonant orbits are adjusted to maintain periodicity and

the ratio between their period and the system becomes irrational, though it remains near the two-body rational ratio.

Two-Body Resonant Orbits

To compute a resonant orbit, the analysis begins with motion in the two-body problem (2BP) about the primary body [26]. Let a resonant orbit be characterized by an orbital period in a p:q ratio with the period of the secondary body, i.e., the resonant orbit completes p revolutions in an *inertial* frame over the same interval that the secondary requires to complete p revolutions. The orbital period of the spacecraft is, thus, easily computed:

$$\mathbb{P}_s = \mathbb{P}_2 * \frac{q}{p}. \tag{3.69}$$

The semi-major axis of the resonant orbit is determined next:

$$a_s = \left(\frac{n_s^2}{G m_1} \right)^{-1/3}, \tag{3.70}$$

where the mean motion n_s of the spacecraft orbit is defined as $n_s = 2\pi/\mathbb{P}_s$, m_1 is the mass of the central body, P_1, in dimensional units, and G is the universal gravitational constant. Orbital period and semi-major axis are the only parameters constrained by the definition of the resonant orbit. However, constraints on the shape of the orbit may be derived from limits placed on the periapsis and apoapsis radii. Consider a constraint on periapsis to ensure crashes with the central body are avoided:

$$r_p > r_{p,min} \quad \rightarrow \quad a(1-e) - r_{p,min} > 0 \quad \rightarrow \quad e < 1 - \frac{r_{p,min}}{a}, \tag{3.71}$$

where $r_{p,min}$ is the minimum periapse radius. At the limiting case, $r_{p,min} = 0$ and the equation simplifies to $e < 1$, which simply ensures the resonant orbit is elliptical and not parabolic nor hyperbolic with respect to the central body. Thus the minimum periapsis radius places a bound on the maximum value of the orbital eccentricity e.

In general, the initial state of the resonant orbit is defined in the form $\vec{q}_0 = \{x \quad y \quad z \quad \dot{z} \quad \dot{y} \quad \dot{z}\}^T$. A planar orbit requires $z = \dot{z} = 0$. At this initial time, let

the spacecraft lie on the P_1-P_2 line and let that line coincide with the inertial $\hat{\mathbb{X}}$-axis. Hence, the initial y-coordinate is zero. Additionally, let the initial state occur at an apse, which simplifies the initial state by constraining it to be perpendicular to the P_1-spacecraft line, i.e., $\dot{x} = 0$. Thus, the initial state on the resonant orbit in an inertial frame is $\vec{q}_0 = \{x \;\; 0 \;\; 0 \;\; 0 \;\; \dot{y} \;\; 0\}^T$ where x specifies the initial radius. Given a choice of e, x is computed as either apoapsis radius $x = r_a = a(1+e)$ or periapsis radius $x = r_p = a(1-e)$. Velocity is then expressed by

$$\dot{y} = \sqrt{Gm_1 \left(\frac{2}{x} - \frac{1}{a} \right)}. \tag{3.72}$$

Once the initial state is selected, the resonant orbit is easily computed in the 2BP. Solutions with $p \geq q$ are termed *interior* orbits as their period is less than that of P_2 and they traverse the interior of the P_1-P_2 system. Conversely, solutions with $p < q$ possess orbital periods greater than that of P_2 and remain primarily outside the P_1-P_2 system. A 5:2 interior resonant orbit is plotted in Figure 3.2 in both inertial and rotating views. The inertial view (Figure 3.2(a)) clearly depicts the interior nature of the resonant orbit. For comparison, consider the 3:5 exterior resonant orbit represented in Figure 3.3. The inertial view, in Figure 3.3(a), demonstrates that the larger orbit remains primarily exterior to the system.

Note that the rotating views of the resonant orbits have significantly different geometry in comparison to the inertial views. Although the inertial path repeats p times during q revolutions of P_2, the same orbit in a rotating view completes only one full revolution and does not repeat during the q revolutions of the secondary, P_2. Accordingly, the period of the resonant orbit is generally identified as $\mathbb{P} = p\frac{2\pi}{n}$ where n is the mean motion computed for the elliptical resonant orbit depicted in the inertial view.

Three-Body Resonant Orbits

In the two-body problem, resonant orbits are defined by periods in rational ratios as compared to the period of the system. However, when a third body is included,

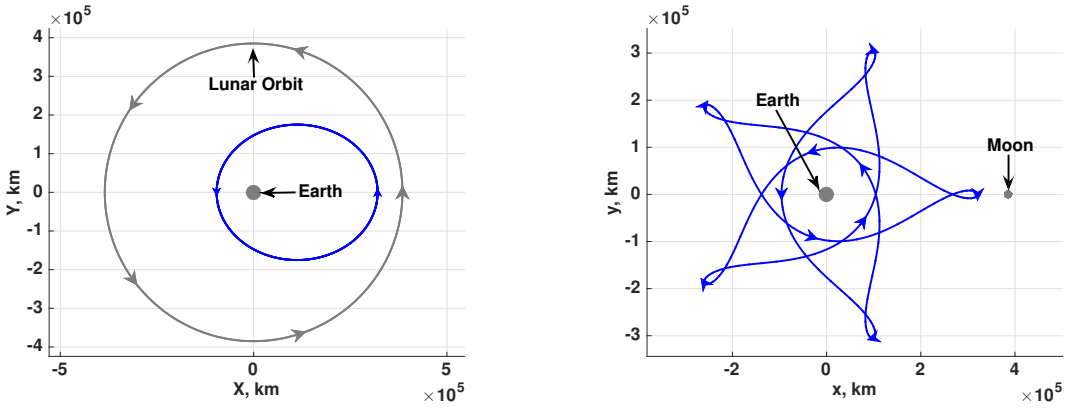

(a) Inertial View (b) Earth-Moon Rotating View

Figure 3.2.: A 5:2 Interior Resonant Orbit in the Earth-Moon 2BP.

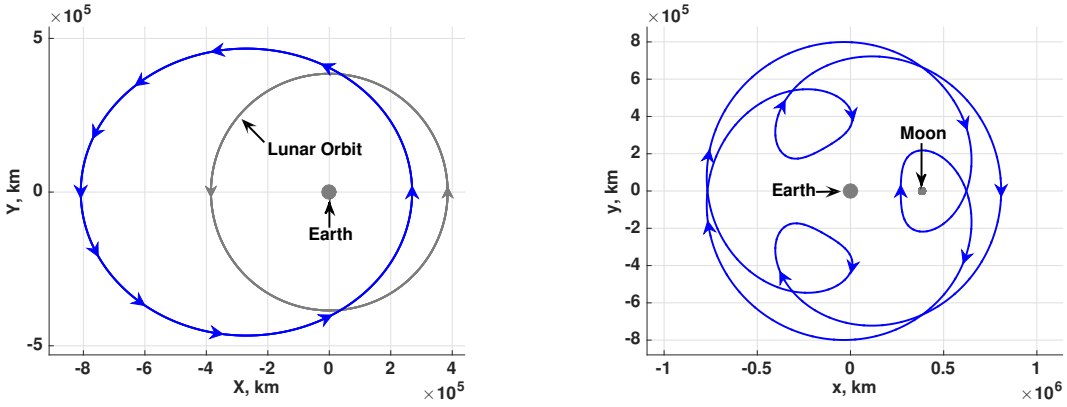

(a) Inertial View (b) Earth-Moon Rotating View

Figure 3.3.: A 3:5 Exterior Resonant Orbit in the Earth-Moon 2BP.

this motion is perturbed from its periodic nature. Although a corrections process is easily applied to adjust the orbit to preserve periodicity, the ratio of periods between the resonant orbit and primary-secondary system no longer exists as a rational ratio, but as an *approximate* rational ratio. The two-body solution is transitioned to the three-body problem by nondimensionalizing the rotating representation of the orbit. Because the solution must be adjusted to reproduce a periodic path, a shooting pro-

cedure is employed. Most resonant orbit paths possess complex geometry as viewed in the rotating frame and benefit from the robustness supplied by a multiple shooting strategy. The two-body problem is considered a special case of the CR3BP with $\mu = 0$. To recreate the resonant orbit in a higher mass ratio system (e.g., Earth-Moon with $\mu \approx 0.012$), the solution is gradually transitioned from $\mu = 0$ to the desired μ value. Natural parameter continuation, discussed more extensively in Section 3.4.1, supplies the framework required for this transition. A comparison between the two-body and three-body motion for the 5:2 and 3:5 Earth-Moon resonant orbits appears in Figure 3.4. These three-body resonant orbits are computed such that their periods are as similar as possible to the two-body resonant orbit periods, but the three-body orbits occur in families, thus, additional options exist. The two-body geometry is approximately retained in this example, but the addition of the gravity of the second body clearly introduces some changes.

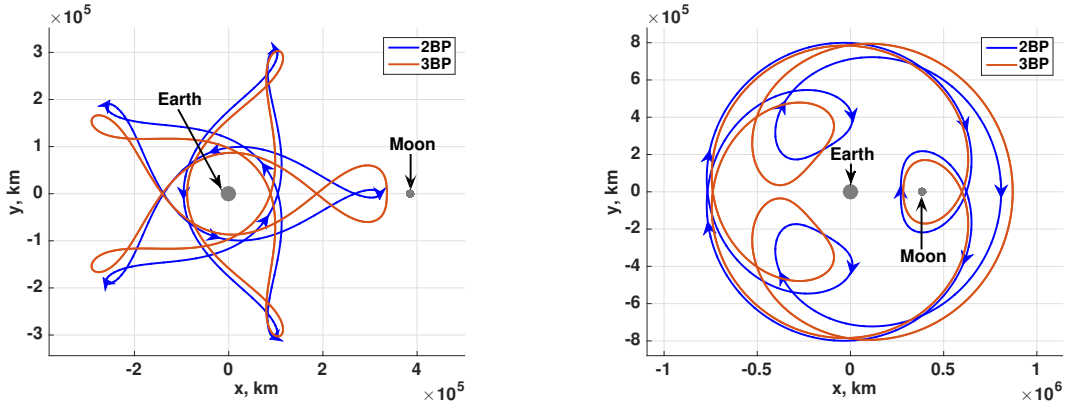

(a) 5:2 Earth-Moon Resonant Orbit

(b) 3:5 Earth-Moon Resonant Orbit

Figure 3.4.: Two representative resonant orbits in the two-body (blue) and three-body (red) problems, plotted in Earth-Moon rotating frame

3.3.2 Periodic Orbits

While some three-body periodic solutions, e.g., resonant orbits, are initialized from two-body Keplarian motion, additional periodic orbits are available by exploiting the linear dynamics relative to the equilibrium points. In particular, the oscillatory linear solutions in the vicinity of the collinear points easily evolve into nonlinear periodic orbits by leveraging the mirror theorem. A periodic spacecraft path in the CR3BP emerges by enforcing multiple, distinct mirror conditions. This constraint is sufficient, though not necessary, to guarantee periodic motion. Thus, any trajectory that possesses two distinct perpendicular xz-plane crossings is a periodic orbit and initial conditions for such orbits are selected with the form

$$\vec{q}_0 = \left\{ x \quad 0 \quad z \quad 0 \quad \dot{y} \quad 0 \right\}^T . \tag{3.73}$$

Although the number of free variables in the initial state is reduced from six to three, an infinite set of such perpendicular crossings exist and further information is required to isolate a single periodic solution. Accordingly, linear solutions from the center subspaces associated with the collinear points are leveraged as initial estimates for periodic, nonlinear motion.

To construct periodic (i.e., oscillatory) motion in the nonlinear system, a shooting approach is employed. The linear solution near one of the three collinear points supplies an initial guess for the nonlinear orbit and two mirror constraints are applied, i.e., at the initial state and a state halfway through the orbital period. Once a periodic solution is constructed, a continuation process is applied to generate other periodic orbits with similar geometries, i.e., a *family* of periodic orbits is computed. By applying this process, planar, periodic libration point orbits are produced. A number of representative orbits in three of these families, known as the *Lyapunov Orbits*, are plotted in Figure 3.5.

Additional periodic orbits are computed by leveraging the oscillatory modes of the linear dynamics. The vertical family, for example, exists within the center manifold associated with the collinear libration points and possess a large out-of-plane

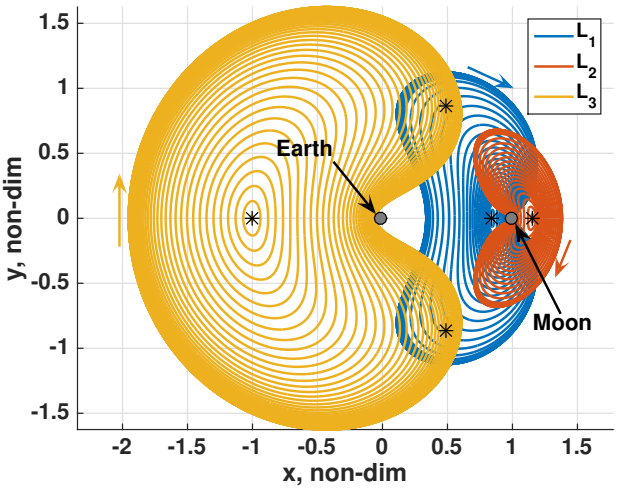

Figure 3.5.: Lyapunov Orbit Families

component. Periodic orbits in the vicinity of the triangular points do not cross the xz-plane and therefore possess no mirror configurations. However, a corrections process that constrains the first and last states along an orbit to be equal is capable of extracting nonlinear periodic orbits from the center manifolds associated with the triangular points. Finally, continuation schemes can identify bifurcations from known families of periodic solutions. By stepping off the known family in the direction of the bifurcation, additional groups of periodic solutions emerge.

3.4 Continuation Schemes

Like multiple shooting, continuation strategies are a tool to explore motion near a reference solution. While multiple shooting is employed to identify solutions that meet a set of constraints, continuation methods generate *families* of similar solutions that all meet the same set of constraints. For example, these families include periodic orbits, quasi-periodic motion, and transfer arcs. Two continuation approaches are detailed here: (i) natural parameter continuation, which evolves a family along a

physical parameter such as x, y, or time-of-flight; and (ii) pseudo-arclength continuation, which leverages a nonphysical parameter to step along a family of solutions.

3.4.1 Natural Parameter Continuation

Natural parameter continuation evolves a family of solutions along a natural (i.e., physical) variable such as a position state, velocity state, time, or Jacobi constant. Such an algorithm is simple to conceptualize. Consider a solution with an initial state represented by

$$\vec{q}_{0,0} = \begin{Bmatrix} x_{0,0} & y_{0,0} & z_{0,0} & \dot{x}_{0,0} & \dot{y}_{0,0} & \dot{z}_{0,0} & T_{0,0} & \tau_{0,0} \end{Bmatrix}^T . \tag{3.74}$$

With some knowledge of the desired family of solutions, a natural parameter is identified that is varied to generate additional solutions. Ideally, each family member is uniquely identified by the value of this parameter. Such families are termed *single-parameter families*. In practice, many families are not uniquely parameterized by a single variable, but subsets of a family can be treated as single-parameter sets.

As an example, consider the Earth-Moon L_1 northern halo family. A 3D representation of a section of this continuous family of periodic orbits is computed via natural parameter continuation and displayed in Figure 3.6(a). The evolution of the x and z components of the initial state along each halo orbit are depicted in Figure 3.6(b). The initial family member is identified on the parameter curve as the top-left blue asterisk near $z_0 = 0$ and represented by the initial state

$$\vec{q}_{0,0} = \begin{Bmatrix} x_{0,0} & 0 & z_{0,0} & 0 & \dot{y}_{0,0} & 0 & \tau_{0,0} & T_{0,0} \end{Bmatrix}^T . \tag{3.75}$$

To continue the family, a small step in z_0 produces a new initial state,

$$\vec{q}_{0,1} = \begin{Bmatrix} x_{0,0} & 0 & z_{0,1} & 0 & \dot{y}_{0,0} & 0 & \tau_{0,0} & T_{0,0} \end{Bmatrix}^T , \tag{3.76}$$

where $z_{0,1} = z_{0,0} + \Delta z_0$. A corrections process is then employed to adjust this state to yield a periodic orbit with the specified $z_{0,1}$ coordinate. This process is applied iteratively to produce a range of halo orbits. However, inspection of the parameter

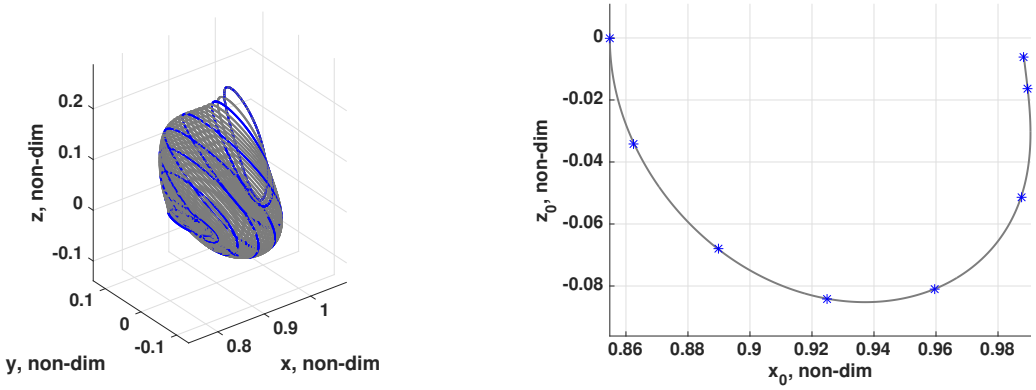

(a) 3D orbit view in the Earth-Moon rotating frame

(b) Evolution of x and z along family

Figure 3.6.: Earth-Moon L_1 northern halo family computed via natural parameter continuation; several members are highlighted in blue

evolution in Figure 3.6(b) reveals that near $x_0 = 0.92$, the family ceases to evolve in z for a time. In this subset of the family, perturbing a family member in the z direction and fixing that component fails to yield a new family member. Although the first third of the family is uniquely identified by its z_0 component and is considered a single-parameter set, the family as a whole requires multiple parameters to uniquely identify solutions.

By incorporating multiple natural parameters into the continuation scheme, greater computational flexibility is achieved. In the Earth-Moon L_1 halo example, steps in the x direction are useful to identify solutions for $0.9 \leq x_0 \leq 0.96$. However, for $x_0 > 0.96$, the algorithm again benefits from steps in the z coordinate because the change in x_0 becomes small relative to the change in z_0 as the family evolves. Accordingly, a procedure that computes the slope of the (x_0, z_0) parameter curve is able to switch between stepping directions in a guided scheme to compute the halo family in Figure 3.6.

The natural parameter step technique can require small step sizes due to the crude approximation of an initial state. Consider, for example, the converged solution represented by a blue asterisk in Figure 3.6(b) with x_0 slightly larger than 0.86. Let the next desired x_0 value be 0.89 (located at the next blue asterisk). The initial guess for this solution includes $z_0 \approx -0.033$, far from the true z_0 at about -0.07. The differential corrections process may not be able to smoothly make this leap between solutions and, consequently, fail to converge. The transition between solutions is facilitated by decreasing the step size, but such an approach requires additional computational resources to evolve the family. A large step size is possible by leveraging a more intelligent initial guess for the initial state of the next member along the evolving family.

To alleviate this initial state prediction inaccuracy, the parameter curve between the two previous solutions is approximated by a second order polynomial in z_0. Let $\hat{x}_{0,n+1}$, $\hat{\dot{y}}_{0,n+1}$, and $\hat{\tau}_{0,n+1}$ be estimates for the next solution to be computed, and let $z_{0,n+1}$ be the desired z_0 value for the next solution. Three scalar second order polynomial expressions are therefore given by

$$\begin{aligned}
\hat{x}_{0,n+1} &= \left\{ z_{0,n+1}^2 \quad z_{0,n+1} \quad 1 \right\} \left\{ c_{x,2} \quad c_{x,1} \quad c_{x,0} \right\}^T, \\
\hat{\dot{y}}_{0,n+1} &= \left\{ z_{0,n+1}^2 \quad z_{0,n+1} \quad 1 \right\} \left\{ c_{\dot{y},2} \quad c_{\dot{y},1} \quad c_{\dot{y},0} \right\}^T, \\
\hat{\tau}_{0,n+1} &= \left\{ z_{0,n+1}^2 \quad z_{0,n+1} \quad 1 \right\} \left\{ c_{\tau,2} \quad c_{\tau,1} \quad c_{\tau,0} \right\}^T,
\end{aligned}$$

where the coefficients c are based on previously converged solution initial states. In matrix form, these equations are rewritten as

$$\begin{Bmatrix} \hat{x}_{0,n+1} \\ \hat{\dot{y}}_{0,n+1} \\ \hat{\tau}_{0,n+1} \end{Bmatrix} = \left\{ z_{0,n+1}^2 \quad z_{0,n+1} \quad 1 \right\} \mathbf{C}, \tag{3.77}$$

where the matrix $\mathbf{C}$ is developed from the coefficients,

$$\mathbf{C} = \begin{bmatrix} c_{x,2} & c_{\dot{y},2} & c_{\tau,2} \\ c_{x,1} & c_{\dot{y},1} & c_{\tau,1} \\ c_{x,0} & c_{\dot{y},0} & c_{\tau,0} \end{bmatrix}. \tag{3.78}$$

To determine the coefficients in $\mathbf{C}$, a least squares approach is employed. The linear system

$$\mathbf{AC} = \mathbf{B} \tag{3.79}$$

represents the relationship between the independent variable (in this example, z_0) stored in $\mathbf{A}$ and the desired dependent variables (x_0, $\dot{y}_0$, and τ_0) stored in $\mathbf{B}$:

$$\mathbf{A} = \begin{bmatrix} z_{0,n-m}^2 & z_{0,n-m} & 1 \\ z_{0,n-(m-1)}^2 & z_{0,n-(m-1)} & 1 \\ \vdots & \vdots & \vdots \\ z_{0,n-1}^2 & z_{0,n-1} & 1 \\ z_{0,n}^2 & z_{0,n} & 1 \end{bmatrix}, \qquad \mathbf{B} = \begin{bmatrix} x_{0,n-m} & \dot{y}_{0,n-m} & \tau_{0,n-m} \\ x_{0,n-(m-1)} & \dot{y}_{0,n-(m-1)} & \tau_{0,n-(m-1)} \\ \vdots & \vdots & \vdots \\ x_{0,n-1} & \dot{y}_{0,n-1} & \tau_{0,n-1} \\ x_{0,n} & \dot{y}_{0,n} & \tau_{0,n} \end{bmatrix},$$

where $m+1 \geq 3$ is the number of data points to include in the least squares fit. In general, $\mathbf{A}$ is not square and equation (3.79) is solved via the left inverse:

$$\mathbf{C} = (\mathbf{A}^T\mathbf{A})^{-1}\mathbf{A}^T\mathbf{B}. \tag{3.80}$$

The predicted values $\hat{x}_{0,n+1}$, $\hat{\dot{y}}_{0,n=1}$, and $\hat{\tau}_{0,n+1}$ are computed by projecting $\mathbf{B}$ onto the column space of $\mathbf{A}$, as expressed in equation (3.77). The accuracy gained by predicting the orbit initial state allows the natural parameter continuation algorithm to employ larger steps between solutions and reduces the number of iterations required to evolve a family of trajectories. Additionally, because the least squares predictions yield initial guesses closer to the family parameter curve, fewer correction iterations are required to converge upon each family member.

3.4.2 Pseudo-Arclength Continuation

Natural parameter continuation evolves a family along an intuitive physical parameter curve, but requires some a priori knowledge or experimentation to identify useful parameters. The pseudo-arclength continuation scheme offers a more robust evolution of the family, at the expense of intuition as the method varies a nonphysical parameter to step along a family of solutions [27, 28]. Similar to the least squares-enabled natural parameter method, pseudo-arclength continuation exploits information from previous solutions to predict the next periodic orbit.

Pseudo-arclength continuation (PAC) is formulated as a multiple shooting problem. Consider a discretized family member with n nodes, represented by a $w \times 1$ design variable vector $\vec{X}$, subject to the constraints represented by a $u \times 1$ vector $\vec{F}$, with associated $u \times w$ Jacobian matrix $\mathbf{J}$. By definition, vectors in the nullspace of $\mathbf{J}$ lie tangent to solution space of family members; stepping along this nullspace direction is analogous to stepping along the family.

To construct a Jacobian with a one-dimensional nullspace, several modifications are incorporated into the general multiple shooting process described previously. First, let the total time of flight along the trajectory be τ_t and the time of flight between each node be $\tau_t/(n-1)$. Although individual times-of-flight cannot vary independently of one another, τ_t is included in the design variable vector:

$$\vec{X} = \begin{Bmatrix} \vec{q}_1 & \dots & \vec{q}_n & \tau_t \end{Bmatrix}^T . \tag{3.81}$$

This amendment reduces the number of design variables, thus, the problem requires fewer constraints to reach the desired rank. Epoch time T is computed similarly for each node as $T_i = T_0 + i/(n-1)\tau_t$; for this sample discussion, consider a fixed initial epoch such that T_0 does not appear in the design vector. Thus, there are $6n+1$ design variables. The constraint vector includes, at minimum, $6(n-1)$ position and velocity continuity constraints. Six more constraints are appended to $\vec{F}$ to equate $w = u+1$. These constraints are arbitrary but often represent periodicity constraints or mirror condition constraints for periodic motion. Note that, to increase the rank of

$\mathbf{J}$, the relationships between the additional constraints and the design variable vector, expressed as $\frac{\partial \vec{F}}{\partial \vec{X}}$, must be linearly independent of all other constraints.

The PAC scheme computes a step tangent to the family, or along the right nullspace of $\mathbf{J}$. Let $\Delta\vec{X}_i = \mathcal{N}(\mathbf{J_i})$ where $\mathbf{J}_i$ represents the Jacobian matrix for a previously converged family member. The initial guess for the next family member is then

$$\vec{X}_{i+1} = \vec{X}_i^* + s\Delta\vec{X}_i, \tag{3.82}$$

where s is a scaling constant and $\vec{X}_i^*$ is a previously converged family member. This new guess is corrected using an augmented constraint vector and, necessarily, an augmented Jacobian matrix. As with natural parameter continuation, the new family member is constrained to be exactly the prescribed step away from the previous solution. However, where natural parameter continuation steps in a single variable, PAC steps in all design variables simultaneously. The constraint to ensure this step is maintained is expressed as

$$F_{PAC} = (\vec{X}_{i+1} - \vec{X}_i^*)\Delta\vec{X}_i - s = 0. \tag{3.83}$$

Though this expression seems complex, $\vec{X}_i^*$, $\Delta\vec{X}_i$, and s are all constant, thus the partial derivative of F_{PAC} with respect to the current design variable vector $\vec{X}_{i+1}$ is simply the nullspace vector, $\Delta\vec{X}_i$. Accordingly, the augmented constraint vector and Jacobian matrix are given by

$$\vec{G}(\vec{X}_{i+1}) = \begin{Bmatrix} \vec{F}(\vec{X}_{i+1}) \\ (\vec{X}_{i+1} - \vec{X}_i^*)\Delta\vec{X}_i - s \end{Bmatrix}, \qquad D\vec{G}(\vec{X}_{i+1}) = \begin{bmatrix} \mathbf{J}_i \\ \Delta\vec{X}_i \end{bmatrix}.$$

As the matrix $D\vec{G}$ is square and full-rank, the update equation is solved via a regular inverse. Since an exact solution exists, PAC effectively converts any family of solutions to a single-parameter set. Because each solution is uniquely identified by this nonphysical parameter, PAC is robust to a complex geometry and natural parameter fluctuations along a family. To illustrate this robustness, recall the Earth-Moon halo family evolution supplied by the natural parameter continuation scheme and

pictured in Figure 3.6. The same family is evolved with PAC and pictured in Figure 3.7. Pseudo-arclength continuation is able to compute a much larger family of orbits.

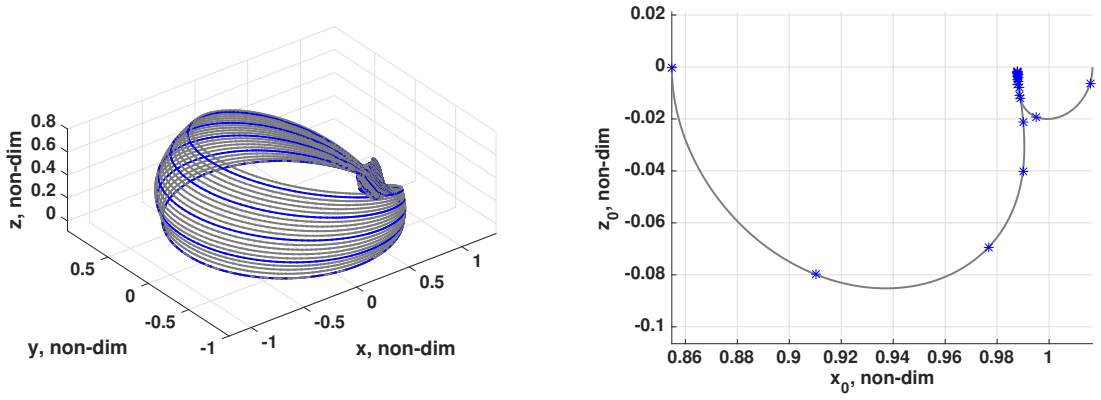

(a) 3D orbit view in the Earth-Moon rotating frame

(b) Evolution of x and z along family

Figure 3.7.: Earth-Moon L_1 northern halo family computed via pseudo-arclength continuation; several members are highlighted in blue

In fact, if left unchecked, the algorithm continuously cycles through the L_1 northern halo family, to the southern family, and back to the northern family; the two families are, actually, two halves of the same family. The halo orbits computed previously are still depicted in Figure 3.7(a), but are dwarfed by larger family members that encircle the Earth-Moon system. The (x_0, z_0) parameter curve reveals why natural parameter continuation was unable to compute these additional family members. At $x_0 \approx 0.99$, near the cluster of blue asterisks, the parameter curve evolves along a tight loop, switching rapidly between near-vertical and near-horizontal solutions in the (x_0, z_0) space. Even with intelligent stepping and least squares predictions, the natural parameter continuation formulation is unable to computationally navigate this loop in the parameter space. Pseudo-arclength continuation experiences no such difficulty because the PAC method parameterizes the family with a *single* nonphysical value. Although PAC supplies less intuition about the evolution of a family of solutions, it

is robust to complex changes in the natural parameter space and assimilates easily into the multiple-shooting process.

3.5 Invariant Manifolds in Trajectory Design

Stable, unstable, and center invariant manifolds computed from linear dynamics relative to a reference solution supply useful approximations to the nonlinear dynamical behavior. For example, periodic motion in the vicinity of the libration points is initialized by isolating states that lie within the center manifold of the libration point. These initial approximations are transitioned into the full nonlinear system via a corrections process and expanded into a family of periodic solutions via continuation methods. A similar analysis is completed by investigating the linear dynamics near a periodic orbit. Periodic motion appears as a fixed point on a stroboscopic map, analogous to the equilibrium points fixed in configuration space. The stable and unstable invariant manifolds of the periodic orbit are leveraged to identify transit solutions that flow toward and away from the periodic orbits. Similarly, the center manifold of a periodic solution contains quasi-periodic motion that oscillates and remains bounded in the vicinity of the periodic solution.

3.5.1 The Stable and Unstable Subspace: Transit Manifold Arcs

The stable and unstable invariant manifolds emanating from periodic solutions supply families of transit arcs that asymptotically approach the periodic orbit in forward and backward time, respectively. Though some periodic solutions do not possess stable and unstable subspaces, many do and the resulting invariant manifolds offer low-cost transfer options to and from the periodic trajectory. To compute these manifold structures, choose a point $\vec{q}_*$ along a periodic solution. The monodromy matrix $\mathbf{M}$ at any point is computed by propagating motion from the selected point for one period T. This matrix represents the linearization of a stroboscopic map on which the periodic orbit is a fixed point.

The eigenvalues of $\mathbf{M}$ exist independently of the isolated fixed point along the orbit. Recall that if the periodic solution has a stable and unstable subspace, at least two of the eigenvalues of $\mathbf{M}$ occur as a real reciprocal pair, i.e., $\lambda^S > 1$ and $\lambda^U = 1/\lambda^S$. The eigenvectors associated with these eigenvalues are then $\vec{v}^U$ and $\vec{v}^S$, respectively, where $\vec{v}^U$ represents the local unstable manifold and $\vec{v}^S$ represents the local stable manifold. The global invariant manifold associated with the periodic solution is computed by perturbing $\vec{q}_*$ along the stable (unstable) eigenvector and propagating for some duration in reverse (forward) time. Accordingly, an initial state on the global unstable manifold arc is expressed by

$$\vec{q}_{U,0} = \vec{q}_* + \epsilon \frac{\vec{v}^U}{\|\vec{v}^U\|}, \tag{3.84}$$

where ϵ is some small step-off distance along the unstable eigenvector, i.e., along the unstable subspace. Note that the sign of the eigenvector is non-unique and can be multiplied by negative one to compute the other half of the manifold arc. For consistency, let eigenvectors with a positive x-component be in the positive (+) direction, i.e., $\vec{v}^{U+}$. Additionally, note that the eigenvector may also be nondimensionalized by dividing by only the magnitude of the position components rather than the magnitude of the entire vector (position and velocity components). A selection of stable and unstable manifolds arcs associated with a Sun-Earth L_1 Lyapunov are depicted in Figure 3.8; only the (+) branch of the manifolds are plotted.

3.5.2 The Center Subspace: Quasi-Periodic Orbits

The center subspace associated with fixed points supplies many bounded, oscillatory arcs offering many applications for trajectory design. The center subspace associated with the equilibrium solutions to the EOMs contains periodic orbits such as the Lyapunov, vertical, halo, and axial families, among others. Each of these periodic solutions exists as a fixed point on a stroboscopic map and may possess center manifolds of their own. As the equilibrium solution center manifolds contain oscillatory motion about the equilibrium point in the form of periodic solutions, the periodic

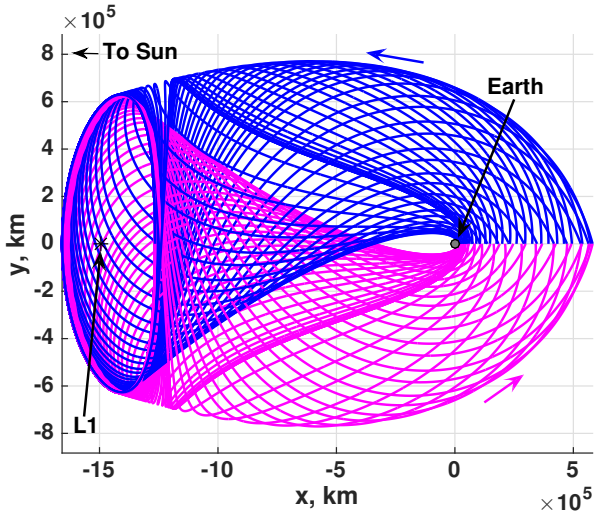

Figure 3.8.: Stable (blue) and unstable (magenta) manifold arcs from a Sun-Earth L_1 Lyapunov orbit, viewed in the Sun-Earth rotating frame

solution center manifolds also include oscillatory motion. Such oscillatory solutions near periodic orbits are termed *quasi-periodic* orbits or *torus* structures.

A quasi-periodic orbit, or torus, in the vicinity of a periodic solution is parameterized by two angles. First, a *longitudinal* angle, θ_0, represents the position of a point, e.g., a spacecraft, about one axis of rotation as illustrated in Figure 3.9. A second *latitudinal* angle, θ_1, locates the point of interest about the second axis of rotation. In the illustration, the torus is represented by a blue donut-like shape; encapsulated within the torus is a red arc depicting a periodic solution. A purple circle locates the point of interest. The angles θ_0 and θ_1 evolve with angular frequencies ω_0 and ω_1.

Based on the formulation described by Olikara and Scheeres, the torus is initiated from a stroboscopic map at some fixed θ_0 [29]. A set of N points around the cross section of the torus are generated by perturbing the periodic orbit (with period T) along the center eigenvector direction for a variety of θ_1 values. Let λ^C be a center (i.e., complex and on the unit circle) eigenvalue of $\mathbf{M}$ with associated eigenvector $\vec{v}^C$.

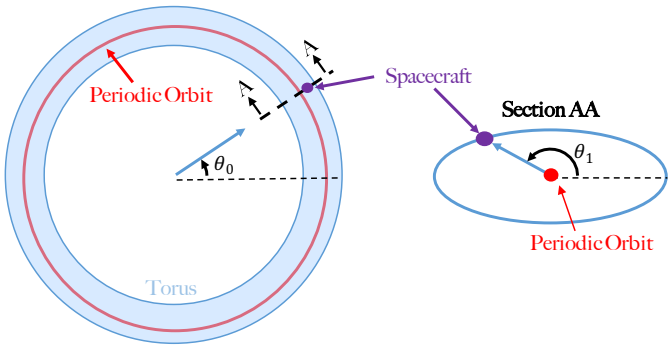

Figure 3.9.: Basic representation of a simple torus (blue) near a periodic orbit (red). The position of a point, e.g., a spacecraft, on the torus is described by two angles, θ_0 and θ_1

Consider a set of N equally spaced angles $\left\{\theta_j \;\middle|\; 0 \leq \theta_j < 2\pi\right\}$ that include $\theta_1 = 0$ but not $\theta_1 = 2\pi$. A set of points around the torus cross section are then defined as

$$\vec{q}_{0,j} = \vec{q}_* + \epsilon \left(\text{real}\left[\vec{v}^C\right] \cos\theta_j - \text{imag}\left[\vec{v}^C\right] \sin\theta_j \right), \tag{3.85}$$

where ϵ is again some small step-off distance from the periodic reference solution $\vec{q}_*$. These initial points on the torus are propagated to the next map iteration, i.e., until time $t = T$. It is assumed that ω_0 and ω_1 are not resonant, thus the new map states, $\vec{q}_{f,j}$ are rotated slightly from the originating points by some angle ρ. In other words, although the stroboscopic map captures points on the torus at a single specified value of θ_0, the value of θ_1 corresponding to each map crossing shifts by angle ρ every iteration.

Although an initial estimate for the quasi-periodic torus is straightforwardly initialized from a periodic orbit, the initial guess requires adjustment to form a true quasi-periodic structure. The frequency ω_0 is approximated from T as $\omega_0 = 2\pi/T$. The angle ρ and frequency ω_1 are proportional, i.e., $\rho = T\omega_1$, and an initial estimate for ρ is obtained from the orientation of $\vec{v}^C$ in the complex plane,

$$\rho = \arccos\left(\text{real}\left[\vec{v}^C\right]\right) = \arcsin\left(\text{imag}\left[\vec{v}^C\right]\right), \tag{3.86}$$

where $\vec{v}^C$ has been normalized to have unit length. Let $\vec{u}_j$ be a Fourier representation of the map crossing $\vec{q}_{f,j}$, parameterized in θ_1 with N terms in the expansion. Additionally, let the map H relate initial points $\vec{q}_{0,j}$ to the approximation $\vec{u}_j$ of next map iteration $\vec{q}_{f,j}$ such that $\vec{u}_j = \vec{H}\left(\vec{q}_{0,j}, T, \rho\right)$. Recall that, on the true quasi-periodic torus, $\vec{u}_j$ is rotated from the originating map crossing by angle ρ. This constraint is captured by enforcing an invariance condition

$$\mathbf{R}(-\rho)\vec{H}\left(\vec{q}_{0,j}, T, \rho\right) - \vec{q}_{0,j} = \vec{0}, \tag{3.87}$$

where $\mathbf{R}(-\rho)$ is a rotation operator through angle ρ. A corrections scheme is constructed to enforce this invariance condition between each of the N points and the Fourier representation of the subsequent stroboscopic map crossing. An additional constraint on the Jacobi constant value is applied to limit the energy of the quasi-periodic solution. The design variable vector includes initial states $\vec{q}_{0,j}$, period T, and angle ρ, which shift slightly during corrections from the estimates supplied by the reference periodic orbit.

Once a torus is corrected, a continuation scheme is implemented to generate a family of tori. Both pseudo-arclength continuation and naturual parameter continuation can be employed to generate a family of tori, but additional constraints must be placed on the solution to reduce the family to a single-parameter evolution. Phase constraints may be placed on θ_0 and θ_1, or physical constraints can be applied to specific points on the torus [29, 30]. As an example of a family of quasi-periodic solutions, several sample quasi-vertical, or *Lissajous*, orbits near the Sun-Earth L_1 libration point are plotted in Figure 3.10. The left frame depicts an arc along a torus near the original vertical orbit. The center and right frames depict paths on tori surfaces further along the family.

It is clear that, like the center manifolds associated with the fixed equilibrium points, the center manifolds corresponding to periodic solutions include a diverse set of solutions that offer further insight into the dynamics in the CR3BP. Though the precise mathematical structures (such as periodic solutions, invariant manifolds, and quasi-periodic structures) exist only in simplified dynamical models such as the

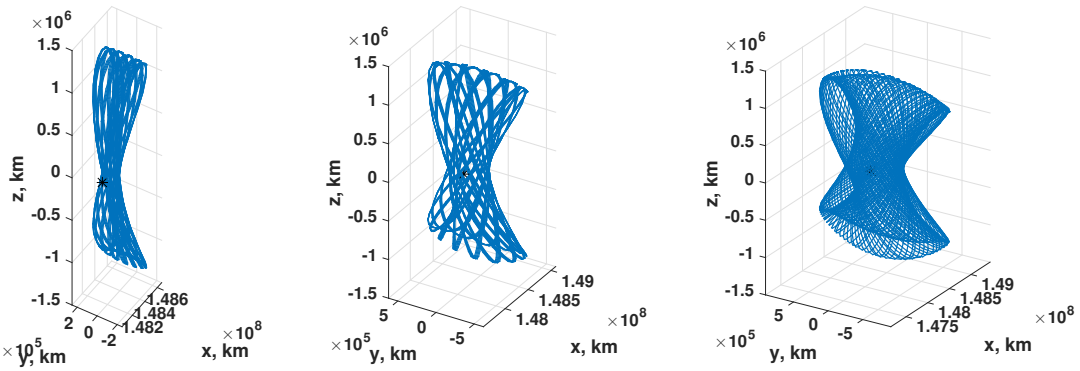

Figure 3.10.: Three Sun-Earth L_1 Lissajous quasi-periodic structures in the Sun-Earth rotating frame

CR3BP, the solutions are approximately retained in higher-fidelity models, including the BC4BP and ephemeris environments. As such, analysis conducted in the CR3BP supplies useful initial designs that are later straightforwardly transitioned in higher-fidelity models.

3.6 Poincaré Mapping Techniques

The analysis of the six-dimensional spatial CR3BP is facilitated by techniques that reduce the dimension of the problem, such as Poincaré mapping. A Poincaré map is essentially a projection into a lower-dimensional space to simplify the analysis by seeking patterns in the design space and is accomplished by fixing specific aspects of the problem. A surface of section, mathematically termed a *hyperplane*, defines this projection and may represent a constraint on a physical state, such as $x = 0$ (the yz-plane) or $z = 0$ (the xy-plane) [21]. The hyperplane may also reflect a nonphysical projection and fix time, or constrain a relationship between position and velocity such that all points on the hyperplane are apses relative to one of the primaries. The constraint imposed by the hyperplane reduces the dimension of the problem, or the number of unknown variables, by one. To demonstrate this process, a map is leveraged

to reduce the four-dimensional planar CR3BP to a two-dimensional problem that is fully described by the map. Higher-dimensional maps are also examined as tools to explore the full spatial problem [26, 31, 32].

3.6.1 Reduction of the Planar CR3BP

A path in the planar CR3BP is is completely described by four states: two position coordinates (x, y) and two velocity coordinates ($\dot{x}$, $\dot{y}$). Accordingly, a single four-dimensional initial state can be evolved in time to yield a trajectory. By employing a Poincaré map, each evolving trajectory in the design space is collected together and projected to reduce the analysis of the solution space to a two-dimensional problem that is easily represented by a typical two-parameter plot. Consider a hyperplane Σ that fixes $y = 0$. That is, a planar trajectory is represented on the map by a point at the location where the arc passes through the x-axis. The two velocity states are reduced to a single unknown by fixing the Jacobi constant of all map crossings and the sign of one of the velocity states. In other words, every trajectory represented on the map possess the same Jacobi constant value. Let the horizontal velocity $\dot{x}$ be the other quantity plotted on the map, as in Figure 3.11, with $\dot{y} > 0$ for all points. Accordingly, any point on the map is rapidly identified with a specific x and $\dot{x}$ value, y is zero, and $\dot{y}$ is obtained from the equation for Jacobi constant. Thus, the Poincaré technique reduces the space from $\mathbb{R}^4$ to $\mathbb{R}^2$.

In addition to a simplification of the higher-dimensional design space, Poincaré maps can supply significant insight into dynamical structures in the CR3BP [17]. The map in Figure 3.11 illustrates several such structures in the midst of chaotic motion. The concentric rings in the center of the map represent quasi-periodic motion; the center of the concentric set is a periodic orbit. A set of four *islands* about the set of quasi-periodic solutions represents additional periodic and quasi-periodic solutions. Transitions from one solution to another may be accomplished by moving along the vertical axis, analogous to performing a Δv to adjust $\dot{x}$ and $\dot{y}$. These types of maps

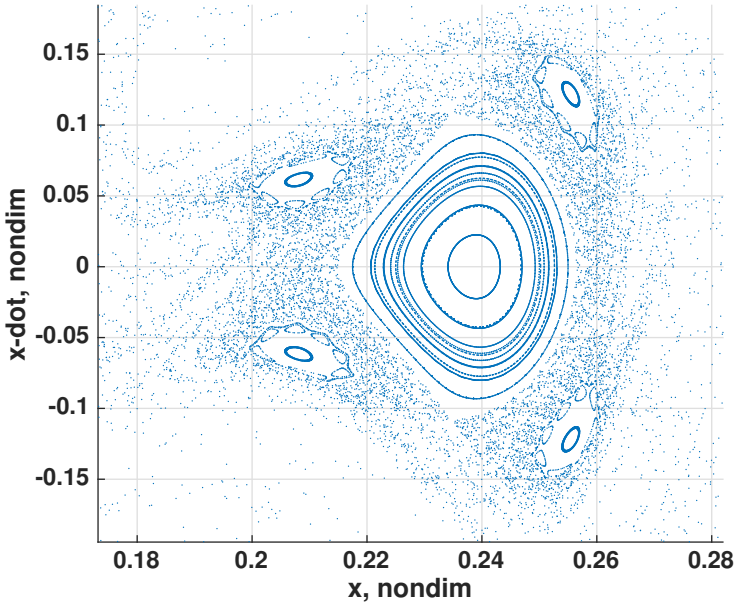

Figure 3.11.: Planar Poincaré map at $y = 0$ and $C = 3.144$; all map crossings possess $\dot{y} > 0$ (i.e., the map is one sided)

are employed by many authors to facilitate spacecraft orbit design in the CR3BP [14, 26, 33, 34, 35].

3.6.2 Higher-Dimensional Poincaré Maps

In general, motion in the CR3BP is described by six states and conventional mapping techniques are unable to represent the full state on a two-parameter plot. However, other techniques are available to increase the amount of information available from such a plot. For example, color may be leveraged to represent an additional dimension, and glyphs such as vectors can also incorporate additional information on a map. Maps that employ such devices are termed *higher-dimensional maps*, and are useful to represent spatial trajectories in the CR3BP [26, 31, 32]. Higher-dimensional Poincaré maps that utilize color *and* glyphs are leveraged in this investigation to identify links between arcs that exist naturally in different CR3BP systems. To this

end, consider a map, illustrated in Figure 3.12, with a hyperplane at $z = 0$. The remaining two positions states, x and y, are plotted as a point on the map. The

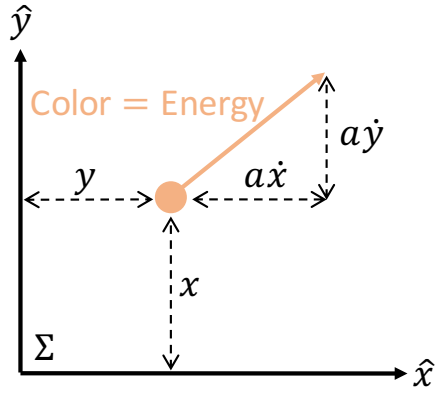

Figure 3.12.: A higher dimensional Poincaré map representing a 6-dimensional state in a 2-dimensional map by employing a hyperplane at $z = 0$

planar velocity states, $\dot{x}$ and $\dot{y}$ are indicated by the orientation and magnitude of a vector emanating from the point and are scaled by some constant a. Finally, the energy value (i.e., Jacobi constant value) is represented by color. Since all position states and two velocity states are known from the point and the vector, the third and final velocity state is obtained from the equation for Jacobi constant. Thus, the full six-dimensional state is represented on the two-dimensional map. Although these maps do not provide the same structural information as the planar CR3BP maps do, higher-dimensional maps are well suited to identify links between various spatial trajectories [32, 36]. In particular, two map crossings with nearby points, similar vector directions and magnitudes, and similar colors possess approximately the same six-dimensional state and likely can be connected at a relatively low cost.

4. ANALYSIS

The analysis of an extended mission concept for LISA Pathfinder (LPF) is facilitated by dividing the process into a series of sub-tasks. First, an understanding of the LPF primary mission orbit is developed and candidate CR3BP trajectories are investigated to approximate the full-fidelity orbit. Next, the target of the extended mission, the gravitational saddle point, is analyzed and modeled. Invariant manifolds are leveraged to provide low-cost transfer options from the LPF primary mission orbit to the saddle point vicinity. Periodic orbits in the Earth-Moon CR3BP are examined as candidate arcs to supply additional saddle point encounters. Alternatively, natural motion in the BC4BP flowing from the invariant manifolds is investigated to the same end. Finally, an end-to-end transfer is constructed by linking these various types of motion and is corrected via multiple shooting techniques.

4.1 A Model for the LPF Primary Orbit

The LISA Pathfinder spacecraft conducts its primary mission in the Sun-Earth L_1 vicinity with an in-plane (i.e., in-ecliptic) amplitude A_y of 800,000 km and out-of-plane amplitude A_z of 500,000 km. However, a smaller orbit with $A_z = 150{,}000$ km is considered in this analysis in an attempt to recreate previous promising designs by Fabacher et al. [3]. A plot of such a reference orbit from a LISA Pathfinder technical report is depicted in Figure 4.1. The coordinate frame employed in this representation differs from the rotating frame $(\hat{x},\ \hat{y},\ \hat{z})$ defined in Section 2.1. Let the coordinate frame in Figure 4.1 be $(\tilde{x},\ \tilde{y},\ \tilde{z})$. The description of the x-axis indicates that $\tilde{x}$ points from the Earth to the Sun, thus $\tilde{x} = -\hat{x}$. Some ambiguity still exists about the relationship between the y and z directions. The rotation of the orbit about L_1 provides the necessary clue: in the $(\hat{x},\ \hat{y},\ \hat{z})$ frame, motion about L_1 proceeds

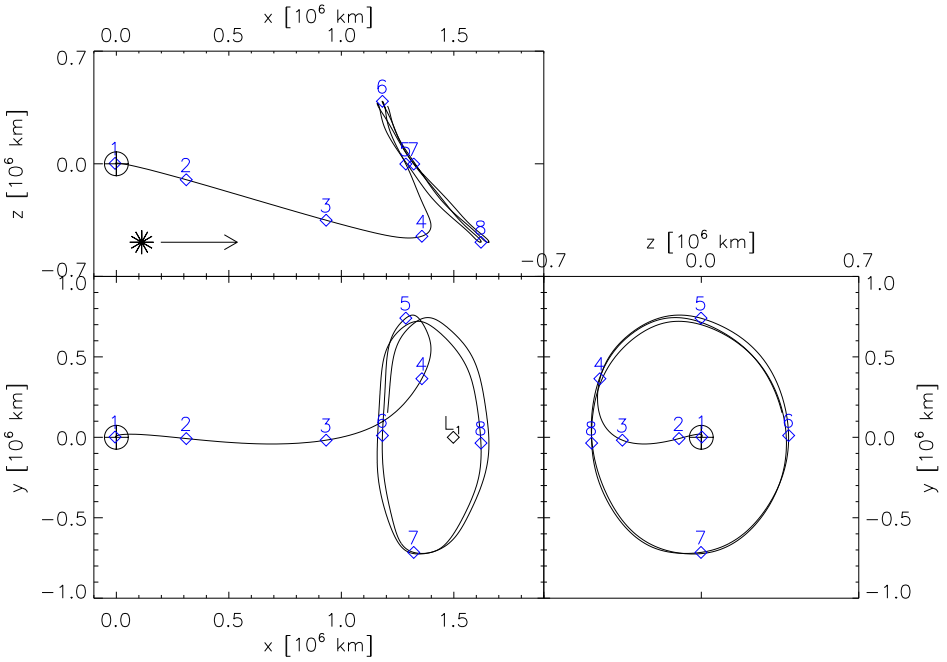

Figure 4.1.: Reference trajectory for LISA Pathfinder about the Sun-Earth L_1 libration point shown in a rotating frame with the Earth at the origin, the x-axis pointing to the Sun, and the xy-plane coincident with the ecliptic plane. The z-axis is chosen to form a right-handed coordinate system. [2]

in the clockwise direction, i.e., it has an angular velocity vector along $-\hat{z}$. The motion depicted in Figure 4.1 rotates about the $\tilde{z}$ direction, hence, $\tilde{z} = -\hat{z}$. As both coordinate frames are right-handed, it follows that $\tilde{y} = \hat{y}$.

The oscillatory motion displayed in the ESA technical report is described as a Lissajous orbit in many publications [1, 2, 8, 9, 3]. However, the visual representations of this motion presented in many of these papers are inconsistent with Lissajous motion at the amplitudes described by the authors. Instead, the motion is much better described by quasi-halo structures. Fabacher et al note that "halo orbits are a special case of Lissajous orbit," thus it is assumed in this investigation that the

LPF primary mission orbit is a quasi-halo orbit (QHO) and that other authors use *Lissajous* to generally imply quasi-periodic motion.

By combining insights about the reference frame definition and the precise orbit designation, it is clear that the LPF primary mission orbit is a quasi-halo in the vicinity of a Sun-Earth L_1 northern halo orbit. Constraints on the A_y and A_z amplitudes limit the number of candidate QHOs, but many options remain. Recall that within the center subspace of an individual periodic orbit, a family of quasi-periodic solutions exist that span a variety of amplitudes. In fact, the amplitudes of revolutions about a single quasi-periodic solution can vary by a large amount. A single Sun-Earth L_1 QHO associated with a family of QHOs, represented in configuration space in Figure 4.2(a), possess a time-varying amplitude history as plotted in Figure 4.2(b). The

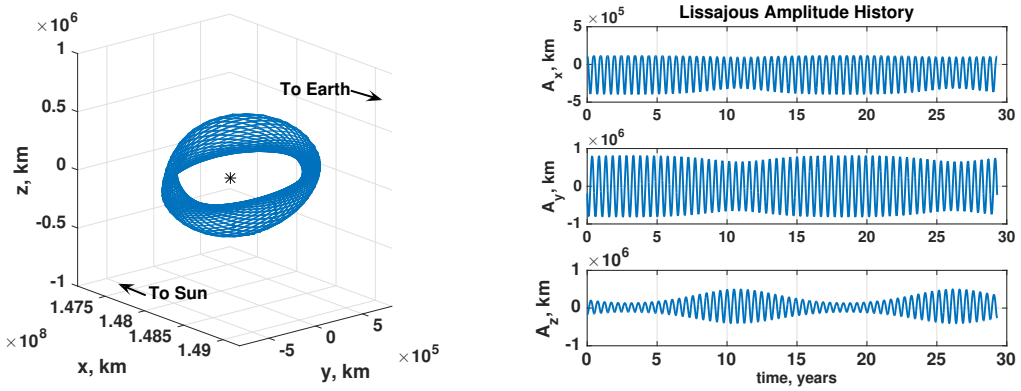

(a) 3D representation in the Sun-Earth rotating frame

(b) Amplitude History

Figure 4.2.: A Sun-Earth L_1 Northern quasi-halo orbit

x-amplitude, A_x, is measured relative to the mean x-coordinate computed for the time-history of the quasi-halo structure, and the y- and z-amplitudes, A_y and A_z, are measured relative to zero. A revolution around the quasi-halo requires slightly less than six months of flight time and experiences amplitudes in the ranges of 622,000 km $\leq A_y \leq$ 837,000 km and 45,000 km $\leq A_z \leq$ 541,000 km. Note that the maximum A_z coincides with the time at which A_y and A_x are minimized. Thus, by selecting

different segments of the quasi-halo structure, orbits with a variety of amplitudes are obtained.

A single QHO can be decomposed into a set of individual revolutions that possess a variety of amplitudes, but this QHO is only one of many structures in a family. Any of the QHOs can be selected to obtain a different amplitude history. To gain insight about the ranges of amplitudes available along a family, the maximum and minimum A_y and A_z amplitudes are computed for each QHO in the family and plotted as a function of orbit index in Figure 4.3. The family originates at a periodic halo

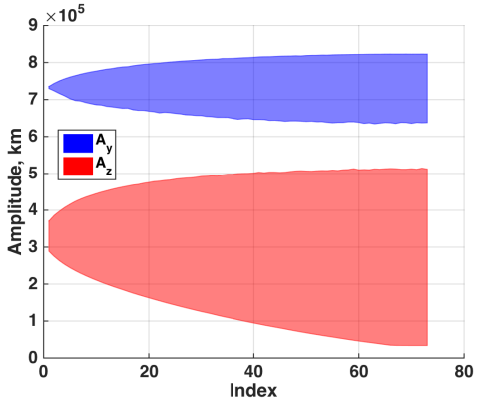

Figure 4.3.: Maximum and minimum amplitudes across a family of quasi-halo orbits that emanate from a halo orbit with Jacobi constant value equal to 3.0007872160

orbit with Jacobi constant value equal to $C = 3.0007872160$ and amplitudes of $A_y =$ 735,000 km and $A_z = 370{,}000$ km. As the family evolves, the quasi-periodic structures grow while remaining in the vicinity of the halo orbit. Accordingly, the maximum and minimum amplitudes expand somewhat symmetrically from the halo dimensions as the family evolves. A QHO with the desired dimensions (i.e., 800,000 km in-plane, 150,000 km out-of-plane) exists after the 20th index depicted in Figure 4.3. Recall that the maximum A_y occurs at the same time as the minimum A_z, thus the QHO possesses revolutions that match these dimensions. The structure associated with the 38th index, plotted in Figure 4.2(a), is selected as it possess the desired A_y and A_z dimensions. This QHO revolution is employed for the duration of the investigation as

the approximated LPF primary mission orbit. Although other segments from different QHO may also be employed, the chosen segment possesses the lowest energy value possible to facilitate low-cost transfers to the saddle point.

4.2 The Saddle Point in the CR3BP and BC4BP

Before a transfer to a gravitational equilibrium point is designed, a working knowledge of the location of the point is constructed. A definition of the saddle point is described in terms of the Sun and Earth gravitational fields, and perturbations from other celestial bodies are considered. The location of the saddle point in Sun-Earth and Earth-Moon rotating coordinates is illustrated, and a scheme to target the saddle point's location is developed for use in corrections processes.

4.2.1 Saddle Point Definition

A gravitational equilibrium point, or *saddle point*, is located where the gravitational accelerations from all massive bodies sum to a net-zero value. Two such points exist in the vicinity of the LPF primary orbit: one where the Sun and Earth gravity fields sum to zero, and one where the Sun and Moon gravity fields sum to zero. Although the effects of MOND may be measured at either saddle point, the Sun-Earth saddle point is the most practical target for the extended mission [37]. This saddle point exists on a line between the Sun and Earth, roughly 259,000 km from Earth. A visualization of the saddle point is presented in Figure 4.4. The two names, *saddle* point and *equilibrium* point, identify the definition of the point in two representations of the Sun-Earth gravitational field. Within the gravitational potential field, plotted in Figure 4.4(a), the point represents a saddle in the field. Alternatively, consider the gravitational acceleration field visualized by the colored surface in Figure 4.4(b). The vertical axis in this figure records the magnitude of the acceleration on a logarithmic scale where large, negative numbers indicate a near-zero acceleration magnitude. In

this case, the saddle point is located where the acceleration magnitude tends to zero, i.e., it is an equilibrium point of the field.

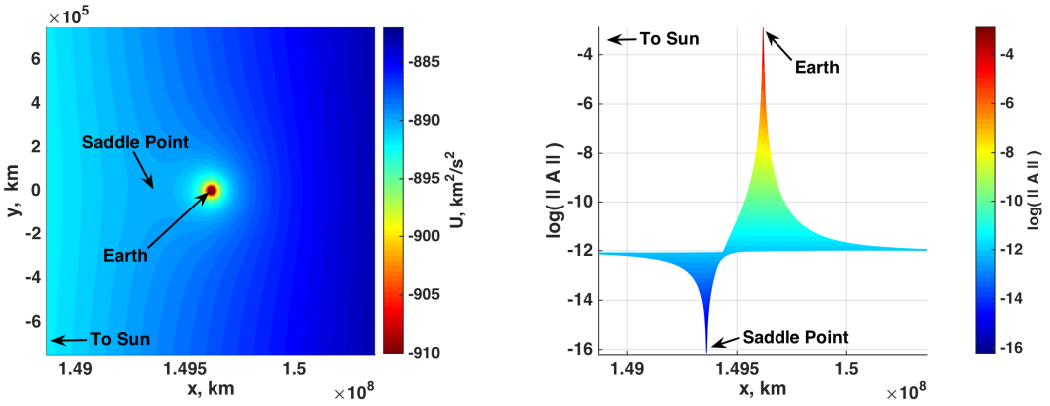

(a) Gravitational Potential Field (b) Gravitational Acceleration Contour

Figure 4.4.: The saddle point visualized as a saddle in the gravitational potential field and as a local minimum in the gravitational acceleration field

4.2.2 n-Body Saddle Point

The location of the Sun-Earth saddle point is clear from the depictions of the local gravity field and is computed by solving a simple second-order polynomial. Consider a point on the Sun-Earth line at position x relative to the Sun-Earth barycenter. Equating the accelerations from both bodies at this point yields the expression

$$\frac{m_s}{(x_s - x)^2} = \frac{m_e}{(x_e - x)^2} \quad \rightarrow \quad \frac{(1-\mu)}{(-\mu - 1)^2} = \frac{\mu}{(1 - \mu - x)^2}, \tag{4.1}$$

where m_s and m_e are the masses of the Sun and Earth, respectively, and x_e and x_s are the locations of the Sun and Earth on the Sun-Earth line relative to the barycenter, i.e., in Sun-Earth rotating coordinates. An application of the quadratic formula offers a solution for the location of the Sun-Earth saddle point:

$$x = \frac{2\mu - 2\mu^2 - \sqrt{\mu(1-\mu)} - 1}{2\mu - 1} \tag{4.2}$$

However, the Sun and Earth are not the only celestial bodies to produce significant gravitational accelerations in this region. To investigate the impact of other celestial bodies, consider the additional gravitational accelerations depicted in Figure 4.5. Each signal in this figure represents the time-varying distance between the Sun-Earth saddle point and the position of the saddle point as computed by incorporating the Sun, Earth, and an additional third body. The greater the distance between the two points, the larger the perturbation due to the additional third body. Because the

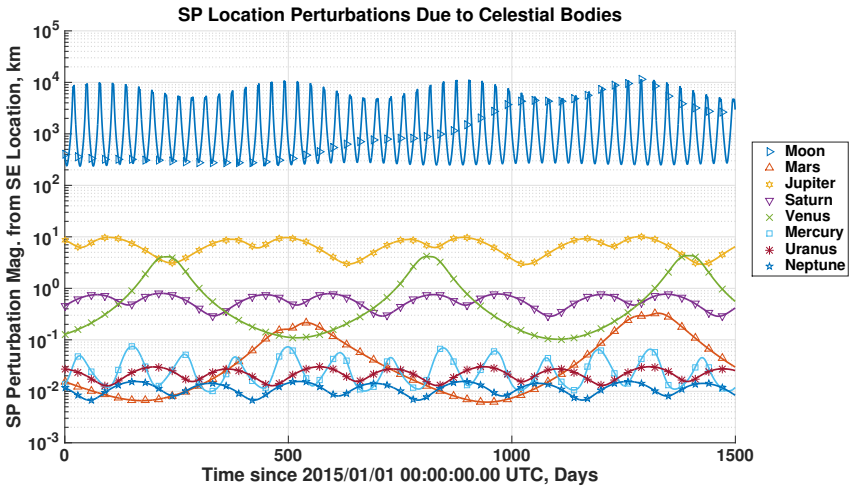

Figure 4.5.: Perturbations of the Sun-Earth-P_n saddle point from the Sun-Earth saddle point position due to various significant celestial bodies P_n

saddle point exists in a location with net-zero gravitational acceleration, its position is computed by locating the roots (i.e., zeros) of the total acceleration function via a Newton-Raphson process that employs the Sun-Earth saddle point location as an initial guess. The positions of all celestial bodies, including the Sun and Earth, are acquired from the Navigation and Ancillary Information Facility (NAIF) SPICE data sets for a five-year duration beginning on Jan 1, 2015 [38]. As is evident from Figure 4.5, the largest perturbation to the saddle point's position is caused by the Moon, with perturbations on the order of hundreds to tens of thousands of kilometers. Clearly, lunar effects must be considered when seeking passes within 100 km of the saddle

point. Both Jupiter and Venus perturb the saddle point's position by as much as 10 km, but these perturbations are ignored in this investigation as their impacts shift the saddle point by less than the permitted pass distance. All other celestial bodies supply comparatively negligible perturbations and are also ignored.

Due to the perturbing effects of lunar gravity, the saddle point's location in the Sun-Earth rotating frame oscillates over time with a period identical to the lunar synodic month. The location of the Sun-Earth and Sun-Earth-Moon saddle points over a period of 90 days appear in Figure 4.6. The Sun-Earth saddle point is represented by a blue dot and the perturbation relative to the Sun-Earth saddle point approximation due to lunar gravity is represented by the red oscillatory arc. The addition of the Moon's gravity perturbs the saddle point's location by roughly 5000 to 10000 km in the $\hat{x}$ direction, 4000 km in the $\hat{y}$ direction, and approximately 2000 km in the $\hat{z}$ direction, normal to the ecliptic plane. The extended mission design for LISA Pathfinder (LPF) must accommodate these perturbations to achieve a pass distance within 100 km of the Sun-Earth-Moon saddle point (hereafter termed saddle point, or SP).

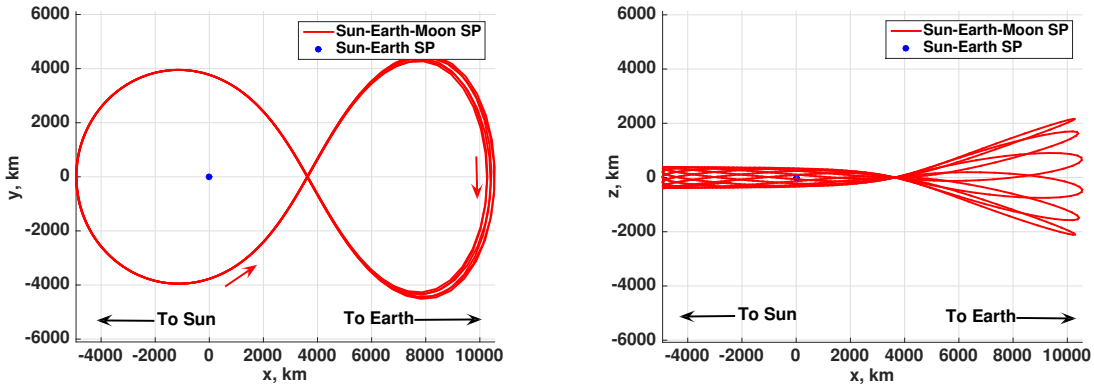

(a) xy projection

(b) xz projection

Figure 4.6.: Sun-Earth-Moon saddle point location in the Sun-Earth rotating frame relative to the fixed location of the Sun-Earth saddle point, over a period of 90 days

A visualization of the saddle point in the Earth-Moon rotating frame provides additional insight. Because the Sun-Earth-Moon saddle point remains near the Sun-Earth saddle point, which exists at a fixed distance from Earth, the Sun-Earth-Moon saddle point traces out a nearly circular path in the Earth-Moon rotating frame, as plotted in Figure 4.7. The relative inclination of the Earth-Moon orbital plane and the ecliptic plane gives the saddle point a cyclical out-of-plane component with a period commensurate to that of the Moon's synodic period and an amplitude of approximately 22,500 km.

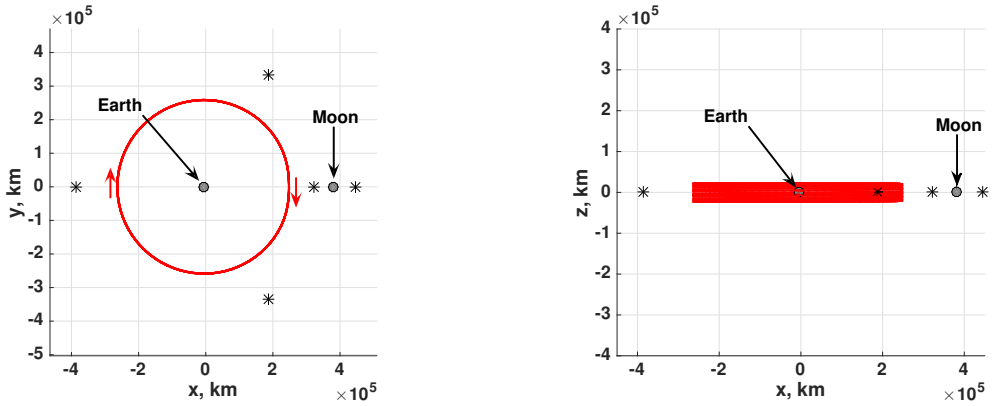

(a) xy projection

(b) xz projection

Figure 4.7.: Sun-Earth-Moon saddle point location in the Earth-Moon rotating frame over a period of 12 months

4.2.3 Saddle Point Constraint in a Multiple Shooting Algorithm

As the saddle point is defined as a gravitational equilibrium point, it is located by identifying a point in space where the acceleration vector tends to zero. In the Sun-Earth-Moon BC4BP, the acceleration vector at a point $\vec{r}_4$ in space is given by

$$\vec{A} = -\frac{(1/k-\mu)}{r_{1,4}^3}\vec{r}_{1,4} - \frac{(\mu-\nu)}{r_{2,4}^3}\vec{r}_{2,4} - \frac{\nu}{r_{3,4}^3}\vec{r}_{3,4}, \tag{4.3}$$

where the quantities μ, ν, k, and vectors $\vec{r}_{i,4}$ are consistent with the definitions supplied in Section 2.2. Note that this equation is very similar to the BC4BP EOMs given in equations (2.62) - (2.64). A constraint to collocate $\vec{r}_4$ and the saddle point is, therefore, written more compactly in terms of Ω, the BC4BP pseudo-potential, as

$$\vec{A} = \begin{Bmatrix} \Omega_x \\ \Omega_y \\ \Omega_z \end{Bmatrix} - \begin{Bmatrix} k^2 x + k^2(1/k - \mu) \\ k^2 y \\ 0 \end{Bmatrix} = \vec{0}. \tag{4.4}$$

Let $\vec{q}_i = \{\vec{\rho}_i, \vec{v}_i\}$ represent a node in a discretized trajectory. To employ this constraint function in a targeting algorithm, the partial derivatives of $\vec{A}$ with respect to the different design variables are required. These design variables consist of node states $\vec{q}_i$, integration times τ_i, and epoch times T_i. The acceleration $\vec{A}$ is an explicit function of the node position $\vec{\rho}_i$ and the primary positions $\vec{r}_1$, $\vec{r}_2$, and $\vec{r}_3$, thus it is expressed as

$$\vec{A} = \vec{A}\left(\vec{\rho}_i,\, \left\{\vec{r}_k(T_i),\ k = 1,2,3\right\}\right). \tag{4.5}$$

First, consider the partial derivative of $\vec{A}$ with respect to node position:

$$\frac{\partial \vec{A}}{\partial \vec{\rho}_j} = \begin{cases} \mathbf{0}_{3\times 3} & j \neq i \\ \mathbf{Q} & j = i \end{cases}, \qquad \mathbf{Q} = \begin{bmatrix} \Omega_{xx} - k^2 & \Omega_{xy} & \Omega_{xz} \\ \Omega_{xy} & \Omega_{yy} - k^2 & \Omega_{yz} \\ \Omega_{xz} & \Omega_{yz} & \Omega_{zz} \end{bmatrix} \tag{4.6}$$

These derivatives are derived to form the linear $\mathbf{A}$ matrix and are listed in Appendix B.2. Next, consider the partial derivatives of $\vec{A}$ with respect to node velocities $\dot{\vec{\rho}}_i$. Because the velocities do not appear in $\vec{A}$, these partials all evaluate to zero. Similarly, the partial derivatives of $\vec{A}$ with respect to time-of-flight τ are zero:

$$\frac{\partial}{\partial \tau_i}\left[\vec{A}\left(\vec{\rho}_i, \left\{\vec{r}_k(T_i),\ k = 1,2,3\right\}\right)\right] = \frac{\partial \vec{A}}{\partial \vec{\rho}_i}\frac{\mathrm{d}\vec{\rho}_i}{\mathrm{d}\tau_i} + \sum_{k=1}^{3}\frac{\partial \vec{A}}{\partial \vec{r}_k}\frac{\mathrm{d}\vec{r}_k}{\mathrm{d}\tau_i} = \vec{0}. \tag{4.7}$$

Recall that $\vec{A}$ is evaluated at a node state that is chosen independently of all previous and subsequent node states and times-of-flight, thus $\vec{\rho}_i$ is constant. Additionally, as

the primary positions $\vec{r}_k$ are functions of only epoch time T_i, the derivative of $\vec{r}_k$ with respect to τ_i evaluates to zero as well.

Finally, consider the derivative of $\vec{A}$ with respect to epoch time:

$$\frac{\partial}{\partial T_i}\left[\vec{A}\left(\vec{\rho}_i, \left\{\vec{r}_k(T_i),\ k=1,2,3\right\}\right)\right] = \frac{\partial \vec{A}}{\partial \vec{\rho}_i}\frac{\mathrm{d}\vec{\rho}_i}{\mathrm{d}T_i} + \sum_{k=1}^{3}\frac{\partial \vec{A}}{\partial \vec{r}_k}\frac{\mathrm{d}\vec{r}_k}{\mathrm{d}T_i}\,. \tag{4.8}$$

The derivative of $\vec{\rho}_i$ with respect to T_i is once again zero because $\vec{\rho}_i$ is fixed, but the derivative of $\vec{r}_k$ is nonzero. This quantity is the velocity of each primary, $\vec{v}_k$; these velocities are given in equations (2.67) - (2.69). The derivative of $\vec{A}$ with respect to $\vec{r}_k$ is given by the matrix $\mathbf{P}_k$:

$$\mathbf{P}_k = \begin{bmatrix} \dfrac{\partial \ddot{x}}{\partial x_k} & \dfrac{\partial \ddot{x}}{\partial y_k} & \dfrac{\partial \ddot{x}}{\partial z_k} \\ \dfrac{\partial \ddot{y}}{\partial x_k} & \dfrac{\partial \ddot{y}}{\partial y_k} & \dfrac{\partial \ddot{y}}{\partial z_k} \\ \dfrac{\partial \ddot{z}}{\partial x_k} & \dfrac{\partial \ddot{z}}{\partial y_k} & \dfrac{\partial \ddot{z}}{\partial z_k} \end{bmatrix}. \tag{4.9}$$

The elements of $\mathbf{P}_k$ are similar to the second derivatives of the pseudo-potential, Ω_{ab}, and are listed in Appendix B.3. Rewriting equation (4.8) in terms of these quantities yields

$$\frac{\partial \vec{A}}{\partial T_i} = \sum_{k=1}^{3}\mathbf{P}_k\vec{v}_k. \tag{4.10}$$

Note that P_1 is fixed in the rotating frame, thus $\vec{v}_1 = \vec{0}$ and only P_2 and P_3 contribute to $\frac{\partial \vec{A}}{\partial T_i}$. Within a multiple shooting process, a node is constrained to coincide with the saddle point by enforcing equation (4.4) evaluated at the node location, and the partial derivatives obtained from equations (4.6) and (4.10) are included in the Jacobian matrix. Experimentation reveals that this constraint is robust to reasonable perturbations from the true saddle point location, i.e., an initial guess in the vicinity of the saddle point converges rapidly.

4.3 LPF Primary Orbit Departure Arcs

Invariant manifold arcs supply low-cost transfer solutions to and from periodic and quasi-periodic orbits in the CR3BP and are useful in this investigation as departure options from the LPF primary mission orbit. Manifold arcs associated with quasi-periodic orbits that possess approximately periodic revolutions, like the QHO discussed in Section 4.1, are computed in a similar fashion as manifold arcs for periodic orbits [32]. To compute the stable and unstable manifold arcs from a point $\vec{q}_0$ on the quasi-periodic orbit (QPO), first propagate the motion from $\vec{q}_0$ for one revolution of the QPO, i.e. for time T, to point $\vec{q}_1$. Assuming the motion is approximately periodic and the distance between $\vec{q}_0$ and $\vec{q}_1$ is small, the state transition matrix associated with the propagation is analogous to the monodromy matrix associated with a periodic orbit and offers an approximation to the local dynamics. Thus, Unstable manifold arcs are computed by stepping some small distance ϵ from $\vec{q}_0$ in the direction of an unstable eigenvector and stable manifold arcs are computed similarly.

Unstable manifold arcs that depart the QHO toward the Earth are initialized and propagated to the xz-plane in the Sun-Earth system. Each of these arcs, plotted in magenta in Figure 4.8, departs the QHO at an epoch of April 18, 2016 at 00:00:00.000 UTC, consistent with the end date of a 200 day primary mission following a nominal launch on November 1, 2016. This epoch determines the location of the Moon when each manifold arc reaches the Earth-Moon vicinity. Some of the manifold arcs pass near the saddle point and may offer one of the two required saddle point encounters.

4.4 Patched 3BP To Achieve Multiple Saddle Point Encounters

Regardless of whether a saddle point encounter is achievable on an unstable manifold between the L_1 QHO and Earth vicinity, at least one additional saddle point encounter is required. To achieve additional encounters, periodic motion in the Earth-Moon vicinity is explored via the Earth-Moon CR3BP. Candidate arcs include the planar Lyapunov and resonant families as well as the 3D halo, vertical, and axial

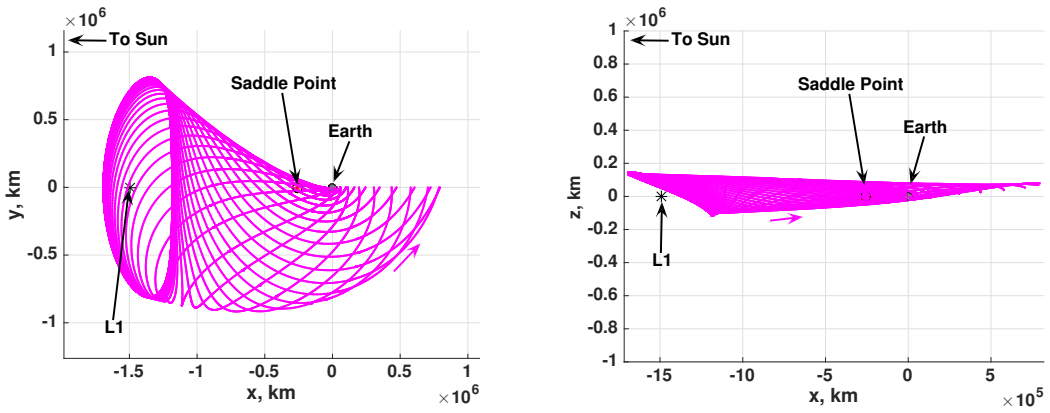

(a) xy-Projection (b) xz-Projection

Figure 4.8.: Unstable manifold arcs depart a Sun-Earth L_1 quasi-halo

families. To be a viable candidate, a periodic orbit in the Earth-Moon CR3BP must pass near the saddle point and possess a Jacobi constant value similar to the Jacobi value associated with the Sun-Earth quasi-halo manifold arcs. A candidate arc that meets these requirements is then included in a trajectory design for the LPF extended mission.

4.4.1 Energy Comparison Between Sun-Earth and Earth-Moon Motion

Due to the low propellant budget available for the extended mission, only very low-cost transfer options are considered. Accordingly, a spacecraft path that transitions from a Sun-Earth quasi-halo manifold arc to an Earth-Moon periodic orbit should employ as small a maneuver as possible. As the difference in Jacobi constant values between arcs is related to the minimum possible maneuver magnitude, Earth-Moon periodic orbits with similar Jacobi constant values to the Sun-Earth manifold arcs are sought.

To compare the Sun-Earth quasi-halo manifold arcs and motion in the Earth-Moon system, the Sun-Earth arcs are transformed into Earth-Moon rotating coordinates. For an initial analysis, consider only the end-points of the manifold arcs, all of which

lie on the Sun-Earth line, i.e., the x-axis in the Sun-Earth rotating frame. In the Sun-Earth CR3BP, each manifold has a Jacobi constant value identical to the energy associated with the quasi-halo orbit (QHO). However, when the points are represented in the Earth-Moon CR3BP, the Jacobi values associated with the points vary. To illustrate this fact, the energy of the manifold arcs in the Earth-Moon CR3BP is plotted against the Sun-Earth x-coordinate in Figure 4.9(a). Although some of the manifold arcs that pass very near the Earth (with $x \approx 0$) have Jacobi constant values much less than 1, the plotted data is filtered to show only energies consistent with typical Earth-Moon periodic motion, i.e. $1 \leq C \leq 3.5$. As a general rule, manifold arcs that intersect the Sun-Earth line farther from Earth possess larger Jacobi constant values, or less energy.

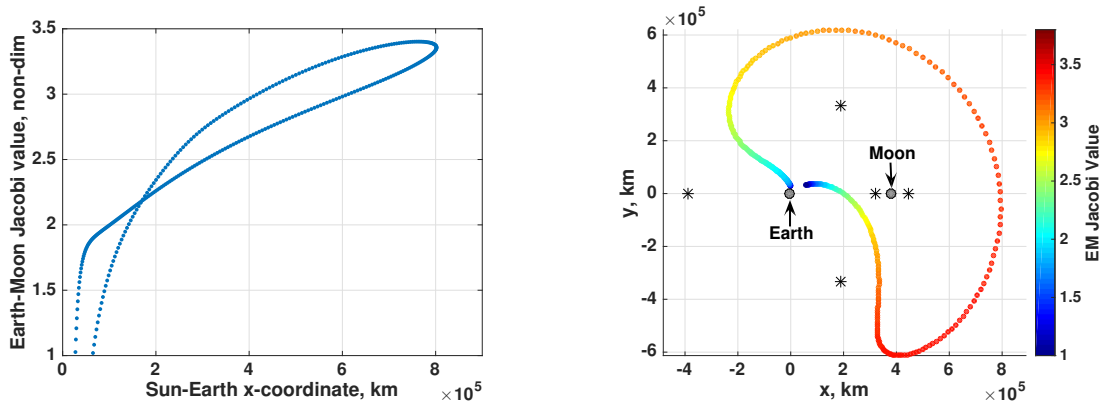

(a) Earth-Moon Energy vs Sun-Earth x-Coordinate

(b) Transformed points in the Earth-Moon rotating frame, colored by Earth-Moon energy

Figure 4.9.: Representations of the Earth-Moon Jacobi constant value associated with the end-points of the Sun-Earth manifold arcs

Further insight is available by plotting the Sun-Earth manifold end-points in the Earth-Moon rotating frame. Though these points lie on a line in the Sun-Earth rotating frame, the arrival epoch associated with each point varies based on the time-of-flight along the manifold arc, thus the linear geometry does not persist after a transformation to Earth-Moon rotating coordinates, as illustrated in Figure 4.9(b).

Each manifold end-point is projected into the Earth-Moon xy-plane and colored by its Earth-Moon Jacobi constant value. Points with lower energy, colored red, lie exterior to the Earth-Moon system, while points with higher energy, colored blue and green, exist closer to the primaries. This relationship between energy and position limits the types of transfers available when linking the Sun-Earth manifold arcs to natural motion in the Earth-Moon system. At the lower end of the energy spectrum (red colors), the zero velocity surfaces close around the primaries and separate the exterior and interior regions. Subsequently, an Earth-Moon orbit that matches these energy values cannot transit from the manifold arc to the interior of the system, where the saddle point is located. Arcs with higher energy values, represented by orange, yellow, green, and blue colors, are not restricted by the ZVCs in this way.

Incorporating larger portions of the manifold arcs supplies additional states on the map. While Figure 4.9(b) illustrates only the final state on each manifold arc, the representations in Figure 4.10 plot the final 1-day and 3-day segment on each manifold arc in Earth-Moon rotating coordinates. The points are once again colored by their Earth-Moon Jacobi constant value. Though the points spread from the single-epoch distribution, the same general trends persist. Points with low energy values lie outside the system, and points with higher energies span the interior of the system. Thus, low-cost transfers from the lowest energy manifold arc segments to the saddle point are not feasible and higher energy options are leveraged to achieve saddle point encounters.

4.4.2 Saddle Point Encounters in the Earth-Moon System

By comparing motion in the Earth-Moon system to the saddle point location time history represented in Earth-Moon rotating coordinates, a preliminary screening of candidate orbits is conducted. Four common libration point orbit families are plotted in Figure 4.11; each family member is colored by its Jacobi constant value for comparison with the range of energies available from the Sun-Earth manifold arcs.

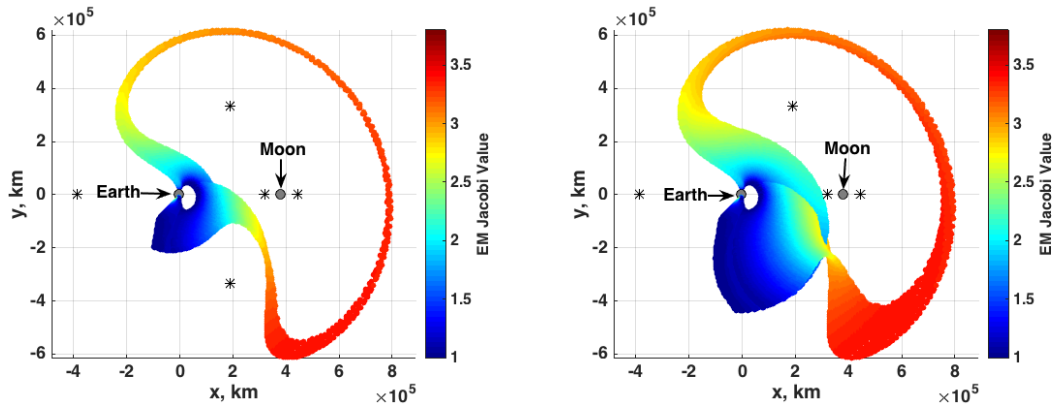

(a) Final 1 Day on Manifold Arcs

(b) Final 3 Days on Manifold Arcs

Figure 4.10.: Final sections of the Sun-Earth manifold arc states transformed into Earth-Moon rotating coordinates and colored by Earth-Moon Jacobi constant value

These families are filtered such that only orbits with Jacobi constant values between 1 and 3.8 are included in the plots. The saddle point is plotted in magenta in each frame. Libration point orbits that do not pass through the saddle point path cannot provide saddle point encounters. Many orbits within the L_1 and L_3 Lyapunov families intersect the saddle point but the L_2 family does not, as illustrated in Figure 4.11(a). Similarly, a small selection of the L_3 northern halo family (Figure 4.11(b)) encounters the saddle point path, but the L_1 and L_2 families have smaller amplitudes and do not cross the saddle point path. A few members of the L_3 northern axial family also encounter the saddle point; again, the L_1 and L_2 families remain separated from the saddle point vicinity. Finally, the vertical orbit families, depicted in Figure 4.11(d), provide no saddle point encounters. Many other families of periodic motion exist in the CR3BP, but many are disqualified as candidates for the extended mission for similar reasons. The Low Prograde Orbits and Distant Prograde Orbits, for example, exist between the L_1 and L_2 points and do not pass through the saddle point path [26]. Similarly, the butterfly family remains in the vicinity of the Moon and does not offer additional saddle point encounters [39].

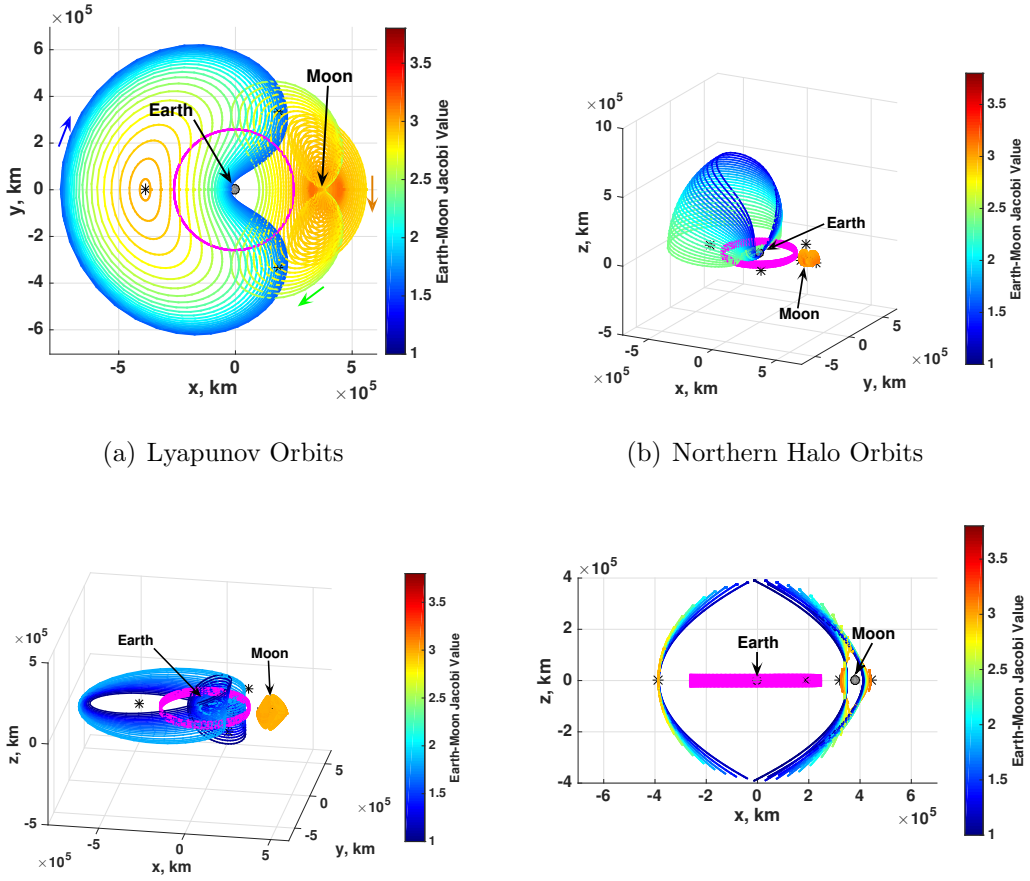

(a) Lyapunov Orbits

(b) Northern Halo Orbits

(c) Northern Axial Orbits

(d) Vertical Orbits

Figure 4.11.: Selections of Earth-Moon Libration point orbit families plotted in Earth-Moon rotating coordinates and colored by Jacobi constant value. A 12-month saddle point location history is plotted in magenta

4.4.3 Resonance with the Saddle Point

Though a selection of libration point orbits pass through the saddle point path, multiple encounters with the saddle point are required. Recall that the Sun-Earth-Moon saddle point oscillates about the fixed Sun-Earth saddle point with a period equal to the synodic period of the Moon. Accordingly, an orbit in resonance with this period is ideal, though not necessary, to deliver multiple saddle point encounters as no phase adjustments are required. Libration point orbits with appropriate periods

may be chosen, as well as more traditional resonant orbits derived from conic motion in the two body problem. A selection of planar interior and exterior resonant orbits are plotted in Earth-Moon rotating coordinates in Figure 4.12, again colored by their Earth-Moon Jacobi constant value and filtered to exclude orbits with Jacobi values less than 1.0 or greater than 3.8. Many of the displayed resonant orbits intersect the

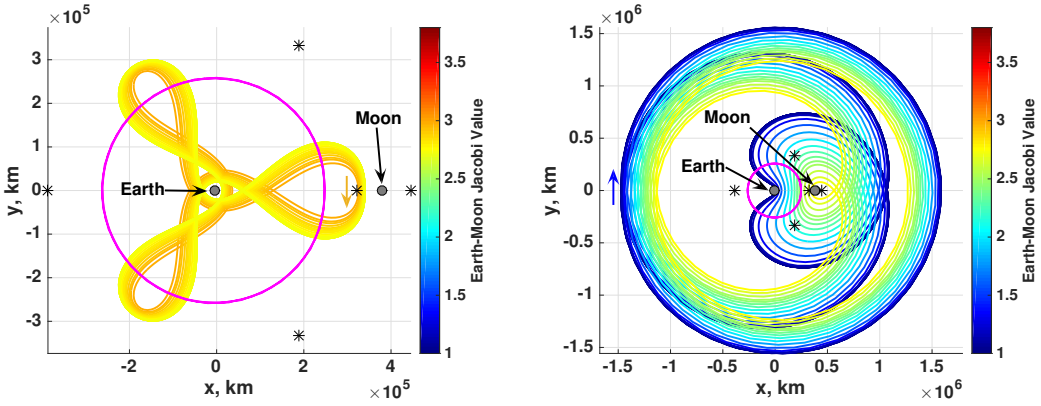

(a) 3:1 Resonant Orbit Family

(b) 1:3 Resonant Orbit Family

Figure 4.12.: Selection of planar Earth-Moon resonant orbits plotted in the Earth-Moon rotating frame with the saddle point (magenta)

saddle point arc. However, these resonant orbits possess periods commensurate with the *sidereal* period of the moon, not the synodic period. To evaluate the relationship between the period of the resonant orbits and the lunar synodic month, consider the comparison illustrated in Figure 4.13. Resonant frequencies of the synodic month are depicted as black, dashed, vertical lines, each with a label representing frequency. For example, the "p:1" line represents a period that matches the synodic period, and the "p:2" line represents a period twice as large as the synodic period. Near each vertical black line is a gray, dashed, vertical line that identifies the corresponding sidereal frequency. That is, the gray line near the black p:2 line represents a period twice as large as the sidereal period of the Moon, etc. Although the period of a p:q resonant orbit in an inertial frame is equal to $(q/p)\mathbb{P}_{\mathbb{C},sidereal}$, the period in the rotating frame

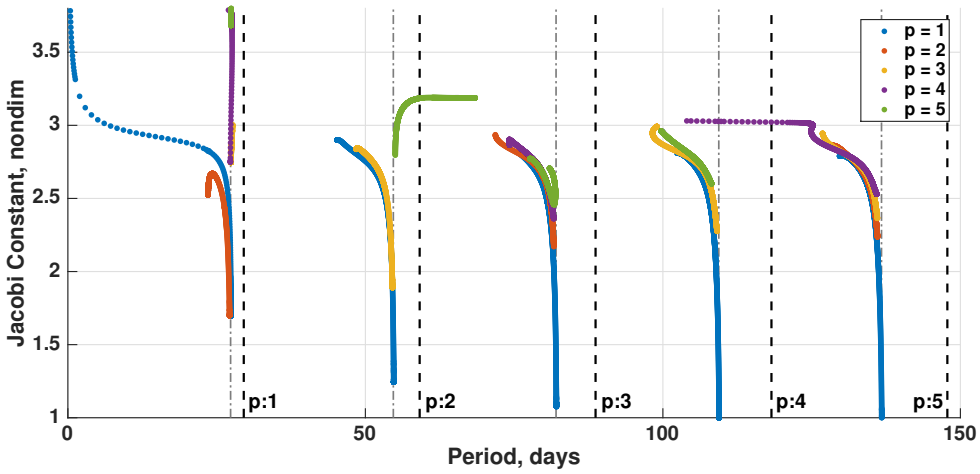

Figure 4.13.: A comparison of the energy and period of Earth-Moon resonant orbit families

is simply $q\mathbb{P}_{\mathbb{C}_{,sidereal}}$. This fact is reflected in the plot as each family of resonant orbits lies near one of the gray lines that represent integer multiples of the lunar sidereal period. Thus, the value of q is determined by the proximity of the family of resonant orbits to the gray, dashed lines. The color of each family identifies the value of p.

The families of resonant orbits do not generally possess periods commensurate with the lunar synodic month. However, several family evolutions, namely the 5:2 and 4:5 families, possess periods that include an integer multiple of the Moon's synodic period. These orbits, if they intersect the saddle point, repeatedly intersect the point at the same location in the Earth-Moon rotating frame, thus delivering the desired multiple saddle point encounters. Upon inspection, the 4:5 family member remains exterior to the Earth-Moon system and does not pass through the saddle point path as the orbits in Figure 4.12(b) do. The 5:2 family member, on the other hand, does pass through the saddle point path. However, this orbit is interior to the Earth-Moon system and possesses a Jacobi value of approximately 3.1856, thus the gateways between the exterior and interior system are closed. As the manifold arcs with similar

Jacobi constant values lie outside the system, a sizable maneuver is required to open the gateways and achieve a transfer to the 5:2 orbit.

Although the periodic orbits identified to be resonant with the Moon's synodic period are disqualified as candidates for the extended mission design, other orbits with periods *near* the synodic month may be useful; The 1:1, 2:1, and 3:1 families all possess family members with periods very near the synodic month and, additionally, have Jacobi constant values low enough to supply potentially free connections to the Sun-Earth manifold arcs. The 3:1 family, plotted in Figure 4.12(a), demonstrates the multi-lobed geometry common to these solutions. Many family members pass through the saddle point path, represented by a magenta arc, and may be adjusted via small maneuvers to make up for the noncommensurability of the orbital period and synodic month. If low-cost links are identified between these orbits and the Sun-Earth manifold arcs, they may offer the required multiple saddle point flybys.

A similar analysis is conducted for the libration point families identified to pass through the saddle point path. The L_3 Lyapunov, halo, and axial families all possess orbital periods near the sidereal period of the Moon, as illustrated in Figure 4.14. The L_1 Lyapunov family, on the other hand, spans a wide range of periods, including

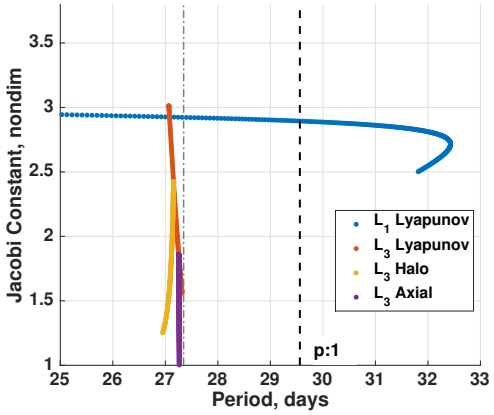

Figure 4.14.: Orbital period compared to Jacobi constant value for libration point orbit families that intersect the saddle point path

the lunar synodic period. The Lyapunov orbit associated with this period has an Jacobi value below 3 and is, thus, accessible from the Sun-Earth manifold arcs. Again, maneuvers may be implemented to adjust the motion of the other solutions to achieve multiple saddle point encounters. Additionally, many other oscillatory solutions exist in the CR3BP. A diverse set of 3D resonant orbits, for example, supply further options for motion that encounters the saddle point. Quasi-periodic solutions in the vicinity of periodic motion also increase the number of options.

4.4.4 Link Sun-Earth and Earth-Moon Segments

Once candidate Earth-Moon orbits are identified with the appropriate energy values, saddle point encounters, and, perhaps, a near resonance with the saddle point period, links between the Sun-Earth manifold arcs and Earth-Moon orbits are located. These paths must intersect in position and time, and, to minimize cost, should also possess similar velocities. Links between segments are identified by combining the plots from Figures 4.9 and 4.12 to construct a higher-dimensional Poincaré map. As an example, consider the overlaid plots of the Sun-Earth manifold arcs and Earth-Moon 1:2 resonant orbit family depicted in Figure 4.15. A hyperplane is chosen in the Sun-Earth rotating frame such that manifold arcs are captured as they cross the xz-plane, consistent with the manifold states depicted in Figure 4.9. These states are transformed into Earth-Moon rotating coordinates and projected onto the xy-plane; out-of-plane components do exist, but have relatively small magnitudes, thus the planar projection provides a reasonable estimate of the true motion. Vectors from each point indicate the direction and magnitude of the manifold velocity in the xy-plane. As in Figure 4.9, each manifold point is colored by its Earth-Moon Jacobi constant value, as are Earth-Moon orbits. Planar families, such as the Lyapunov and resonant orbits, are well-suited for this mapping procedure as they require no projection into the plane. However, three dimensional orbits with significant out-of-plane components are not represented accurately.

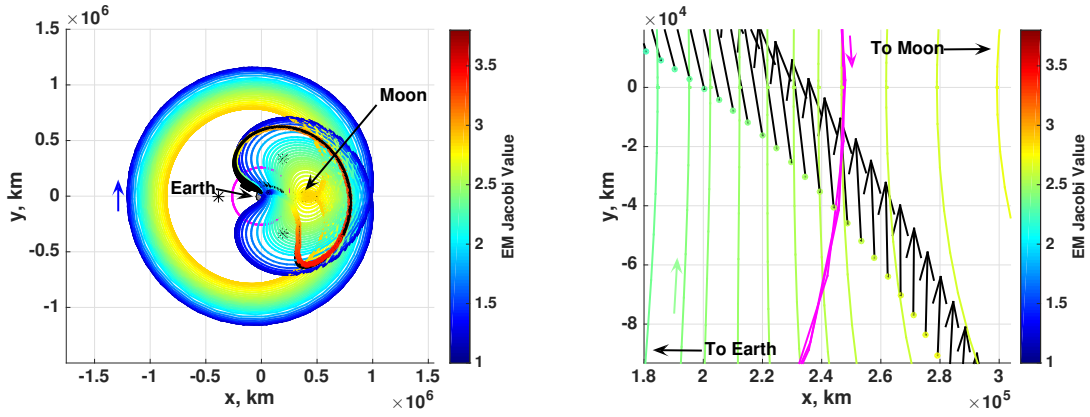

(a) Full View

(b) Zoomed-In View

Figure 4.15.: Comparison of Earth-Moon 1:2 resonant orbit family and Sun-Earth manifold arcs projected into Earth-Moon rotating coordinates at a specific epoch. The saddle point is represented by a magenta arc

A potential low-cost link between a manifold arc and resonant orbit is identified by locating a manifold arc state with a velocity vector tangent to an Earth-Moon orbit and a similar Jacobi constant value. By zooming in on the region between the Earth and the Moon, as in Figure 4.15(b), a number of candidate links are located. The resonant orbits visible in this zoomed-in view are nearly parallel to the manifold velocity vectors. Additionally, the Jacobi constant value of the resonant orbits and manifold states are approximately the same. Therefore, the velocity magnitudes of the two types of motion are similar and a low-cost link between the two is feasible. As a final criteria, the resonant orbit selected to link with a manifold arc should pass through the saddle point path, plotted in magenta; the resonant orbits on the right-hand-side of Figure 4.15(b) do not pass through the saddle point and are not viable candidates for the extended mission design. However, the light green resonant orbit arcs in the center of the plot are nearly tangent to the saddle point path. Accordingly, the 2:1 resonant orbit family supplies several promising candidate arcs for the extended mission design.

This analysis is repeated for the 1:1, 2:1, and 3:1 resonant orbit families, as well as for the L_1 Lyapunov and L_3 Lyapunov, halo, and axial families that possess periods near the lunar synodic period. The 3:1 family, depicted in Figure 4.16(a), is far from tangent to the manifold arc velocity directions. Similarly, the L_1 Lyapunov family includes orbits tangent to the manifold velocity vectors, but at significantly different Jacobi constant values. In either case, significant maneuvers are required to link the two arcs, thus these families do not supply trajectories capable of encountering the saddle point at a low cost.

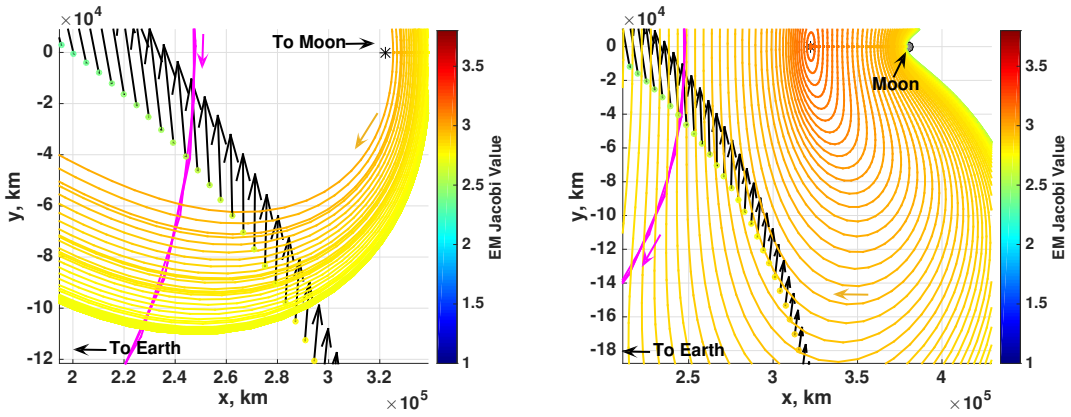

(a) 3:1 Resonant Family

(b) L_1 Lyapunov Family

Figure 4.16.: Search for links between additional Earth-Moon families and the Sun-Earth L_1 QHO unstable manifold arcs; velocity vector directions are not tangent to family members with similar energy values

As periodic orbits with frequencies near the lunar synodic frequency are not accessible via low-cost maneuvers, other periodic orbits are considered. As established above, the 1:2 resonant orbit family offers potential low-cost trajectory options that intersect the saddle point path multiple times. The 1:3, 1:4, 2:3, and 3:4 resonant families possess similar geometries and likewise offer feasible options for the extended mission. To illustrate the process of constructing a patched three-body transfer, consider linking a manifold arc to an Earth-Moon 1:2 resonant orbit. A low-cost transfer

is selected by locating a manifold arc on the map that lies near a resonant orbit with a similar color (Jacobi constant value) and has a velocity vector that is approximately tangent to the resonant orbit. The first segment consists of the Sun-Earth L_1 quasi-halo unstable manifold arc propagated to the map crossing. The second segment consists of several revolutions of the Earth-Moon resonant orbit, propagated from a state near the manifold map crossing. An initial estimate of an end-to-end transfer is visualized by transforming each segment into the same reference frame; Figure 4.17 supplies representations of the transfer in the Sun-Earth and Earth-Moon coordinate systems. In both coordinate systems, the quasi-halo manifold arc is plotted in blue,

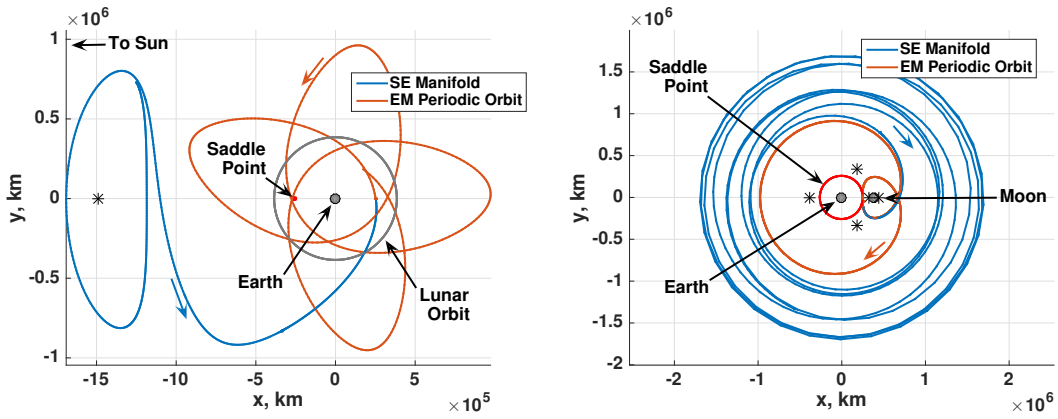

(a) Sun-Earth Rotating Coordinates

(b) Earth-Moon Rotating Coordinates

Figure 4.17.: A trajectory constructed from a Sun-Earth L_1 quasi-halo unstable manifold arc and an Earth-Moon 1:2 resonant orbit, depicted in two coordinate frames

the resonant orbit in orange, and the saddle point in red. The tangential encounter with the saddle point path is clearly visible in the Earth-Moon representation as the manifold and periodic orbit transit about the lobe encompassing the lunar region. This tangential flight mitigates the difference between the resonant orbit period and the saddle point period and facilitates multiple saddle encounters, as seen in the Sun-Earth representation. The transition from one segment to the next appears smooth in these representations, although a small position and velocity discontinuity exists

between the segments. This discontinuity is later corrected via a multiple-shooting process.

Other resonant orbits supply similar transfers. The 2:3 resonant family, for example, is leveraged to construct the transfer depicted in Figure 4.18. Once again,

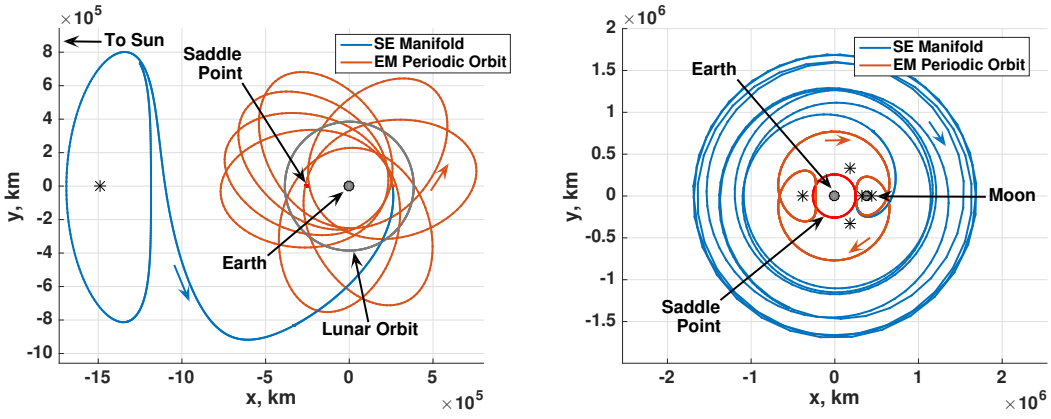

(a) Sun-Earth Rotating Coordinates

(b) Earth-Moon Rotating Coordinates

Figure 4.18.: A trajectory constructed from a Sun-Earth L_1 quasi-halo unstable manifold arc and an Earth-Moon 2:3 resonant orbit, depicted in two coordinate frames

tangential encounters with the saddle point path in the Earth-Moon rotating frame facilitate the saddle point encounters visible in the Sun-Earth rotating frame. These tangential encounters are typical of exterior resonant orbits that posses low Jacobi constant values, or high energy values. In general, resonant orbits with higher Jacobi values are desirable because they remain closer to the Earth-Moon system than orbits with higher energy (i.e., lower Jacobi values) and are less perturbed by solar gravity when transitioned to higher-fidelity models. However, as discussed previously, Earth-Moon orbits with Jacobi constant values above the L_1 or L_2 gateway energies are generally inaccessible from the low-energy manifold arcs as they are separated by the zero velocity surface. Accordingly, orbits that minimize energy within these limits, i.e., orbits in the yellow-orange color range, or 2.8 - 3.17 Jacobi constant value range, are sought; dark blue periodic orbits, those with Jacobi values below 2, are

not leveraged for this analysis because their motion strays far from the Earth-Moon vicinity and is strongly perturbed by the Sun.

4.4.5 Corrections Process

Patched three-body motion is corrected in a model that includes, at minimum, all primary bodies from the three-body systems. In this investigation, the Sun-Earth-Moon BC4BP is employed for this purpose. The transfer is discretized into a series of nodes and passed to a multiple shooting algorithm. The multiple shooting process constraints position and time continuity by default, and velocity continuity is enforced at all nodes except for nodes that are permitted to have impulsive maneuvers. Additional constraints are applied to nodes near the saddle point to ensure they intersect the exact location of the Sun-Earth-Moon saddle point.

An initial corrected transfer generally requires a maneuver or series of maneuvers that exceed the allowable mission Δv budget. A constraint on total Δv is applied to reduce the maneuver costs to a local minimum.

4.5 Natural Extension of Sun-Earth Manifold Arcs in BC4BP

As an alternative to the patched three-body problem, i.e., linking arcs from the Sun-Earth and Earth-Moon CR3BP, natural motion in the BC4BP is leveraged to supply multiple saddle point encounters. To obtain such natural motion, a series of steps are completed. First, unstable manifold arcs are propagated from the Sun-Earth L_1 quasi-halo to the x-axis in the rotating Sun-Earth frame, as demonstrated in the patched three-body method. Next, each manifold arc is combined with a revolution of the quasi-halo and discretized. A multiple shooting algorithm is employed to enforce position, velocity, and time continuity along the arc. Finally, the manifold arc is propagated from the x-axis for some time in the Sun-Earth-Moon BC4BP. The resulting geometries are loosely grouped into four categories: single-pass arcs, double-pass arcs, partially captured arcs, and captured arcs. Single-pass arcs, plotted

in Figure 4.19(a), perform a single Earth flyby and depart the system. Though the arcs illustrated here depart in the direction of L_1, other options exist that exit toward L_2. These arcs do not exhibit multiple saddle point encounters and are not feasible options for the LPF extended mission trajectory. Double-pass arcs are characterized

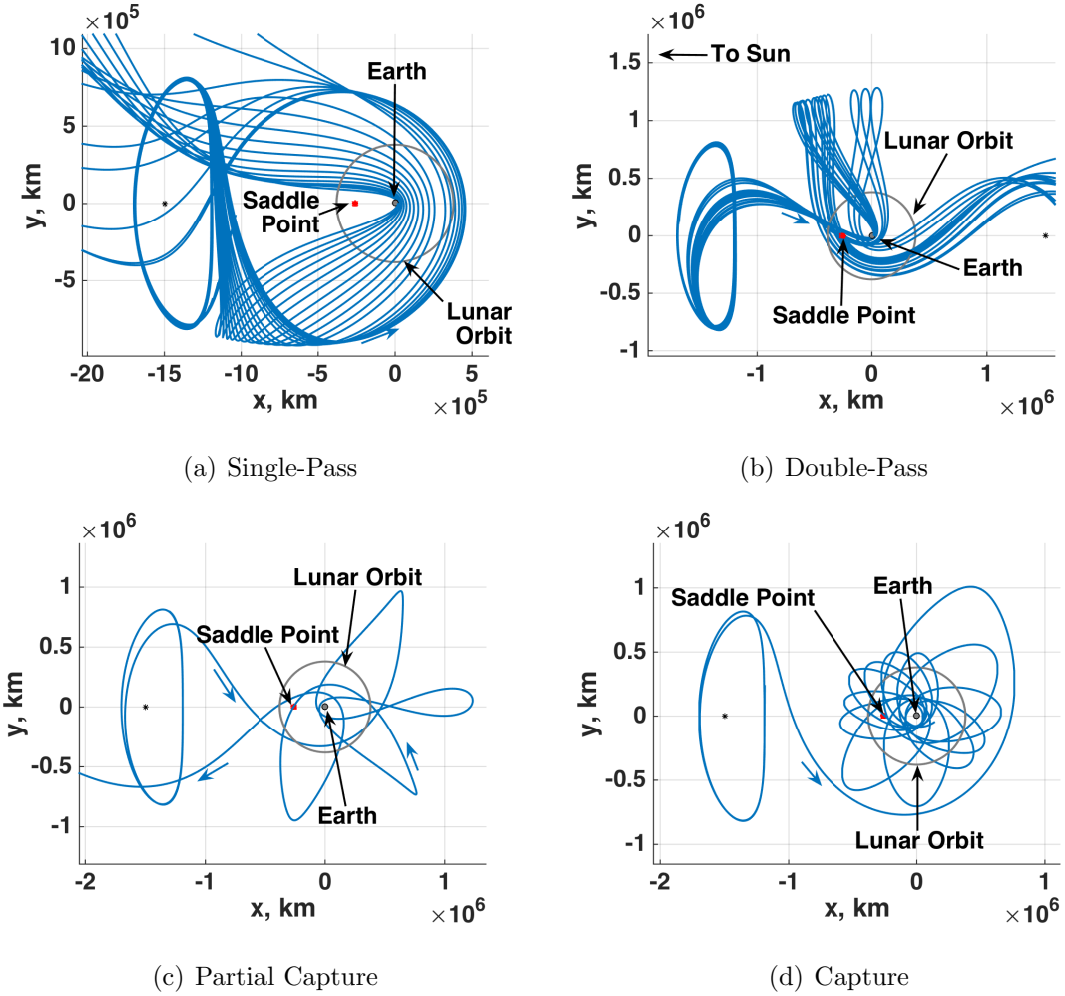

(a) Single-Pass

(b) Double-Pass

(c) Partial Capture

(d) Capture

Figure 4.19.: General categories of natural motion flowing from the unstable manifold arcs

by two Earth flybys and are illustrated in Figure 4.19(b). These arcs *do* exhibit multiple saddle point encounters and may be corrected to achieve the desired pass distance. Partially captured arcs, as in Figure 4.19(c), perform multiple Earth flybys

but eventually depart the vicinity of the saddle point. Similar to the double-pass arcs, the multi-pass motion may be adjusted to achieve the desired saddle point encounters via a corrections process. Finally, captured arcs, illustrated in Figure 4.19(d), remain in the vicinity of the Earth and saddle point for much longer than the desired two-year extended mission timeline and may include many saddle point encounters. This captured motion generally leverages a close lunar flyby to decrease the trajectory energy.

Although natural motion in the BC4BP does not require adjustments to ensure position, velocity, and time continuity, some corrections are required to ensure multiple saddle point encounters within the desired 100 km range. Accordingly, the transfer design is discretized and nodes near the saddle point are constrained to intersect the saddle point location. Impulsive maneuvers are permitted at one or more nodes along the transfer to provide opportunities for the corrector to adjust the transfer geometry to satisfy the new constraints. Finally, a constraint on the total Δv is applied to reduce the cost of the transfer.

5. RESULTS

Multiple methods to construct an end to end transfer for the LISA Pathfinder extended mission have been developed and are applied. First, arcs from the Sun-Earth and Earth-Moon CR3BP systems are patched together in the Sun-Earth-Moon BC4BP and a corrections process is applied to mitigate discontinuities and satisfy mission constraints. A second method leverages the natural evolution of the the unstable quasi-halo manifold arcs in the Sun-Earth-Moon BC4BP to construct trajectories that encounter the saddle point. Several trajectories are designed via both methods and compared to the mission constraints. Finally, the designs are transitioned to an ephemeris model to validate the BC4BP results.

5.1 Patched 3BP Motion

By following the procedure described in Section 4.4.4, an initial estimate for a end-to-end trajectory is constructed from a Sun-Earth unstable manifold arc and an Earth-Moon periodic orbit. The Earth-Moon orbit is transformed into Sun-Earth rotating coordinates and linked with the manifold arc, as depicted in Figures 4.17(a) and 4.18(a). Additionally, one revolution about the quasi-halo orbit is incorporated into the design; the inclusion of this arc preserves the original quasi-halo during the corrections process without the need for additional constraints. The design is then transformed into Sun-Earth-Moon BC4BP coordinates. Recall that the BC4BP is formulated such that the origin lies at the P_2-P_3 barycenter, B_2, and the coordinates rotate with P_1-B_2 line. Accordingly, a transformation from Sun-Earth CR3BP coordinates to Sun-Earth-Moon BC4BP coordinates requires only a shift in the x-coordinate to adjust the origin to the Earth-Moon barycenter and variable scaling to account for the change in characteristic quantities. The epoch associated with the

beginning of the departing unstable manifold arc is set to April 18, 2016 00:00:00.000 UTC, consistent with the conclusion of a 200 day LPF primary mission.

Two trajectory options are designed by leveraging motion from a 1:2 Earth-Moon resonant orbit as well as a 2:3 resonant orbit. Each design is discretized and then propagated in the Sun-Earth-Moon BC4BP. In this higher-fidelity model, the CR3BP arcs are no longer continuous; position and velocity discontinuities exist between segments, as illustrated in Figure 5.1. These discontinuities are largest and most visible in the plots near apogees on the Earth-Moon segment of the design, particularly at apogees near the Sun-Earth line, i.e., the x-axis. At these points, the spacecraft has a relatively low speed and solar gravity perturbs the Earth-Moon motion in a direction nearly orthogonal to its velocity vector. Subsequently, the Earth-Moon motion is strongly perturbed by the Sun.

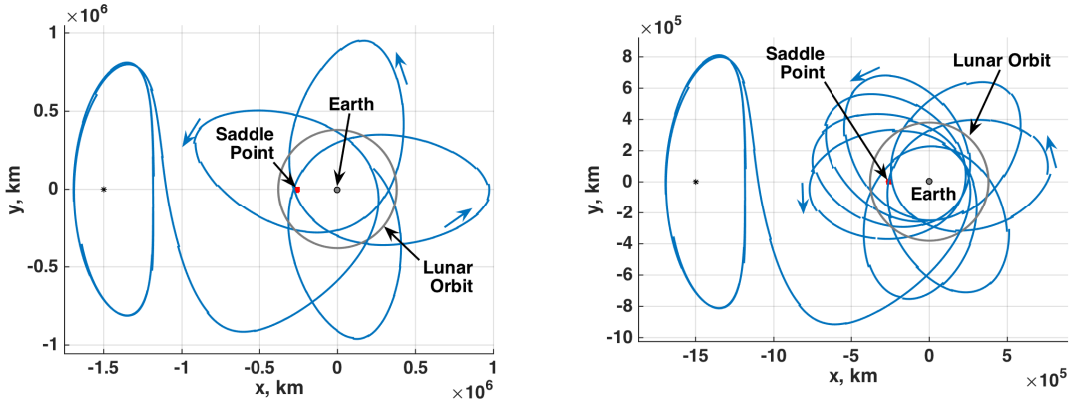

(a) 1:2 Resonant Orbit

(b) 2:3 Resonant Orbit

Figure 5.1.: A complete initial guess for a transfer, including one revolution about the quasi-halo, an unstable manifold arc, and an Earth-Moon periodic orbit, propagated from a set of discretized nodes in the Sun-Earth-Moon BC4BP

To mitigate these discontinuities and achieve a continuous transfer with some incorporated impulsive maneuvers, a multiple shooting corrections scheme is implemented within the Sun-Earth-Moon BC4BP. Velocity discontinuities, i.e., impulsive

maneuvers, are permitted at the interface between the unstable manifold arc and the resonant orbit and at apogee on the Earth-Moon arcs. A sequence of steps is implemented to converge upon a solution similar to the baseline guess. First, the trajectory is corrected for continuity in the BC4BP. Next, two constraints are added to ensure that the path intersects the saddle point location at two distinct times. Additionally, the total Δv is constrained to remain at or below the value converged upon during the initial continuity corrections process. The multiple shooting process is repeated with the new constraints to obtain a converged design that includes the required saddle point encounters. Finally, the constraint on total Δv is iteratively decreased to reduce the maneuver cost of the transfer.

To illustrate this process, consider the patched design that leverages an Earth-Moon 1:2 resonant orbit. An initial corrections process converges on a path that requires a total maneuver budget of 1308 m/s to approximately preserve the geometry of the Earth-Moon resonant orbit, as illustrated in Figure 5.2(a). Several of these

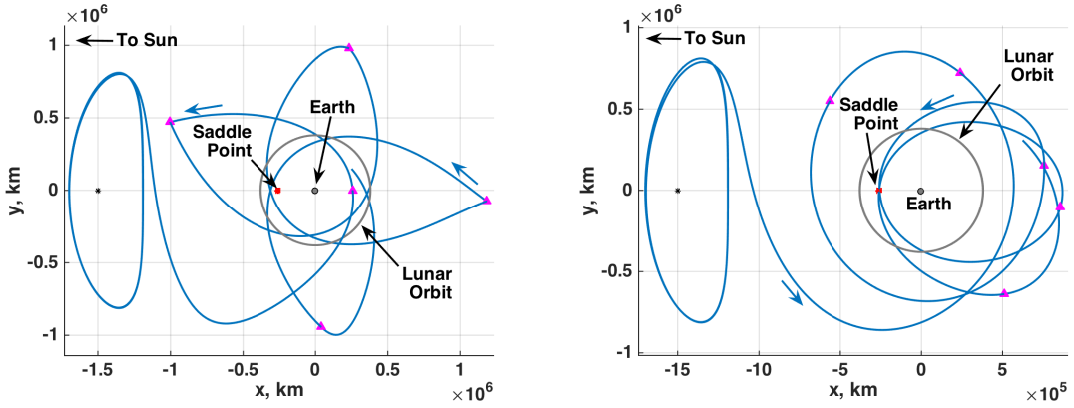

(a) Initial, Continuous Trajectory

(b) Reduced Δv Trajectory

Figure 5.2.: Two corrected transfers stemming from a patched 3BP design that leverages an Earth-Moon 1:2 resonant orbit

maneuvers, marked by magenta triangles, are clearly visible as cusps in the trajectory and occur most prominently at the apogees near the Sun-Earth line. Once the total

maneuver cost is reduced by an iterative corrections process, the geometry changes: an initial loop about the Earth-Moon system flows into a series of less eccentric loops with apogees on the dark side of the Earth. This converged solution, pictured in Figure 5.2(b), includes 278 m/s of impulsive maneuvers and flies directly through the saddle point at two distinct times. The first flyby occurs 380 days after departing the quasi-halo with an Earth-centered, inertial speed of 1534 m/s. The second saddle point encounter occurs 55 days later with a speed of 1553 m/s in the Earth-centered, inertial frame.

The same process is repeated for the patched design that leverages an Earth-Moon 2:3 resonant orbit. The initial corrections process converges on a trajectory that includes 1746 m/s of maneuvers to approximately reproduce the resonant arcs from the Earth-Moon CR3BP; this preliminary transfer is plotted in Figure 5.3(a). As with the previous example, the maneuvers at apogees near the Sun-Earth line are

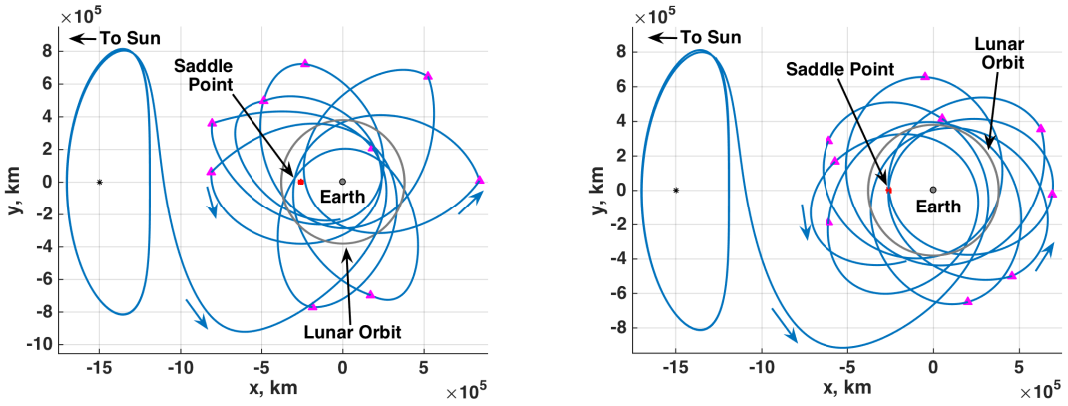

(a) Initial, Continuous Trajectory

(b) Reduced Δv Trajectory

Figure 5.3.: Two corrected transfers stemming from a patched 3BP design that leverages an Earth-Moon 2:3 resonant orbit

particularly visible as cusps in the path. After a series of corrections to reduce the total Δv, the path plotted in Figure 5.3(b) is converged upon, with a total maneuver budget of 538 m/s. The trajectory lobes near the Earth are once again less eccentric

and posses lower apogees compared to the Earth-Moon arcs. The first saddle point encounter occurs 393.5 days after departing the quasi-halo with an Earth-centered, inertial speed of 1486 m/s. A second encounter commences 40 days later with a slightly higher speed of 1519 m/s in the Earth-centered, inertial frame.

It is interesting to note that the original discontinuity between the Sun-Earth manifold arc and the Earth-Moon resonant orbits is on the order of 150 m/s. That is, the motion depicted in Figures 4.17 and 4.18 include an impulsive maneuver of about 150 m/s at the interface between the Sun-Earth and Earth-Moon motion. However, when transitioned to the higher-fidelity BC4BP, pertubations from the Moon on the Sun-Earth motion and perturbations from the Sun on the Earth-Moon motion are introduced, thus the total cost to preserve the desired geometry increases. Accordingly, even with efforts to decrease the total Δv, the cost for the patched 3BP trajectory designs exceeds the allowable Δv of 4 m/s by several orders of magnitude.

Both of the resonant orbits employed in the trajectory designs are exterior resonant orbits and are characterized by high altitude apogees. As these apogees are far from the influence of the Earth and Moon, the spacecraft path near these points is particularly sensitive to solar perturbations. Orbits that remain near the Earth-Moon system are less susceptible to solar perturbations; in fact, several authors have demonstrated low-cost transfers between libration point orbits in the Earth-Moon and Sun-Earth systems [40, 41]. Accordingly, interior resonant orbits may supply multiple saddle point encounters for a lower Δv budget. However, the interior resonant orbits are not accessible from the quasi-halo manifold arcs via low-cost maneuvers, and are, therefore, infeasible candidates for the low-cost extended mission design. Low-altitude lunar flybys may be leveraged to adjust the energy of the inbound manifold arcs, but the tools necessary for such a design remain an area of future study.

5.2 Natural BC4BP Motion

Employing natural motion in the BC4BP avoids the perturbation issues that plague the transitioned CR3BP resonant orbit arcs. As a number of different geometries exist, illustrated in Figure 4.19, many trajectory options are possible. Trajectory options stemming from the double-pass and loose capture geometries are evaluated and corrected. Additionally, fully captured arcs are considered as potential low-cost options for future work.

5.2.1 Double-Pass Geometry

Consider first the double-pass geometry; solutions of this type are characterized by two Earth flybys and are promising candidates for the extended mission as they pass relatively near the saddle point without any corrective maneuvers. As the natural BC4BP arcs do not require adjustments to establish position, velocity, and time continuity, the corrections process is more straightforward than for the patched 3BP method. Two constraints are applied to enforce two distinct saddle point encounters, and two maneuvers are allowed: one maneuver on the unstable manifold arc prior to the first saddle point encounter, and another at apogee before the final encounter. These maneuvers are represented as magenta triangles in Figure 5.4. The location of the maneuvers is somewhat arbitrary; alternate nodes may be allowed to include impulsive maneuvers, or more maneuvers may be added to the transfer. The selection of maneuver locations biases the final result, thus some consideration is given to choose locations that yield the most cost-effective transfer designs. Experimentation reveals that the two maneuver configuration depicted in Figure 5.4 offers such a low-cost design.

An initial iteration of the corrections process yields a trajectory that is continuous and includes two saddle point encounters. As many variants of the double-pass geometry are obtained from the unstable quasi-halo manifold arcs, a number of converged solutions are available. Each solution is further constrained to reduce the total Δv,

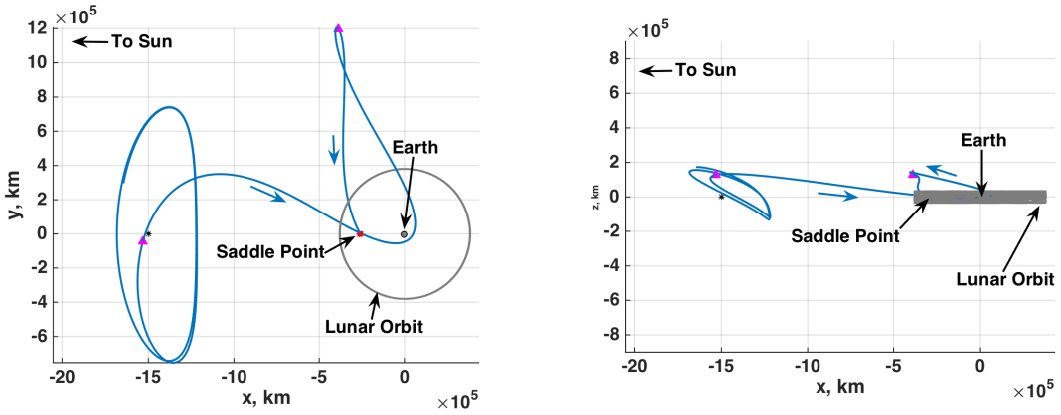

(a) xy-Projection

(b) xz-Projection

Figure 5.4.: An example of a corrected double-pass transfer that includes two maneuvers (magenta triangles) and two saddle point encounters

and an iterative process proceeds until the Δv can no longer be reduced. The most cost-effective solution from this process is pictured in Figure 5.4 and includes two maneuvers with a total Δv budget of 29 m/s. The initial maneuver, located near L_1, is relatively small with a magnitude of 1.4 m/s, and guarantees the first saddle point encounter, which occurs approximately 206 days after departing the LPF primary mission orbit. The second maneuver, located at apogee, has a magnitude of 26.6 m/s and shifts the descending portion of the trajectory to guarantee the second saddle point flyby, which occurs about 63 days after the first encounter. If this maneuver is not performed, the spacecraft path misses the saddle point location by roughly 5000 km, well outside the maximum pass distance of 100 km. Regardless of whether the second maneuver is performed, the trajectory departs the Earth vicinity in the direction of L_2 and does not return during a reasonable time scale (i.e., years).

Other solutions obtained from double-pass natural motion require similar maneuver budgets to achieve both saddle point encounters. As with the case illustrated in Figure 5.4, the first maneuver on the manifold arc typically has a magnitude less than 2 m/s while the second maneuver magnitude ranges from 26 m/s to 100+ m/s. As

all the solutions possess the double-pass geometry, all depart the system in the direction of L_2 following the second encounter. The spacecraft speed at the first saddle point encounter ranges from 1556 - 1560 m/s and the speed at the second encounter varies between 1595 and 1597 m/s. Thus, the double-pass trajectory designs satisfy all extended mission constraints *except* the total Δv budget. Although theses results are more efficient than the patched 3BP results by hundreds of meters per second, an additional order of magnitude decrease in total Δv is required.

5.2.2 Loose Capture Geometry

Though loosely captured arcs require longer times of flight to reach the saddle point, additional opportunities exist to adjust the spacecraft path to achieve the required encounters at a low cost. One such loosely captured path is depicted in Figure 5.5, with three impulsive maneuvers represented by magenta triangles. The correc-

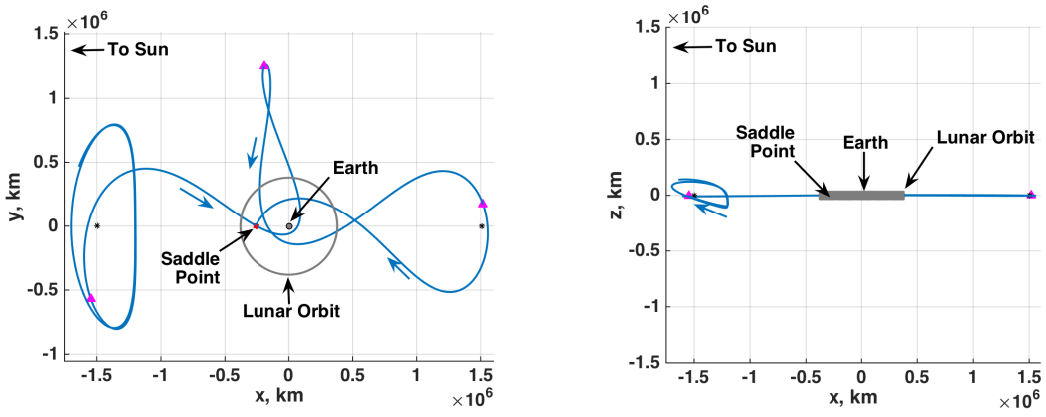

(a) xy-Projection (b) xz-Projection

Figure 5.5.: An example of a corrected loose-capture transfer that includes two maneuvers (magenta triangles) and two saddle point encounters

tions process for loosely captured trajectories mirrors the process followed to correct transfers with a double-pass geometry. As the trajectory is already continuous in the BC4BP, the maneuvers serve to adjust the spacecraft path to achieve the re-

quired saddle point encounters. Once a feasible design is converged upon, additional constraints are applied to reduce the total Δv and an iterative corrections process is employed until no further reductions are possible. The result of this process is the trajectory plotted in Figure 5.5. The first saddle point encounter occurs approximately 205 days after departing the LPF primary mission orbit, with a second encounter 190 days later. In this case, the corrections process converges on a design that exists almost entirely in the ecliptic plane, i.e., the xy-plane, as illustrated in Figure 5.5(b). The first maneuver on the trajectory accomplishes this plane change and targets the first saddle point encounter by applying a velocity change with a magnitude of 40.3 m/s. The second and third maneuvers target the final saddle point encounter, with magnitudes of 13.7 and 1.2 m/s, respectively. Subsequently, the total Δv budget for this trajectory option is 55.2 m/s, an amount comparable with many of the double-pass transfers. The spacecraft speed at each encounter is also similar to the double-pass geometries: 1567 m/s at the first encounter and 1608 m/s at the second encounter. Thus, the candidate trajectory for the extended mission once again fulfills all mission requirements apart from the total Δv requirement. Many other loosely captured trajectory geometries exist, but none have been identified that satisfy the mission constraints while requiring less than the allotted 4 m/s maneuvering budget.

5.2.3 Capture Geometry

A final transfer option incorporates natural motion in the BC4BP that leverages a lunar flyby to capture into the Earth-Moon vicinity. Due to the decrease in energy, the spacecraft path remains near the Earth and offers multiple saddle point encounters, as illustrated by the capture trajectory plotted in Figure 4.19(d). Additionally, the sensitive nature of the flyby facilitates trajectory adjustments to achieve the saddle point encounters. That is, small changes in the flyby position and velocity effect large changes in the downstream trajectory that may be leveraged to accomplish mission goals.

Despite their benefits, capture-type geometries have several drawbacks. Although the compact geometries offer many encounter options, many revolutions may be required to reach the saddle point with the consequence of long times-of-flight. Additionally, the low-altitude perigees common to these geometries may pass within the orbit of Earth-orbiting satellites or repeatedly pass through the Van Allen radiation belts. Finally, the sensitive lunar flybys facilitate large changes with minimal maneuver requirements, but such downstream effects can be difficult to predict and no additional propellant is available for further adjustments. Further investigation is warranted to leverage these lunar gravity assists and realize the extended mission goals.

5.3 Summary of BC4BP Results

Both the patched 3BP designs and natural BC4BP are corrected for continuity and to meet mission constraints in the Sun-Earth-Moon BC4BP. The relevant characteristics of the trajectory designs discussed above are listed in Table 5.1. Recall that the extended mission requirements stipulate that total ΔV is less than 4 m/s, the total time-of-flight (TOF) is less than 730 days, and the Earth-centered inertial speed at each saddle point encounter, SP_1 and SP_2, is between 1 and 2 km/s. As discussed previously, each trajectory design satisfies all but the Δv requirement. The double-pass design options deliver one saddle point encounter with the allotted propellant amount, but cannot deliver a second encounter without exceeding the budget. The loosely captured design requires slightly more propellant to complete the mission, and the patched three-body designs require even more.

5.4 Corrections in an Ephemeris Model

To demonstrate the validity of the BC4BP corrections process, each sample trajectory is transitioned from the BC4BP to an ephemeris model and recorrected. The *Ephemeris Corrections Module* within the Adaptive Trajectory Design (ATD) suite, a

Table 5.1.: BC4BP-Corrected Results

Design	Total Δv, m/s	TOF to SP_1, days	TOF to SP_2, days	$SP_1 \|\vec{v}\|$, m/s	$SP_2 \|\vec{v}\|$, m/s
1:2 Resonance	278.3	379.7	55.5	1533.9	1552.9
2:3 Resonance	538.1	393.5	41.1	1486.2	1518.9
Double Pass	28.0	205.6	62.6	1559.7	1596.3
Loose Capture	55.2	205.2	189.9	1566.8	1607.9

Purdue and NASA Goddard collaboration, is employed for this process [42, 36]. The gravitational forces due to the Sun, Earth, and Moon are included in the corrections process and other perturbing forces such as solar radition pressure are neglected. Although the same gravitational influences are included in the BC4BP, the ephemeris environment accounts for the noncircular motion of the primaries and the designs obtained from the BC4BP are discontinuous whem propagated in the ephemeris model. Accordingly, a multiple shooting corrections process is employed to resolve the discontinuities. Impulsive maneuvers are implemented in locations similar to those selected in the BC4BP corrections process, and constraints on two distinct saddle point encounters are applied. Finally, an iterative corrections process reduces the total Δv to achieve a more cost-effective transfer.

First, consider the designs from the patched 3BP method. These designs are corrected in the BC4BP, as described previously, and then transitioned to the ephemeris environment for further corrections. A comparison of the BC4BP trajectory (Figures 5.2 and 5.3) with the ephemeris paths, plotted in Figure 5.6, demonstrates that the geometry obtained in the BC4BP is approximately retained in the ephemeris environment. The maneuver budgets associated with each design decrease during this transition: the 1:2 resonant orbit design shifts from a total Δv of 278 m/s to 200 m/s, and the 2:3 resonant orbit design shifts from 538 m/s to 300 m/s. Other mission parameters, such as the time of flight to reach each saddle point encounter

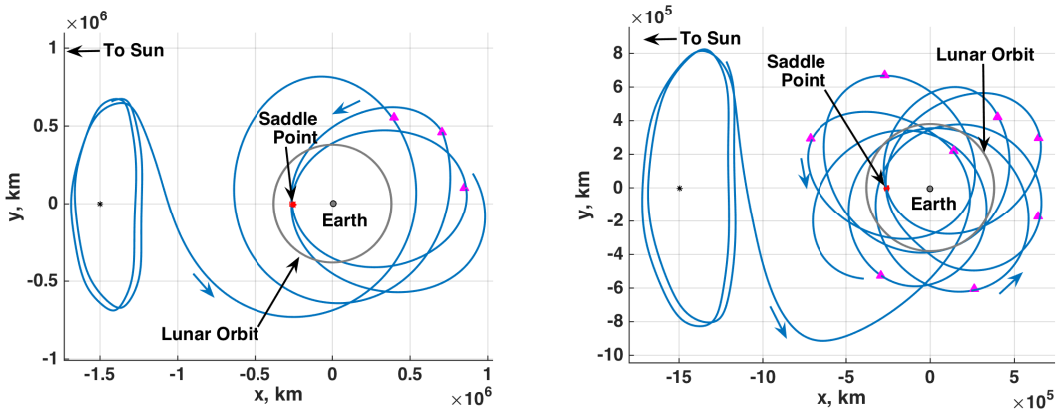

(a) 1:2 Resonant Orbit

(b) 2:3 Resonant Orbit

Figure 5.6.: Designs from the patched 3BP, corrected ATD's ephemeris environment under the influence of the Sun, Earth, and Moon gravity

and the spacecraft speed at the encounters, remain approximately the same. Thus, the ephemeris-corrected transfer design meets the same mission requirements as the BC4BP-corrected design and although the total cost for each transfer is decreased, it remains above the required maneuver budget.

The solutions obtained from natural motion in the BC4BP are also transitioned to the ephemeris environment. As with the designs derived from the patched 3BP, the BC4BP motion is approximately retained when transitioned to the higher-fidelity model. A comparison of the BC4BP-corrected results (Figures 5.4 and 5.5) with the ephemeris results, plotted in Figure 5.7, verifies that the geometry between the two sets of results remains similar. Note that the maneuvers for these designs are located in different locations to achieve more efficient transfers. In these cases, the maneuver budget required to achieve the desired saddle point encounters increases in the ephemeris environment, from 28 m/s to 87 m/s for the double-pass option, and from 55 m/s to 108 m/s for the loosely captured option. Similar to the patched 3BP designs, the times-of-flight to the saddle point encounters, and the spacecraft speed at these encounters, remain nearly identical for the natural BC4BP designs

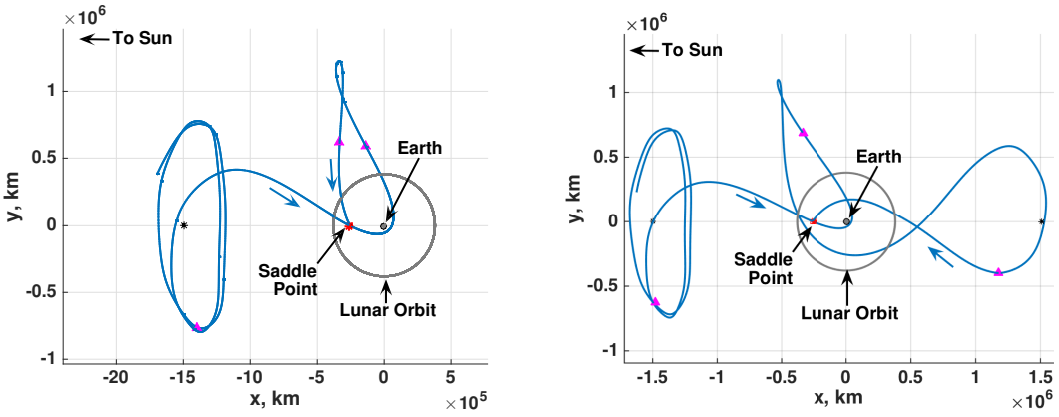

(a) Double-Pass

(b) Loose Capture

Figure 5.7.: Designs from the BC4BP, corrected ATD's ephemeris environment under the influence of the Sun, Earth, and Moon gravity

in the ephemeris model. A summary of the relevant trajectory parameters for each ephemeris-corrected design is listed in Table 5.2. As with the BC4BP-corrected results, these designs meet all but the total Δv constraint for the extended mission.

Table 5.2.: Ephemeris-Corrected Results

Design	Total Δv, m/s	TOF to SP_1, days	TOF to SP_2, days	SP_1 $\|\vec{v}\|$, m/s	SP_2 $\|\vec{v}\|$, m/s
1:2 Resonance	200.0	380.2	56.1	1524.3	1522.3
2:3 Resonance	300.0	393.1	41.5	1468.1	1527.9
Double Pass	87.0	205.5	62.5	1579.4	1619.9
Loose Capture	108.0	205.0	189.1	1575.2	1644.71

5.5 Summary of Results

Several transfer design strategies have been explored, each with their own advantages and disadvantages. The first method, which combines Earth-Moon resonant orbits with Sun-Earth halo orbit manifold arcs, leverages knowledge of three-body dynamics to rapidly construct an end-to-end transfer. Motion in each system is well understood and transfer segments can be selected from large families of periodic and quasi-periodic motion. However, the Earth-Moon resonant arcs that exist near the energy level of the Sun-Earth manifold arc are strongly perturbed by Solar gravity and require large maneuvers to recover the desired geometry. The second approach, which utilizes natural motion in the BC4BP and completes two Earth flybys, clearly leverages three gravitational bodies and is more difficult to predict than three-body motion. Periodic orbits are not available in the BC4BP, and an additional variable, epoch, influences the dynamics. However, because this motion exists naturally, fewer corrections are required. Additionally, the geometry of the transfers is simple (i.e., does not include many "loops" or close flybys) and is easily constrained to encounter the saddle point twice. Partially captured motion possesses many of the same characteristics as the double-pass motion, but introduces additional revolutions about the Earth and longer times of flight to complete the extended mission. A final concept, that leverages natural four-body motion and lunar gravity assists, yields trajectories that possess more complex geometry than the double pass transfers. Although the captured motion is natural and does not require corrections for continuity, the differential corrections process struggles to implement meaningful adjustments because of the sensitivity and complexity of the arcs. A more sophisticated strategy remains the focus of future work.

The trajectories generated by each strategy offer different strengths and weaknesses as well. Resonant orbits supply simple, planar motion that encounters the saddle point at regular intervals. Unfortunately, constructing the ideal geometry in the BC4BP requires prohibitively large maneuvers. The double-pass transfers are

simpler to correct and successfully encounter the saddle point multiple times, albeit while requiring larger maneuvers than are allowed for the extended mission. The fully captured transfer geometry does possess the potential to satisfy all mission requirements - the lunar flybys may be targeted to produce desirable geometries for a minimal maneuver cost - but the sensitive dynamics demand further development of the techniques. Additionally, although the slow precession of the captured arcs guarantees several saddle point encounters, the time-of-flight to reach the saddle point can exceed the desired 2 year extended mission duration.

Although no transfers have been identified that meet all mission constraints, numerous options remain that may uncover trajectories capable of satisfying the requirements. An extended stay in the Sun-Earth L_1 Lissajous orbit may allow the LPF spacecraft to approach the Earth-Moon vicinity on a variety of different manifold arcs and at a different epochs and, thus, reduce the maneuver costs required to pass within 100 km of the saddle point. A more sophisticated corrections scheme may also leverage lunar flybys to adjust capture arc geometries and reach the saddle point with a minimal propellant cost. Finally, the addition of solar radiation pressure to the ephemeris corrections process can supply additional forces to minimize the total ΔV during the extended mission.

6. SUMMARY AND FUTURE WORK

6.1 Summary

This investigation seeks to develop tools and techniques to construct trajectories that repeatedly encounter a dynamically defined point in space. The LISA Pathfinder extended mission concept to visit a gravitational equilibrium point, or saddle point, is explored to demonstrate these tools and techniques. To facilitate the design of such trajectories, two dynamical models are formulated: the Circular Restricted Three-Body Problem (CR3BP) and Bi-Circular Restricted Four-Body Problem (BC4BP). Dynamical systems techniques are discussed and implemented to leverage natural structures within the CR3BP and BC4BP for trajectory design. The behavior of the saddle point is analyzed and a model of the LISA Pathfinder primary mission orbit is developed. Low-cost transit arcs, i.e., unstable manifold arcs, are propagated from the approximate primary mission orbit and deliver the spacecraft to the vicinity of the Earth and saddle point. Periodic motion in the Earth-Moon system is explored to satisfy the extended mission requirements and supply multiple saddle point encounters. Higher-dimensional Poincaré mapping techniques are applied to identify links between the unstable manifold arcs and the Earth-Moon periodic orbits. These "patched" trajectory designs are corrected in the Sun-Earth-Moon BC4BP and in an ephemeris environment to demonstrate their persistence and validity. Natural motion flowing from the unstable manifold arcs within the Sun-Earth-Moon BC4BP is also investigated as a means to achieve multiple saddle point encounters; similar corrections processes are followed to validate these trajectory designs. The main conclusions of this study are as follows:

i. Transfers that depart the Sun-Earth L_1 vicinity and achieve multiple saddle point encounters are intuitively designed by combining natural structures in the

Sun-Earth CR3BP and Earth-Moon systems that achieve individual mission goals. Higher-dimensional Poincaré maps prove effective in locating low-cost links between inter-system arcs.

ii. Natural motion in the Sun-Earth-Moon BC4BP closely approximates motion in the Sun-Earth-Moon ephemeris model, yet the small differences in primary eccentricity and semi-major axis have significant impacts on the total maneuver budget for the trajectory designs.

iii. LPF extended mission trajectory designs that achieve multiple saddle point encounters while simultaneously requiring less than 4 m/s of maneuvering capability are not immediately apparent in patched 3BP motion or in natural BC4BP motion; trajectories that leverage the complex dynamics of the Sun-Earth-Moon system are required to meet this stringent design constraint.

Thus, a design strategy to construct trajectories to a dynamically defined point in space is demonstrated with applications to the LISA Pathfinder extended mission concept.

6.2 Future Work

Although the design strategy is successfully employed to design transfers with multiple saddle point encounters, additional exploration is required to identify designs that meet the stringent Δv constraint. Proposed areas of future work are as follows:

i. The analysis direction may be reversed. That is, mapping techniques may be applied near the saddle point to identify natural motion, and, potentially, structures of motion that repeatedly encounter the saddle point. Additional maps may be constructed to identify links between this nearby motion and arcs that approach the primary mission orbit in reverse time.

ii. Arcs that posses close lunar encounters may be leveraged to supply dense, low-energy motion in the Earth and saddle point vicinity and, thus, achieve multiple

saddle point encounters. More sophisticated shooting techniques will facilitate this effort.

iii. The total Δv associated with trajectory designs depends strongly on the baseline trajectory. Although the Δv for many designs is reduced via constraints in the corrections process, lower-cost results may be identified by employing optimization. For example, a genetic algorithm may identify the optimal locations for maneuver placement and sequential quadratic programming algorithms may locate locally optimal results for a fixed maneuver itinerary.

The implementation of these goals requires the development of new tools and trajectory design techniques.

LIST OF REFERENCES

LIST OF REFERENCES

[1] P. McNamara, S. Vitale, and K. Danzmann. Lisa pathfinder. *Classical and Quantum Gravity*, 25(11), May 2008.

[2] P. McNamara and G. Racca. Introduction to lisa pathfinder. Technical Report LISA-LPF-RP-0002, European Space Agency, November 2009.

[3] E. Fabacher, S. Kemble, C. Trenkel, and N. Dunbar. Multiple sun-earth saddle point flybys for lisa pathfinder. *Advances in Space Research*, 52(1):105–116, 2013.

[4] J. Bekenstein and J. Magueijo. Modified newtonian dynamics habitats within the solar system. *Phys Rev D*, 2006.

[5] M. Milgrom. A modification of the newtonian dynamics as a possible alternative to the hidden mass hypothesis. *Astrophysical Journal*, 270:365–370, July 1983.

[6] F. Zwicky. On the masses of nebulae and clusters of nebulae. *Astrophysical Journal*, 86:217, 1937.

[7] S. Kemble. Personal Communication, Jan 2015.

[8] C. Trenkel and S. Kemble. Gravitational science with lisa pathfinder. In *Journal of Physics: Conference Series 154*. IOP Publishing, 2009.

[9] C. Trenkel, S. Kemble, N. Bevis, and J. Magueijo. Testing modified newtonian dynamics with lisa pathfinder. *Advances in Space Research*, 50(11):1570–1580, December 2012.

[10] A. E. Roy. *Orbital Motion*. Adam Hilger Ltd, 2 edition, 1982.

[11] Victor Szebehely. *Theory of Orbits: The Restricted Problem of Three Bodies*. Academic Press, 1967.

[12] W. S. Koon, M. W. Lo., J. E. Marsden, and S. D. Ross. *Dynamical Systems, the Three-Body Problem and Space Mission Design*. Marsden Books, 2011.

[13] A. E. Roy and M. W. Ovenden. On the occurence of commensurable mean motions in the solar system. the mirror theorem. *Monthly Notices of the Royal Astronomical Society*, 115:296, December 1954.

[14] A. Haapala. Trajectory design using periapse maps and invariant manifolds. M.S. thesis, Purdue University, December 2010.

[15] A. M. Ozorio de Almeida. *Hamiltonian Systems: Chaos and Quantization*. Cambridge University Press, Cambridge, England, 1988.

[16] J. E. Guckenheimer, L. Sirovich, and F. John. *Nonlinear Oscillations, Dynamical Systems, and Bifurcations of Vector Fields*. Springer, New York, 1983.

[17] M. Hénon. Numerical exploration of the restricted three-body problem. In G.I. Kontopoulos, editor, *The Theory of Orbits in the Solar System and in Stellar Systems*, volume 25, pages 157–169. IAU Symposium, 1966.

[18] V. A. Yakubovich and V. M. Starzhinskii. *Linear Differential Equations with Periodic Coefficients*, volume 1. John Wiley and Sons, New York, 1975.

[19] B. A. Steves, A. J. Maciejewski, and M. Hendry. *Chaotic Worlds: From Order to Disorder in Gravitational N-Body Dynamical Systems*, volume 227 of *Mathematics, Physics and Chemistry*. Springer, Dordrecht, Netherlands, 2006.

[20] L. Perko. *Differential Equations and Dynamical Systems*. Springer, New York, 2001.

[21] T. S. Parker and L. O. Chua. *Practical Numerical AAlgorithm for Chaotic Systems*. Springer-Verlag, Berlin, 1989.

[22] H. Keller. *Numerical Solution of Two Point Boundary Value Problems*. Society for Industrial and Applied Mathematics, Philadelphia, 1976.

[23] K. E. Atkinson. *An Introduction to Numerical Analysis*. John Wiley and Sons, New York, second edition edition, 1989.

[24] G. Gómez, J. J. Masdemont, and C. Simó. Quasihalo orbits associated with libration points. *Journal of the Astronautical Sciences*, 46(2):135–176, 1998.

[25] T. Pavlak. *Trajectory Design and Orbit Maintenance Strategies in Multi-Body Dynamical Regimes*. Ph.D. dissertation, Purdue University, May 2013.

[26] M. Vaquero. *Spacecraft Transfer Trajectory Design Exploiting Resonant Orbits in Multi-Body Environments*. Ph.D. dissertation, Purdue University, August 2013.

[27] E. Doedel and V. Romanov. Elemental periodic orbits associated with the libration points in the circular restricted 3-body problem. *International Journal of Bifurcation and Chaos*, 17(8), 2007.

[28] H. Keller. Numerical solutions of bifurcations and nonlinear eigenvalue problems. In P. Rabinowitz, editor, *Applications of Bifurcation Theory*, pages 359–384. Academic Press, 1977.

[29] Z. Olikara and D. Scheeres. Numerical method for computing quasi-periodic orbits and their stability in the restricted three-body problem. In *IAA Conference on Dynamics and Control of Space Systems*, 2012.

[30] G. Gómez and J. M. Mondelo. The dynamics around the collinear equilibrium points of the rtbp. *Physica D*, 157(4):283–321, 2001.

[31] C. Geisel. *Spacecraft Orbit Design in the Circular Restricted Three-Body Problem Using Higher Dimensional Poincaré Maps*. Ph.D. dissertation, Purdue University, December 2013.

[32] A. Haapala. *Trajectory Design in the Spatial Circular Restricted Three-Body Problem Exploiting Higher-Dimensional Poincare Maps*. Ph.D. dissertation, Purdue University, December 2014.

[33] M. Kakoi. Transfers between the earth-moon and sun-earth systems using manifolds and transit orbits. M.S. thesis, Purdue University, December 2005.

[34] W. Schlei. An application of visual analytics to spacecraft trajectory design. M.S. thesis, Purdue University, December 2011.

[35] D. Davis. *Multi-Body Trajectory Design Strategies Based on Periapsis Poincaré Maps*. Ph.D. dissertation, Purdue University, August 2011.

[36] A. D. Cox, N. Bosanac, D. Guzzetti, K. C. Howell, D. C. Folta, and C. M. Webster. An interactive trajectory design environment leveraging dynamical structures in multi-body regimes. In *6th International Conference on Astrodynamics Tools and Techniques*, Darmstadt, Germany, March 2016.

[37] N. Bevis, J. Magueijo., C. Trenkel, and S. Kemble. Mondian three-body predictions for lisa pathfinder. *Classical and Quantum Gravity*, 27(21), October 2010.

[38] C. H. Acton. Ancillary data services of nasa's navigation and ancillary information facility. *Planetary and Space Science*, 44(1):65–70, 1996.

[39] D. J. Grebow. Generating periodic orbits in the circular restricted three-body problem with applications to lunar south pole coverage. M.S. thesis, Purdue University, May 2006.

[40] K. C. Howell and M. Kakoi. Transfers between the earth-moon and sun-earth systems usin manifolds and transit orbits. *Acta Astronautica*, 59:367–380, 2006.

[41] E. Canalias and J. Masdemont. Computing natural transfers between sun-earth and earth-moon lissajous libration point orbits. *Acta Astronautica*, 63:238–248, 2008.

[42] A. Haapala, M. Vaquero, T. Pavlak, K. Howell, and D. Folta. Trajectory selection strategy for tours in the earth-moon system. In *AAS/AIAA Astrodynamics Specialist Conference*, Hilton Head, South Carolina, August 2013.

APPENDICES

A. MULTIPLE SHOOTING CONSTRAINT DERIVATIONS

The update equation leveraged to solve multiple shooting problems in this investigation requires information about the relationships between the set of design variables and constraint functions. To supplement the relationships derived in Section 3.2.4, relationships between a ΔV constraint and typical design variables are derived here.

A.1 Constraint on Total Δv

It is often useful to limit the total Δv on a trajectory to be a specific value. The constraint function takes the form

$$F = \Delta v_2 + \Delta v_3 + \cdots + \Delta v_i - \Delta v_{des} = 0, \tag{A.1}$$

where Δv_{des} is the desired total maneuver budget and Δv_i is the magnitude of the velocity discontinuity at node i, expressed by

$$\Delta v_i = \left\| \vec{v}_{i-1,f} - \vec{v}_i \right\| = \sqrt{(\dot{x}_{i-1,f} - \dot{x}_i)^2 + (\dot{y}_{i-1,f} - \dot{y}_i)^2 + (\dot{z}_{i-1,f} - \dot{z}_i)^2}\,. \tag{A.2}$$

Note that $\vec{v}_{i-1,f}$ is the velocity of the *integrated* segment that ends near node i and $\vec{v}_i$ is the velocity *at* node i. To apply this constraint in the multiple shooting algorithm, the derivatives of F with respect to the design variables are derived. To illustrate these derivations, consider a simple case with only one maneuver. The constraint function then takes the form

$$F = \sqrt{(\dot{x}_{i-1,f} - \dot{x}_i)^2 + (\dot{y}_{i-1,f} - \dot{y}_i)^2 + (\dot{z}_{i-1,f} - \dot{z}_i)^2} - \Delta v_{des} = f(\vec{v}_{i-1,f},\, \vec{v}_i). \tag{A.3}$$

The partial derivative with respect to node state $\vec{q}_i$ is split into derivatives with respect to the position and velocity states:

$$\frac{\partial F}{\partial \vec{r}_i} = \vec{0}_{3\times 1}, \tag{A.4}$$

$$\frac{\partial F}{\partial \vec{v}_i} = \frac{-2(\vec{v}_{i-1,f} - \vec{v}_i)(1/2)}{\Delta v_i} = \frac{1}{\Delta v_i}(\vec{v}_i - \vec{v}_{i-1,f}). \tag{A.5}$$

Next, consider the partial derivative with respect to node $i-1$. As with node i, partial derivatives taken with respect to the position states evaluate to zero. The velocity at node $i-1$, on the other hand, does effect the value of the constraint. Because $\vec{v}_{i-1}$ does not appear explicitly in the constraint equation, apply chain rule to compute the derivative,

$$\frac{\partial F}{\partial \vec{v}_{i-1}} = \frac{\partial f}{\partial \vec{v}_{i-1,f}} \frac{\mathrm{d}\vec{v}_{i-1,f}}{\mathrm{d}\vec{v}_{i-1}} + \frac{\partial f}{\partial \vec{v}_i} \frac{\mathrm{d}\vec{v}_i}{\mathrm{d}\vec{v}_{i-1}}\,. \tag{A.6}$$

The second ordinary derivative evaluates to zero as there is no dependency between nodes i and $i-1$. This leaves the first term: The ordinary derivative yields the STM evaluated at the end of the integrated segment, and the partial derivative term is similar to the partial $\frac{\partial F}{\partial \vec{v}_i}$:

$$\frac{\partial F}{\partial \vec{v}_{i-1}} = \frac{1}{\Delta v_i}(\vec{v}_{i-1,f} - \vec{v}_i)\mathbf{\Phi_{vv}}(\tau_i, 0). \tag{A.7}$$

The partial derivatives of F with respect to nodes other than i and $i-1$ are zero.

In addition to dependencies on the velocities at nodes i and $i-1$, the value of the constraint function is dependent on the time-of-flight τ and epoch time T associated with one or both of the nodes. Accordingly, the partial derivatives of the constraint with respect to τ and T are also computed. Neither time variable appears explicitly

in F, so the chain rule is applied once again. Consider first the relationship between F and time-of-flight,

$$\begin{aligned}\frac{\partial F}{\partial \tau_{i-1}} &= \frac{\partial f}{\partial \vec{v}_{i-1,f}} \frac{\mathrm{d}\vec{v}_{i-1,f}}{\mathrm{d}\tau_{i-1}} + \frac{\partial f}{\partial \vec{v}_i} \frac{\mathrm{d}\vec{v}_i}{\mathrm{d}\tau_{i-1}} \\ &= \frac{\partial f}{\partial \vec{v}_{i-1,f}} \dot{\vec{v}}_{i-1,f} + \frac{\partial f}{\partial \vec{v}_i} \vec{0} \\ &= \frac{1}{\Delta v_i}(\vec{v}_{i-1,f} - \vec{v}_i)\vec{a}_{i-1,f}, \end{aligned} \tag{A.8}$$

$$\tag{A.9}$$

where $\vec{a}_{i-1,f}$ is the acceleration at the end of the propagation originating at node $i-1$. This acceleration is easily obtained by evaluating the equations of motion at the state associated with the end of this propagation. Next, consider the relationship between F and epoch time,

$$\begin{aligned}\frac{\partial F}{\partial T_{i-1}} &= \frac{\partial f}{\partial \vec{v}_{i-1,f}} \frac{\mathrm{d}\vec{v}_{i-1,f}}{\mathrm{d}T_{i-1}} + \frac{\partial f}{\partial \vec{v}_i} \frac{\mathrm{d}\vec{v}_i}{\mathrm{d}T_{i-1}} \\ &= \frac{1}{\Delta v_i}(\vec{v}_{i-1,f} - \vec{v}_i) \frac{\mathrm{d}\vec{v}_{i-1,f}}{\mathrm{d}T_{i-1}} + \frac{\partial f}{\partial \vec{v}_i} \vec{0} \\ &= \frac{1}{\Delta v_i}(\vec{v}_{i-1,f} - \vec{v}_i) \frac{\mathrm{d}\vec{v}_{i-1,f}}{\mathrm{d}T_{i-1}}, \end{aligned} \tag{A.10}$$

where $\frac{\partial \vec{v}_{i-1,f}}{\partial T_{i-1}}$ is described by the velocity components of $\frac{\partial \vec{q}}{\partial T}$ given by the differential equation (3.65) and evaluated at the end of the segment propagated from node $i-1$. Recall that these quantities are numerically propagated simultaneously with the equations of motion. Derivatives with respect to any other time variables (including τ_i and T_i) are zero as these variables do not affect the constraint function.

The example developed above assumes only one maneuver is included in a multiple shooting corrections process. If more maneuvers are included, additional considerations become relevant. For example, if two subsequent nodes, i and $i+1$, include maneuvers, the constraint function takes the form

$$F = \Delta v_i + \Delta v_{i+1} = \left\|\vec{v}_{i-1,f} - \vec{v}_i\right\| + \left\|\vec{v}_{i,f} - \vec{v}_{i+1}\right\| = \Delta v_{des}. \tag{A.11}$$

In this case, the relationship between F and $\vec{v}_i$ includes two terms:

$$\begin{aligned}\frac{\partial F}{\partial \vec{v}_i} &= \frac{\partial \Delta v_i}{\partial \vec{v}_i} + \frac{\partial \Delta v_{i+1}}{\partial \vec{v}_i} \\ &= \frac{1}{\Delta v_i}(\vec{v}_i - \vec{v}_{i-1,f}) + \frac{1}{\Delta v_{i+1}}(\vec{v}_{i,f} - \vec{v}_{i+1})\mathbf{\Phi_{vv}}(\tau_{i+1}, 0). \end{aligned} \tag{A.12}$$

In contrast, the relationships between F and τ_{i-1}, T_{i-1}, τ_i and T_i all include one term each and are formulated in the same manner as derived above. These constraint functions and partial derivatives are applied in multiple shooting processes to constrain the total maneuver budget on a design with an arbitrary number of maneuvers. Although this constraint is formulated here as an equality constraint, the desired Δv may be replaced with a maximum value, Δv_{max}, and a slack variable can be introduced to construct an inequality constraint that possesses the same relationships with the state variables.

B. PARTIAL DERIVATIVES

Partial derivatives are leveraged in many applications in this investigation, most notably in linearized dynamical expressions that supply estimates to the full nonlinear dynamics. A selection of commonly applied derivatives are included in this section.

B.1 CR3BP Pseudo-Potential

The following equations represent the second partial derivatives of the CR3BP pseudo-potential function with respect to the position states x, y, and z, and are listed here for reference.

$$\Omega_{xx} = 1 - \frac{(1-\mu)}{d^3} - \frac{\mu}{r^3} + \frac{3(1-\mu)(x+\mu)^2}{d^5} + \frac{3\mu(x+\mu-1)^2}{r^5} \tag{B.1}$$

$$\Omega_{yy} = 1 - \frac{(1-\mu)}{d^3} - \frac{\mu}{r^3} + \frac{3(1-\mu)y^2}{d^5} + \frac{3\mu y^2}{r^5} \tag{B.2}$$

$$\Omega_{zz} = -\frac{(1-\mu)}{d^3} - \frac{\mu}{r^3} + \frac{3(1-\mu)z^2}{d^5} + \frac{3\mu z^2}{r^5} \tag{B.3}$$

$$\Omega_{xy} = \Omega_{yx} = \frac{3(1-\mu)(x+\mu)y}{d^5} + \frac{3\mu(x+\mu-1)y}{r^5} \tag{B.4}$$

$$\Omega_{xz} = \Omega_{zx} = \frac{3(1-\mu)(x+\mu)z}{d^5} + \frac{3\mu(x+\mu-1)z}{r^5} \tag{B.5}$$

$$\Omega_{yz} = \Omega_{zy} = \frac{3(1-\mu)yz}{d^5} + \frac{3\mu yz}{r^5} \tag{B.6}$$

These relationships are leveraged in multiple shooting applications.

B.2 BC4BP Pseudo-Potential

Consistent with the CR3BP, the BC4BP pseudo-potential function, Υ, possesses second partial derivatives that are useful in corrections processes and other applications. Those derivatives are listed here.

$$\Upsilon_{xx} = k^2 - (\frac{1}{k} - \mu)\left[\frac{1}{s^3} - \frac{3(x-x_1)^2}{s^5}\right] - (\mu - \nu)\left[\frac{1}{e^3} - \frac{3(x-x_2)^2}{e^5}\right] - \nu\left[\frac{1}{m^3} - \frac{3(x-x_3)^2}{m^5}\right] \tag{B.7}$$

$$\Upsilon_{yy} = k^2 - (\frac{1}{k} - \mu)\left[\frac{1}{s^3} - \frac{3y^2}{s^5}\right] - (\mu - \nu)\left[\frac{1}{e^3} - \frac{3(y-y_2)^2}{e^5}\right] - \nu\left[\frac{1}{m^3} - \frac{3(y-y_3)^2}{m^5}\right] \tag{B.8}$$

$$\Upsilon_{zz} = -(\frac{1}{k} - \mu)\left[\frac{1}{s^3} - \frac{3z^2}{s^5}\right] - (\mu - \nu)\left[\frac{1}{e^3} - \frac{3(z-z_2)^2}{e^5}\right] - \nu\left[\frac{1}{m^3} - \frac{3(z-z_3)^2}{m^5}\right] \tag{B.9}$$

$$\Upsilon_{xy} = \Upsilon_{yx} = (\frac{1}{k} - \mu)\frac{3(x-x_1)y}{s^5} + (\mu - \nu)\frac{3(x-x_2)(y-y_2)}{e^5} + \nu\frac{3(x-x_3)(y-y_3)}{m^5} \tag{B.10}$$

$$\Upsilon_{xz} = \Upsilon_{zx} = (\frac{1}{k} - \mu)\frac{3(x-x_1)z}{s^5} + (\mu - \nu)\frac{3(x-x_2)(z-z_2)}{e^5} + \nu\frac{3(x-x_3)(z-z_3)}{m^5} \tag{B.11}$$

$$\Upsilon_{yz} = \Upsilon_{zy} = (\frac{1}{k} - \mu)\frac{3yz}{s^5} + (\mu - \nu)\frac{3(z-z_2)(y-y_2)}{e^5} + \nu\frac{3(z-z_3)(y-y_3)}{m^5} \tag{B.12}$$

It is interesting to note that although the EOMs formulated for the BC4BP in this investigation include an origin at the B_2 barycenter, the resulting centripetal acceleration term in the EOMs (and in Υ) does not appear in these second derivatives. Because the distance between B_2 and the system barycenter, B_1, is fixed, the centripetal acceleration has a constant magnitude does not appear in higher-order derivatives.

B.3 BC4BP Dependencies on Primary Position

The effects of the locations of the primaries on the acceleration of P_4 in the BC4BP are captured by the second-order partial derivatives listed in this section. These derivatives have a similar form to the BC4BP pseudo-potential second derivatives. First, consider the affect of the motion of P_1 on the acceleration of P_4. This case is

particularly simple since P_1 is fixed in the rotating frame, i.e., $y_1 = z_1 = 0$ and x_1 is constant. Accordingly, the only non-zero partial derivatives are

$$\frac{\partial \ddot{x}}{\partial x_1} = -(\frac{1}{k} - \mu)\left[\frac{-1}{r_{1,4}^3} + \frac{3(x - x_1)^2}{r_{1,4}^5}\right] \tag{B.13}$$

$$\frac{\partial \ddot{y}}{\partial x_1} = -(\frac{1}{k} - \mu)\frac{3(x - x_1)y}{r_{1,4}^5} \tag{B.14}$$

$$\frac{\partial \ddot{y}}{\partial x_1} = -(\frac{1}{k} - \mu)\frac{3(x - x_1)z}{r_{1,4}^5} \tag{B.15}$$

The partial derivatives with respect to the positions of P_2 and P_3, i.e., $\vec{r}_2$ and $\vec{r}_3$, respectively, follow a similar pattern, but with fewer zero elements:

$$\frac{\partial \ddot{x}}{\partial x_2} = -(\mu - \nu)\left[\frac{-1}{r_{2,4}^3} + \frac{3(x - x_2)^2}{r_{2,4}^5}\right] \tag{B.16}$$

$$\frac{\partial \ddot{y}}{\partial y_2} = -(\mu - \nu)\left[\frac{-1}{r_{2,4}^3} + \frac{3(y - y_2)^2}{r_{2,4}^5}\right] \tag{B.17}$$

$$\frac{\partial \ddot{z}}{\partial z_2} = -(\mu - \nu)\left[\frac{-1}{r_{2,4}^3} + \frac{3(z - z_2)^2}{r_{2,4}^5}\right] \tag{B.18}$$

$$\frac{\partial \ddot{x}}{\partial y_2} = \frac{\partial \ddot{y}}{\partial x_2} = -(\mu - \nu)\frac{3(x - x_2)(y - y_2)}{r_{2,4}^5} \tag{B.19}$$

$$\frac{\partial \ddot{x}}{\partial z_2} = \frac{\partial \ddot{z}}{\partial x_2} = -(\mu - \nu)\frac{3(x - x_2)(z - z_2)}{r_{2,4}^5} \tag{B.20}$$

$$\frac{\partial \ddot{y}}{\partial z_2} = \frac{\partial \ddot{z}}{\partial y_2} = -(\mu - \nu)\frac{3(y - y_2)(z - z_2)}{r_{2,4}^5} \tag{B.21}$$

$$\frac{\partial \ddot{x}}{\partial x_3} = -\nu \left[\frac{-1}{r_{3,4}^3} + \frac{3(x - x_3)^2}{r_{3,4}^5} \right] \tag{B.22}$$

$$\frac{\partial \ddot{y}}{\partial y_3} = -\nu \left[\frac{-1}{r_{3,4}^3} + \frac{3(y - y_3)^2}{r_{3,4}^5} \right] \tag{B.23}$$

$$\frac{\partial \ddot{z}}{\partial z_3} = -\nu \left[\frac{-1}{r_{3,4}^3} + \frac{3(z - z_3)^2}{r_{3,4}^5} \right] \tag{B.24}$$

$$\frac{\partial \ddot{x}}{\partial y_3} = \frac{\partial \ddot{y}}{\partial x_3} = -\nu \frac{3(x - x_3)(y - y_3)}{r_{3,4}^5} \tag{B.25}$$

$$\frac{\partial \ddot{x}}{\partial z_3} = \frac{\partial \ddot{z}}{\partial x_3} = -\nu \frac{3(x - x_3)(z - z_3)}{r_{3,4}^5} \tag{B.26}$$

$$\frac{\partial \ddot{y}}{\partial z_3} = \frac{\partial \ddot{z}}{\partial y_3} = -\nu \frac{3(y - y_3)(z - z_3)}{r_{3,4}^5} \tag{B.27}$$

These derivatives are included in the Jacobian matrix entries associated with many constraints in BC4BP multiple shooting processes